University of Groningen

Ge-Sb-Te based phase-change nanoparticles

Chen, Bin

IMPORTANT NOTE: You are advised to consult the publisher's version (publisher's PDF) if you wish to cite from it. Please check the document version below.

Document Version
Publisher's PDF, also known as Version of record

Publication date:
2017

Link to publication in University of Groningen/UMCG research database

Citation for published version (APA):
Chen, B. (2017). *Ge-Sb-Te based phase-change nanoparticles: Synthesis, structure characterization and crystallization kinetics*. [Thesis fully internal (DIV), University of Groningen]. University of Groningen.

Copyright
Other than for strictly personal use, it is not permitted to download or to forward/distribute the text or part of it without the consent of the author(s) and/or copyright holder(s), unless the work is under an open content license (like Creative Commons).

The publication may also be distributed here under the terms of Article 25fa of the Dutch Copyright Act, indicated by the “Taverne” license. More information can be found on the University of Groningen website: https://www.rug.nl/library/open-access/self-archiving-pure/taverne-amendment.

Take-down policy
If you believe that this document breaches copyright please contact us providing details, and we will remove access to the work immediately and investigate your claim.

Downloaded from the University of Groningen/UMCG research database (Pure): http://www.rug.nl/research/portal. For technical reasons the number of authors shown on this cover page is limited to 10 maximum.

Download date: 04-05-2023

Ge-Sb-Te based phase-change nanoparticles

Synthesis, structure characterization
and crystallization kinetics

Bin Chen

PhD thesis
University of Groningen
The Netherlands

The work presented in this thesis was performed in the Nanostructured Materials and Interfaces group at the Zernike Institute for Advanced Materials of the University of Groningen, The Netherlands. This research was funded by the China Scholarship Council.

Zernike Institute for Advanced Materials PhD thesis series 2017-24
ISSN:1570-1530
ISBN: 978-94-034-0198-0 (electronic version)
ISBN: 978-94-034-0199-7 (printed version)

Cover designed by Bin Chen
Printed by Gildeprint

university of groningen

faculty of science and engineering

zernike institute for advanced materials

Ge-Sb-Te based phase-change nanoparticles

Synthesis, structure characterization and crystallization kinetics

PhD thesis

to obtain the degree of PhD at the
University of Groningen
on the authority of the
Rector Magnificus Prof. E. Sterken
and in accordance with
the decision by the College of Deans.

This thesis will be defended in public on

Friday 17 November 2017 at 11.00 hours

by

Bin Chen

born on 16 April 1987
in Sichuan, China

Supervisors
Prof. B. J. Kooi
Prof. G. Palasantzas

Assessment committee
Prof. H. Bhaskaran
Prof. K. U. Loos
Prof. M. A. Loi

To my family

Contents

Chapter 1

General introduction

1.1 History of phase-change materials

The first observation of phase-change characteristics dates back to the 1920s, when Waterman observed a large negative coefficient of resistivity as a function of temperature in MoS_2.[1] Further exploration led him to the discovery of the breakdown of the resistivity coefficient when MoS_2 is heated above a critical voltage by an electrical current, where a permanent increase in electrical conductivity was obtained by applying a voltage higher than the threshold values. It was pointed out that two different phases existed in the material with respect to temperature. However, this discovery attracted little attention due to the lack of a practical application. After the invention and development of the computer drive, the search for a non-volatile random access memory to replace the non-volatile magnetic core memory in the 1950s resulted in more intense studies of chalcogenide based materials. In 1962, the reversible switching between stable high and low conductivity states was observed by applying a proper electrical pulse to As-Te-I glass by Pearson et al., but no explanation of the switching mechanism nor applications was mentioned.[2] The threshold switching that is important in phase-change memory application was detected by Ovshinsky in chalcogenide glasses in 1968.[3] $Ge_{10}Si_{12}As_{30}Te_{48}$ alloy showed the reversible switching over period of several months, yielding it as a potential memory. This breakthrough triggered the practical interest of using chalcogenides in memory technology. Many patents came out disclosing the operations and appropriate compositions in 1960s, with the first phase-change memory device built by Shanefield.[4] In the early 1970s, a 256-bit array consisting of phase-change memory was built by Neale and Nelson.[5] However, due to the enormous power consumption needed to program the phase-change memory in comparison to the conventional metal oxide semiconductor memory, phase-change memory went into hibernation for 2 decades without commercial interest.[6]

The other interest in phase-change materials (PCMs) relates to optical recording media due to the high difference in optical reflectivity between the two phases. After the first demonstration of laser-induced reversible phase-change by Feinleib in 1971, Yamada found superior properties in pseudo-binary alloy, $GeTe\text{-}Sb_2Te_3$, which could be crystalized within 50 nanoseconds in 1987.[7] This extremely fast crystallization triggered commercial interest rapidly. In 1990 Panasonic introduced the first product: R/W phase-change optical disc drive (500 MB).[8] After the development of GeSbTe alloy, Ag and In doped SbTe and Ge doped Sb alloys were also developed as storage medium in optical discs.

The application in optical storage facilitated the rebirth of PCMs as the active element in non-volatile random access memory. In early 2000s, the emerging photolithography technology enabled the scaling of components as small as 180 nm. The large decrement in dimensions could efficiently lower the power needed for programming, making phase-change memory again promising. After the formation of Ovonyx by Lowrey and Parkinson in 1999, BAE Systems granted the phase-change memory technology for space applications. In 2006 BAE introduced the first commercial phase-change memory that is 3.3 V, 4 Mb memory device. Ovonyx reached an agreement with Intel in 2000, after which Intel and Ovonyx re-introduced the phase-change memory to the industry in 2001. Hence, the interest from industry and academy grew dramatically, leading to the exponential increase of the US patents and publications on PCMs. Many prototypes of phase-change memory were then developed by various companies, such as 46.7 nm cell (512 Mb) by Samsung in 2004, 90 nm device (256 Mb) by Intel in 2008 and the recent 3D Xpoint based on chalcogenides that is claimed 1000 times faster than NAND and 10 times denser than DRAM.[9] In 2017 Intel released their first SSD (solid state drive) based on 3D Xpoint memory (375 GB).

Nowadays the most widely used and studied PCMs can be categorized in three groups: alloys lying on (or very close to) the GeTe-Sb2Te3 tie line, such as GeTe, $Ge_1Sb_2Te_4$ and $Ge_2Sb_2Te_5$; Ag, In and Ge doped Sb_2Te, such as $Ag_5In_5Sb_{60}Te_{30}$ and the more recently discovered Ge doped Sb.[8]

1.2 Properties

Standard PCMs contain two types of structures, i.e., amorphous and crystalline phases. Due to the absence of long-range order in the amorphous phase, it is complicated to obtain the structural properties. Two crystalline phases exist in the GeSbTe alloy when the PCMs are annealed above their crystallization temperature. At low temperature it is present in the rock-salt structure (space group $Fm\bar{3}m$) that consists of two face-centered cubic sublattices shifted by half the lattice parameter in each direction (1/2,1/2,1/2), where one sublattice is occupied by tellurium atoms the other is statistically occupied by germanium, antimony and vacancies. When the alloy is annealed at high temperature (350-400 ^{o}C), the rock-salt structure then changes to an ordered stacking structure with a rhombohedral structure (in general space group $R\bar{3}m$). The amorphous phase can be obtained again by melting the materials (usually around 600-650 ^{o}C) and quenching them with extremely high cooling rate (>10^9 K/s). Another switching mechanism, bipolar switching, has been proposed in a special case, where the drift of the Ge and Sb atoms induced by the polar electric field leads to the resistance switching of the mushroom-like GST dome.[10–13]

In order to be used in optical storage or phase-change memory, the materials have to meet several requirements: large optical/electrical contrasts between the amorphous and crystalline states; high speed crystallization for fast memory switching; low threshold voltage switching the materials for PCRAM (phase-change random access memory); long thermal stability of amorphous phase (at least up to 80 °C) and excellent endurance (high cyclability).[14]

The electrical conductivity of the crystalline phase is up to 5 orders of magnitude higher than the one of the amorphous phase.[15] The dielectric function also varies significantly upon crystallization, from 5.0+i1.3 to 6.5+i3.5 for $Ge_2Sb_2Ge_5$ for a wave length of 830 nm, providing up to 30% difference in reflectivity.[16] The optical and electrical contrasts between these two phases enable the PCMs to encode information.

The amorphous state of the PCM can be obtained by a short and large electrical or laser pulse (RESET) which can melt the PCM and where the subsequently high quenching rate makes the PCM amorphous. The amorphous phase can be crystallized (SET) by a longer and lower pulse that enables the heating of the PCM above its crystallization temperature. Typical PCMs crystallize in a time scale of 1-100 ns,[17] while amorphization takes place much faster than crystallization. The crystallization speed of 500 picoseconds has been achieved for $Ge_2Sb_2Te_5$ cells by pre-ordering the structure with a low voltage pulse before the SET pulse.[18] For PCRAM technology, the threshold switching is of key importance without which the PCRAM would not be feasible. Above the threshold voltage the amorphous phase (high resistivity state) starts to become conductive and only then starts to dissipate sufficient heat to allow crystallizing by which the resistivity drops. By applying a higher voltage the RESET process to the amorphous can be achieved. A doped-SbTe phase-change cell (with the dimension of $200\times20\times20$ nm^3) switched from high to low resistivity states at 1.0 V with 30 ns pulses while the RESET could be performed by 1.4 V voltage with 30 ns pulses.[19] Similar transitions can also be observed for GeTe and GeSbTe phase-change cells. For example, a threshold voltage of 0.65 V was obtained for a 60 nm thick $Ge_2Sb_2Te_5$ film.[20] The PCMs present excellent endurance for switching. A PCRAM cell using nitrogen-doped GeSbTe thin films can be switched 10^8 times.[21,22] Another cell based on phase-change memory reached 10^{12} SET/RESET cycles.[23] The thermal stability of the amorphous phase is also outstanding. For a 60 nm wide $Ge_2Sb_2Te_5$ nanowire the data retention time can be as long as 25 years at 80 ^oC via isothermal characterization at different temperatures.[24] Although down-scaling the nanowires decreases the data retention time, the amorphous phase of a 30 nm wide nanowire is still stable for ~5 years at 80 °C.[24] Furthermore, doping the PCMs with proper elements, such as Cu,[25] Sn,[26] Al,[27] C,[28,29] and N,[30] increases the activation energy for crystallization and increases the thermal stability. For instance 2.7% of Al doping increased the activation energy of GeTe thin film from 3.14 to 5.56 eV. The crystallization temperature then also increased from 179 °C for GeTe to 277 °C for 3.6% Al-doped GeTe film.[27]

1.3 Applications of phase-change materials

The remarkable properties of PCMs shown above enable their applications in many fields. The most successful application that PCMs achieved is data storage. Rewritable optical data storage has been commercially used and is based on the difference in reflectivity between the amorphous and crystalline phases of the PCMs. The phase-change thin films (GeSbTe ternary alloy or AgInSbTe) are usually sandwiched between two dielectric layers, ZnS-SiO2. A laser beam is used to read, write and erase the data. Three generations of rewritable optical data storage have been developed. Rewritable compact discs (CDs) using a 780 nm laser were firstly released in early 1990s, containing a capacity of 500 MB. Then the digital versatile discs (DVDs) increase the storage ability to 4.7 GB using a 650 nm laser and smaller feature size. The third generation is the Blu-ray discs with single (25 GB) and dual layer (50 GB) using a 405 nm laser.[8]

Another promising application of PCMs is PCRAM that is based on the resistivity difference between amorphous and crystalline phases. The amorphous phase has a resistivity usually 3-4 orders of magnitude higher than the crystalline state. The pulse used to read the memory state is low enough to avoid the phase transition of the materials. The phase-change memory has long been considered as the most promising candidate to replace the popular Flash memory, but this recently changed towards application as storage-class memory. Comparing to the long write/erase time (in the scale of μs/ms) of Flash, the PCMs require much less time (in the time scale of tens of ns).[31] This time can be even reduced into a few ns by either decreasing the cell size or pre-annealing the PCMs.[18,32] Another advantage of PCRAM is that it has better endurance, i.e., more write/erase cycles compared to Flash memory (10^9 vs 10^5).[31] Moreover, the voltage needed for the write operation for PCMs is lower than the one of Flash memory (3 vs 12 V). There are also some other contenders for the storage-class memory, such as ferroelectric RAM, magnetic RAM, resistive RAM etc.. Scalability and cost will mainly decide which technology will dominate the storage-class memory area, but the strong scalability of the PCRAM make it a strong candidate.[33] The phase-change memory is also used in neuromorphic computing, where nanoscale phase-change memory was used.[34] Recently GeSbTe PCMs were used for display and data visualization purposes.[35]

1.4 Down-scaling ability of phase-change materials

The ability to store information develops along with the human development. From the hieroglyphs in ancient Egypt and oracle in China to the movable type printing in eleven century in China, the search for faster information storage drives the improvement of data storage along the history. The amount of created information did not explode until the invention of the computer and the internet. The generated data doubles almost every two years.[36] The gap between the data generation and storage supply is becoming wider with time. Down-scaling the storing unit provides a promising way to increase the storage capacity.[37] Moreover, it offers more intriguing properties for applications such as, high speed switching and low power consumption per bit.[38] Before the usage of the PCMs in down scaled devices, it is necessary to understand the behaviors of the PCMs shrunk to the feature size of the devices. Therefore many efforts have been devoted to studying the down-scaling of the PCMs.

$Ge_2Sb_2Te_5$ thin films with thickness ranging from 30 to 5 nm were deposited and capped by or sandwiched between ZnS-SiO_2 films using magnetron sputtering.[39] The crystallization temperature was then characterized by resistivity measurements. A clear thickness dependence in crystallization temperature was observed, where it increased from 138 to 157 ^{o}C for a heating rate of 0.5 ^{o}C/min when the thickness reduced from 30 to 5 nm.[39] In another work, similar trends were detected for other PCMs, like GST, N-doped GST, Sb_2Te and GeSb thin films sandwiched between SiO_2 and Al_2O_3 layers.[40] This work also showed that at the ultimate thickness of 1.5 nm crystallization did not take place anymore. However, for GST thin films sandwiched between SiO_2 and SiN layers the crystallization temperature was found independent of the thickness when the thickness decreased from 87 to 11 nm.[41] Still, the rock-salt to rhombohedral structure transition temperature was significantly decreased with the reduction of film thickness. The capping layers play an important role in crystallization, especially when the films become thinner as for instance the boundary induced heterogeneous nucleation and the stress field induced by the capping layer become more important. It has been observed that the SiN layer can facilitate the nucleation process for GST thin films while SiO_2 layer retards it.[42] Also it was found that at the metal/PCMs interfaces, like W/GeSb and Al/GeSb, the crystallization process is facilitated, especially when the film thickness is below 5 nm.[43] The crystallization time as a function of film thickness has been investigated as well. An increase of crystallization time was found with the decreasing of film thickness for nucleation-dominated PCMs (GST), while the opposite trend was detected for growth-dominated PCMs (AIST).[32,44]

Two dimensional down scaling of PCMs has been achieved by the VLS (vapour-liquid-solid) process.[24,45] The GST nanowires with widths shrinking from 200 to 30 nm were synthesized. Strong size dependency of the activation energy for crystallization was detected, where it decreased from 2.34 eV for a 200 nm nanowire to 1.9 eV for a 20 nm nanowire. The surface-induced heterogeneous nucleation was proposed to be responsible for the size dependency.[45] The writing current and power consumption decrease from 1.4 mA (100 ns) and 2.8 mW for 200 nm width nanowire to 0.16 mA and 0.7 mW for a 30 nm width nanowire.[24] Similar effects have also been observed for GeTe nanowires.[46]

When the phase-change memory is further scaled down in three dimensions, the active area of PCMs is like a (semi) nanoparticle. Thus, size dependent properties become crucial before using PCMs in phase-change devices. The first success was achieved using GeTe nanoparticles. By chemical synthesis, both amorphous and crystalline GeTe nanoparticles with average diameter down to 1.8 nm were produced. These nanoparticles showed a strong size dependence of the crystallization temperature,[47,48] where the crystallization temperature reaches ~400 ^oC for nanoparticles with a diameter of 1.8 nm, a huge increase in comparison to the bulk GeTe (~175 ^oC). Size-dependent polar ordering was also observed in the rhombohedral phase of these nanoparticles.[49] $Ge_{15}Sb_{85}$ nanodots with average diameter around 18.5 nm were produced by self-assembled polymer lithography. These NPs showed a crystallization temperature close to the one for bulk GeSb. Yet, growing smaller NPs is not feasible because of the limitations of optical lithography. Due to its complex stoichiometry, preparation of GST nanoparticles with narrow size distribution, composition and crystallinity control has been for a long time a huge challenge. Pulsed laser ablation was utilized to prepare GST nanoparticles, but the limitation of this method is that the size of the obtained nanoparticles showed a large variation (5-50 nm).[50] An anomalous sequence of phase transitions was detected, in which the amorphous nanoparticle first changed to the rhombohedral structure and then to the rock-salt structure. Another group used magnetron sputtering to grow GST nanoparticles.[51] Another nanoscaled phase-change memory was achieved by depositing the PCMs in the nanogap between two carbon nanotubes electrodes.[38] The nanogaps were generated by electrical breakdown, in the size ranging from 20 to 300 nm. In this configuration programming currents of 0.5 and 5 μA for SET and RESET were achieved, respectively. The programming voltage and energy were highly scalable and could be below 1 V and 1 fJ per bit.[38] Variations in either composition or sizes can be found for all the GST nanoparticles described above. So, GST nanoparticles with better tunable size, crystallinity and composition control are necessary to obtain a sound understanding of the crystallization behavior of the nanoparticles.

1.5 Motivation

As can be deduced from the above literature review, research on phase-change nanoparticles with sizes smaller than achievable with (optical) lithography is highly relevant. Concerning the most important phase-change material $Ge_2Sb_2Te_5$, hardly any relevant research on nanoparticles appears present. Nanoparticles with relatively monodisperse size distribution have only been demonstrated in Ref. 51, although the finally obtained composition of these nanoparticles showed a relatively large deviation from the stoichiometric 2:2:5 composition. The crystallization temperature of these NPs was assessed from synchrotron X-ray diffraction, but the influence of the NP size on the crystallization temperature was not determined. In the present thesis it is shown that $Ge_2Sb_2Te_5$ NPs with better tunable size (in the range between 8 and 20 nm), crystallinity and composition control could be synthesized. Detailed structure, morphology and composition analysis was performed using transmission electron microscopy (TEM) based techniques. The crystallization temperature of the NPs based on very low heating rate was determined using in-situ heating TEM as well as the influence of the NP size on the crystallization temperature. In order to obtain a more complete understanding of the crystallization kinetics, ultrafast differential scanning calorimetry has been employed to crystallize single flake of NPs with controlled heating rates in the range from 10 K/s to 40000 K/s. The present thesis thus covers a large existing gap in literature on this highly relevant topic of phase-change nanoparticles.

1.6 Thesis outline

In the next chapter 2, the general methods applied throughout the thesis are described. The main emphasis is on: (1) the synthesis of phase-change nanoparticles based on magnetron sputtering and gas-phase aggregation, (2) the characterization of the NPs using TEM and in-situ heating in the TEM, (3) ultrafast DSC employing controlled heating rates up to 40000 K/s and finally on the models used to interpret the DSC data. In this thesis there are some repetitions on the introduction and equations for different chapters. These parts are kept so that one can directly read individual chapters as a whole story.

Chapter 3 focuses on the crystallization kinetics of Ge_7Sb_{93} thin films as obtained by Ultrafast DSC. Modeling the experimentally obtained DSC data allowed extraction of the crystal growth rate extrapolated over a large temperature range in-between the glass temperature and the melting temperature. By comparing the modeled crystal growth rate to directly measured experimental growth rates, we verified the validity of two different models, where one showed to be adequate and the other not. This work turned out very instrumental for selecting the more suitable model to further analyze the crystallization kinetics of GeSbTe nanoparticles.

Chapter 4 describes the preparation of GeSbTe NPs and subsequent characterization using transmission electron microscopy. The size dependence of crystallization temperature for the GeSbTe NPs was revealed by in-situ heating in TEM. Also observed is that the addition of minor amounts of CH_4 to the argon sputtering gas during the NPs production plays an important role in increasing the crystallization temperature of the NPs and thus in improving the stability of the amorphous phase.

Chapter 5 demonstrates the crystallization kinetics of the GeSbTe NPs produced by magnetron sputtering and gas aggregation. The kinetics was studied by ultrafast heating over a large range of heating rates in differential scanning calorimetry (DSC). By analyzing the data with numerical modelling the temperature dependent viscosity and crystal growth rate of the amorphous nanoparticles were unraveled and extrapolated over a large temperature range from the glass temperature to the melting temperature. CH_4 incorporation was found as an excellent method to improve the performance of the nanoparticles.

Chapter 6 shows the interaction of the GeSbTe nanoparticles with graphene as support film, studied by state-of-the-art aberration corrected scanning transmission electron microscopy. A large difference in coverage of the NPs has been observed between suspended graphene and graphene supported by an amorphous carbon film, showing the different attachment dynamics of the nanoparticles on graphene and graphene/carbon supports. After aging the nanoparticles, the oxidation dynamics of the nanoparticles was studied as well.

Finally, in chapter 7 the synthesis of GeTe NPs, their crystallization temperature as determined by (low rate) in-situ heating in TEM and their crystallization kinetics as determined by ultrafast DSC are presented also allowing the comparison in behavior of GeTe NPs with the one of GeSbTe NPs as presented in chapters 4 and 5.

References

(1) Waterman, A. T. *Phys. Rev.* **1923**, *21* (5), 540–549.

(2) A. Pearson; W. Northover; J. Dewald; W. Peck. *Advunces in Glass Technology*; Plenum Press: New York, 1962.

(3) Ovshinsky, S. R. *Phys. Rev. Lett.* **1968**, *21* (20), 1450–1453.

(4) Battle, J. H.; Lighty, P. E.; Shanefield, D. J. Solid state element comprising semiconductive glass composition exhibiting negative incremental resistance. US3448425 A, June 3, 1969.

(5) R.G. Neale; D.L.Nelson; G.E. Moore. *Electronics* **1970**, *43* (20), 56–60.

(6) Raoux, S. *Annu. Rev. Mater. Res.* **2009**, *39* (1), 25–48.

(7) Yamada, N.; Ohno, E.; Akahira, N.; Nishiuchi, K. 'ichi; Nagata, K. 'ichi; Takao, M. *Jpn. J. Appl. Phys.* **1987**, *26* (S4), 61.

(8) Wuttig, M.; Yamada, N. *Nat. Mater.* **2007**, *6* (11), 824–832.

(9) Intel And Micron Jointly Unveil Disruptive, Game-Changing 3D XPoint Memory, 1000x Faster Than NAND | HotHardware https://hothardware.com/news/intel-and-micron-jointly-drop-disruptive-game-changing-3d-xpoint-cross-point-memory-1000x-faster-than-nand.

(10) Pandian, R.; Kooi, B. J.; Palasantzas, G.; De Hosson, J. T. M.; Pauza, A. *Adv. Mater.* **2007**, *19* (24), 4431–4437.

(11) Pandian, R.; Kooi, B. J.; Palasantzas, G.; De Hosson, J. T. M.; Pauza, A. *Appl. Phys. Lett.* **2007**, *91* (15), 152103.

(12) Pandian, R.; Kooi, B. J.; Oosthoek, J. L. M.; van den Dool, P.; Palasantzas, G.; Pauza, A. *Appl. Phys. Lett.* **2009**, *95* (25), 252109.

(13) Ciocchini, N.; Laudato, M.; Boniardi, M.; Varesi, E.; Fantini, P.; Lacaita, A. L.; Ielmini, D. *Sci. Rep.* **2016**, *6*.

(14) Lencer, D.; Salinga, M.; Wuttig, M. *Adv. Mater.* **2011**, *23* (18), 2030–2058.

(15) Siegrist, T.; Jost, P.; Volker, H.; Woda, M.; Merkelbach, P.; Schlockermann, C.; Wuttig, M. *Nat. Mater.* **2011**, *10* (3), 202–208.

(16) Yamada, N.; Ohno, E.; Nishiuchi, K.; Akahira, N.; Takao, M. *J. Appl. Phys.* **1991**, *69* (5), 2849–2856.

(17) Bruns, G.; Merkelbach, P.; Schlockermann, C.; Salinga, M.; Wuttig, M.; Happ, T. D.; Philipp, J. B.; Kund, M. *Appl. Phys. Lett.* **2009**, *95* (4), 043108.

(18) Loke, D.; Lee, T. H.; Wang, W. J.; Shi, L. P.; Zhao, R.; Yeo, Y. C.; Chong, T. C.; Elliott, S. R. *Science* **2012**, *336* (6088), 1566–1569.

(19) Lankhorst, M. H. R.; Ketelaars, B. W. S. M. M.; Wolters, R. a. M. *Nat. Mater.* **2005**, *4* (4), 347–352.

(20) Pirovano, A.; Lacaita, A. L.; Benvenuti, A.; Pellizzer, F.; Bez, R. *IEEE Trans. Electron Devices* **2004**, *51* (3), 452–459.

(21) Horii, H.; Yi, J. H.; Park, J. H.; Ha, Y. H.; Baek, I. G.; Park, S. O.; Hwang, Y. N.; Lee, S. H.; Kim, Y. T.; Lee, K. H.; Chung, U.-I.; Moon, J. T. In *2003 Symposium on VLSI Technology. Digest of Technical Papers (IEEE Cat. No.03CH37407)*; 2003; pp 177–178.

(22) Yi, J. H.; Ha, Y. H.; Park, J. H.; Kuh, B. J.; Horii, H.; Kim, Y. T.; Park, S. O.; Hwang, Y. N.; Lee, S. H.; Ahn, S. J.; Lee, S. Y.; Hong, J. S.; Lee, K. H.; Lee, N. I.; Kang, H. K.; Chung, U.-I.; Moon, J. T. In *IEEE International Electron Devices Meeting 2003*; 2003; p 37.3.1-37.3.4.

(23) Lai, S.; Lowrey, T. In *International Electron Devices Meeting. Technical Digest (Cat. No.01CH37224)*; 2001; p 36.5.1-36.5.4.

(24) Lee, S.-H.; Jung, Y.; Agarwal, R. *Nat. Nanotechnol.* **2007**, *2* (10), 626–630.

(25) Raoux, S.; Salinga, M.; Jordan-Sweet, J. L.; Kellock, A. *J. Appl. Phys.* **2007**, *101* (4), 044909.

(26) Lee, M. L.; Yong, K. T.; Gan, C. L.; Ting, L. H.; Daud, S. B. M.; Shi, L. P. *J. Phys. Appl. Phys.* **2008**, *41* (21), 215402.

(27) Ren, K.; Rao, F.; Song, Z.; Peng, C.; Li, J.; Wu, L.; Liu, B.; Feng, S. *Appl. Phys. Lett.* **2013**, *103* (9), 093111.

(28) Zhou, X.; Wu, L.; Song, Z.; Rao, F.; Zhu, M.; Peng, C.; Yao, D.; Song, S.; Liu, B.; Feng, S. *Appl. Phys. Lett.* **2012**, *101* (14), 142104.

(29) Zhou, X.; Xia, M.; Rao, F.; Wu, L.; Li, X.; Song, Z.; Feng, S.; Sun, H. *ACS Appl. Mater. Interfaces* **2014**, *6* (16), 14207–14214.

(30) Seo, H.; Jeong, T.-H.; Park, J.-W.; Yeon, C.; Kim, S.-J.; Kim, S.-Y. *Jpn. J. Appl. Phys.* **2000**, *39* (2S), 745.

(31) Wong, H.-S. P.; Raoux, S.; Kim, S.; Liang, J.; Reifenberg, J. P.; Rajendran, B.; Asheghi, M.; Goodson, K. E. *Proc. IEEE* **2010**, *98* (12), 2201–2227.

(32) Wang, W. J.; Shi, L. P.; Zhao, R.; Lim, K. G.; Lee, H. K.; Chong, T. C.; Wu, Y. H. *Appl. Phys. Lett.* **2008**, *93* (4), 043121.

(33) Burr, G. W.; Kurdi, B. N.; Scott, J. C.; Lam, C. H.; Gopalakrishnan, K.; Shenoy, R. S. *IBM J. Res. Dev.* **2008**, *52* (4.5), 449–464.

(34) Tuma, T.; Pantazi, A.; Le Gallo, M.; Sebastian, A.; Eleftheriou, E. *Nat. Nanotechnol.* **2016**, *11* (8), 693–699.

(35) Hosseini, P.; Wright, C. D.; Bhaskaran, H. *Nature* **2014**, *511* (7508), 206–211.

(36) J. Grantz; D. Reinsel. IDC iVIEW: IDC Analyze the future 2012.

(37) Hamann, H. F.; O'Boyle, M.; Martin, Y. C.; Rooks, M.; Wickramasinghe, H. K. *Nat. Mater.* **2006**, *5* (5), 383–387.

(38) Xiong, F.; Liao, A. D.; Estrada, D.; Pop, E. *Science* **2011**, *332* (6029), 568–570.

(39) Wei; Xiaoqian; Shi; Luping; Chong; Chong, T.; Zhao; Rong; Lee; Koon, H. *Jpn. J. Appl. Phys.* **2007**, *46* (4S), 2211.

(40) Raoux, S.; Jordan-Sweet, J. L.; Kellock, A. J. *J. Appl. Phys.* **2008**, *103* (11), 114310-114310–114317.

(41) Peng, H. K.; Cil, K.; Gokirmak, A.; Bakan, G.; Zhu, Y.; Lai, C. S.; Lam, C. H.; Silva, H. *Thin Solid Films* **2012**, *520* (7), 2976–2978.

(42) Ohshima, N. *J. Appl. Phys.* **1996**, *79* (11), 8357–8363.

(43) Raoux, S.; Cheng, H.-Y.; Jordan-Sweet, J. L.; Muñoz, B.; Hitzbleck, M. *Appl. Phys. Lett.* **2009**, *94* (18), 183114.

(44) Zhou, G.-F.; Jacobs, B. A. J. *Jpn. J. Appl. Phys.* **1999**, *38* (3S), 1625.

(45) Lee, S.-H.; Jung, Y.; Agarwal, R. *Nano Lett.* **2008**, *8* (10), 3303–3309.

(46) Lee, S.-H.; Ko, D.-K.; Jung, Y.; Agarwal, R. *Appl. Phys. Lett.* **2006**, *89* (22), 223116.

(47) Caldwell, M. A.; Raoux, S.; Wang, R. Y.; Wong, H.-S. P.; Milliron, D. J. *J. Mater. Chem.* **2010**, *20* (7), 1285–1291.

(48) Arachchige, I. U.; Soriano, R.; Malliakas, C. D.; Ivanov, S. A.; Kanatzidis, M. G. *Adv. Funct. Mater.* **2011**, *21* (14), 2737–2743.

(49) Polking, M. J.; Urban, J. J.; Milliron, D. J.; Zheng, H.; Chan, E.; Caldwell, M. A.; Raoux, S.; Kisielowski, C. F.; Ager, J. W.; Ramesh, R.; Alivisatos, A. P. *Nano Lett.* **2011**, *11* (3), 1147–1152.

(50) Yoon, H. R.; Jo, W.; Lee, E. H.; Lee, J. H.; Kim, M.; Lee, K. Y.; Khang, Y. *J. Non-Cryst. Solids* **2005**, *351* (43–45), 3430–3434.

(51) Ghezzi, G. E.; Morel, R.; Brenac, A.; Boudet, N.; Audier, M.; Fillot, F.; Maitrejean, S.; Hippert, F. *Appl. Phys. Lett.* **2012**, *101* (23), 233113.

Chapter 2

Methods

Abstract

This chapter describes the general methods utilized to prepare samples and the subsequent methods employed for sample characterization and data analysis. Two different routes were pursued to study the crystallization behavior of the phase-change materials: (1) slow crystallization by in-situ heating in a transmission electron microscope and (2) fast crystallization by ultrafast heating in differential scanning calorimetry. The analytical methods adopted and described here are the basis for the analyses performed and presented in the next chapters. Specific deviations of these general methods will be mentioned in the chapters separately.

2.1 Sample preparation

In this thesis, Ge_7Sb_{93} thin films and $Ge_2Sb_2Te_5$ (GST) nanoparticles were studied. Amorphous Ge_7Sb_{93} films with thickness of 200 nm were deposited on glass substrates using co-sputtering with a Unaxis Sputter coater. The deposition rate was 2.5 nm s^{-1}. The films were, without breaking the vacuum, directly capped with a (5 nm) layer of ZnS-SiO_2 to avoid oxidation of the films.

The phase-change nanoparticles (NPs) were produced by magnetron sputtering with inert gas condensation in a home-modified nanoparticle system Nanosys50 from Mantis Deposition Ltd. (http://www.mantisdeposition.com). The setup is shown in Figure 2.1. This system consists of two chambers, i.e., the main chamber (indicated by the left dashed square in Figure 2.1a) and the aggregation chamber (marked by the right dashed rectangle in Figure 2.1a).

The main chamber is used to collect the produced NPs. The substrate for the sample is placed in the holder that locates in the main chamber. Up to 10 samples can be put into the sample holder (in 5 arrays), enabling the production of NPs at five different settings without opening the system. Two Leybold turbo molecular pumps with a capacity of 300 lt/s are present to evacuate the two chambers and they are both backed by one scroll pump (Varian LTH10). The vacuum can reach $1x10^{-8}$ mbar in the main chamber and $1x10^{-6}$ mbar in the aggregation chamber. The settings and vacuum are controlled and monitored by the Mantis controller, as shown in Figure 2.1b.

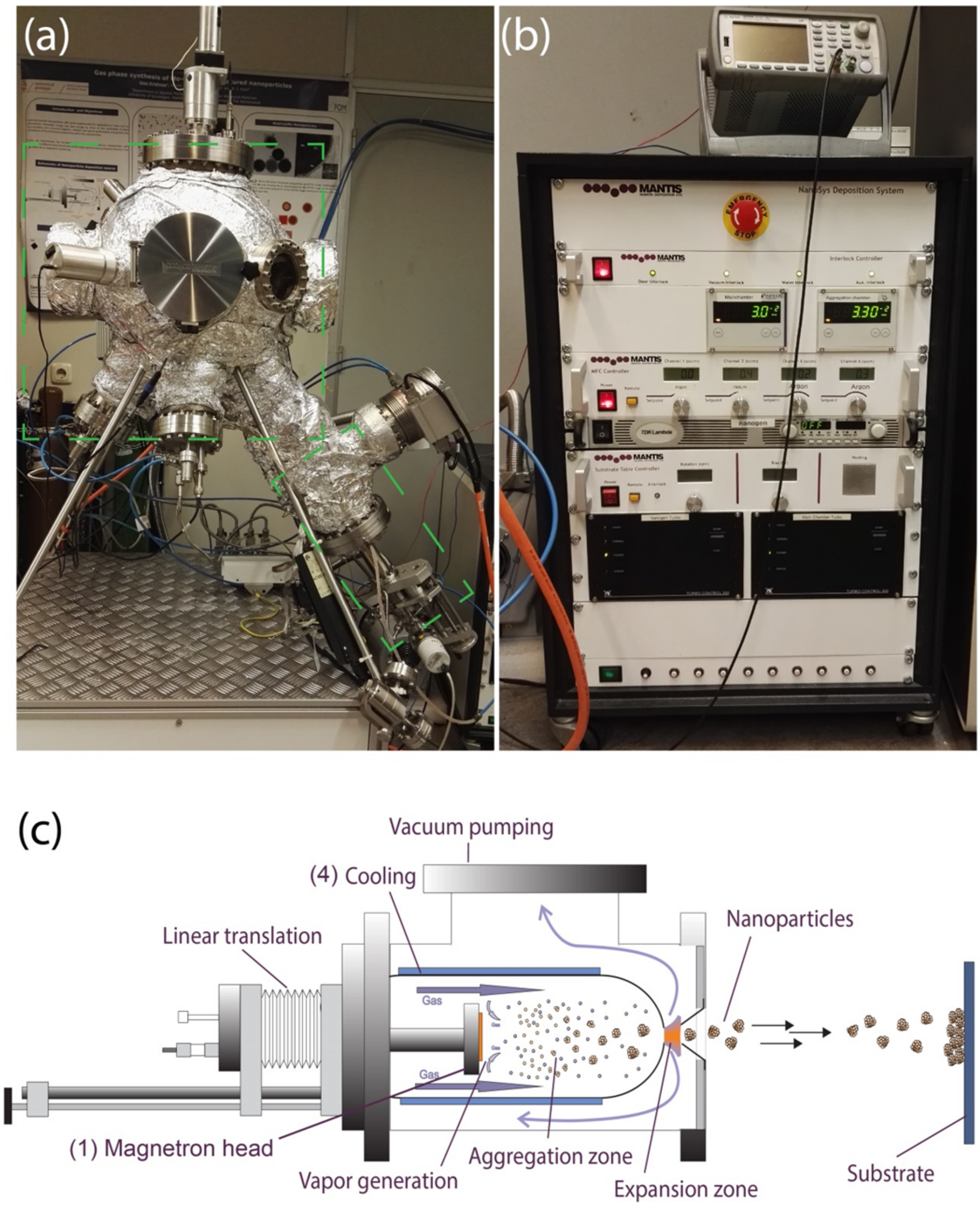

Figure 2.1 The cluster source for producing nanoparticles (a) and the corresponding controller (b). The schematic of the aggregation chamber is shown in (c).

The aggregation chamber is the core of the system, which is schematically illustrated in Figure 2.1c. It consists of several parts: (1) a water cooled magnetron head, (2) a double gas inlet system controlled by 2 MKS mass flow meters, (3) pressure readings inside the aggregation chamber and the main chamber and (4) water cooling for both the magnetron head and aggregation chamber wall. A target (2 inches in diameter and with tunable thickness) is placed on top of the magnet head. On top of the target a cylindrical anode is mounted, connected to a TDK-Lambda Genesys Gen 600-1.3 programmable DC power supply with a range up to 600 V and 1.3 A. During deposition the power can be controlled by a build-in voltage and current limiter. Inert gas is used as sputtering gas to minimize the possible interference with the target materials. The gas has three functions throughout the sputtering process: first sputtering, then cooling of the target material vapor, and then finally transporting the formed NPs.

The mechanism of magnetron sputtering can be summarized as follows. When a deposition starts, a noble gas (usually Ar in this thesis) is flown into the aggregation zone. Due to the applied potential between the target and the anode, the inert gas is ionized above the magnetron head to create a plasma. Then the positive ions in the plasma (Ar^+) are accelerated by the DC potential and impacts on the target, thereby breaking off particles which together compose the desired target material vapor. The magnetron under the target can increase the efficiency of the sputtering process by making the ions travel in a helical path through the plasma, leading to the longer effective path therefore higher chance of colliding with the target. The target material vapor is then swept to the aggregation volume that is just above the plasma. The relatively high pressure caused by the inert gas and the cooling limit the vapors mean free path, resulting in the supersaturation in which nucleation and growing of the cluster can take place.

After their growth the NPs are swept to the main chamber through the small nozzle because of the much higher pressure in the aggregation chamber in comparison to the main chamber. Hydrogen or methane was used to facilitate the formation of nascent clusters during the deposition process.[1] Note that the amount of hydrogen or methane used, supplied using a needle valve, could only be specified qualitatively, because a gauge measuring the gas flow precisely was lacking. The NPs then land on the substrates located in the sample holder in the main chamber. The deposition rate can be monitored by a home-built quartz crystal microbalance (QCM) placed slightly off-center of the conical NPs beam.

There are some parameters that can affect the size and crystallinity of the as-deposited NPs. (1) The length of the aggregation volume can influence the size of the NPs. A longer length provides a longer time and length for the NPs to grow. (2) The addition of He gas (to the Ar) tends to decrease the size of the NPs. Due to the higher thermal conductivity of He compared to Ar, He can cool down the supersaturated vapor faster leading to reduced NPs growth. (3) The discharge current can influence the phase of the as-deposited phase-change NPs. High discharge current (0.3-0.35 A) results in crystalline NPs while amorphous NPs are produced at low current. (4) A backing plate (usually copper) underneath the target reduces the size of the NPs significantly. The thicker the backing plate is, the smaller the NPs become. Adjusting the above parameters, we have been able to tune the size and crystallinity of the as-deposited phase-change NPs.

2.2 Morphology characterization

The morphology, crystallographic structure and the stoichiometry of the NPs were characterized by transmission electron microscope (TEM) at 200 kV. The phase-change NPs were directly deposited on the TEM grids (holey/continuous carbon or silicon nitride membranes). The composition of the NPs was characterized by energy disperse X-ray spectrometry (EDS) attached to the TEMs (Thermo Instruments on the JEOL 2010 and Bruker Quantax on the JEOL 2010F). The crystal structure of the crystalline phase-change NPs were investigated by high resolution TEM (JEOL 2010F).

2.3 Crystallization

In this thesis, two kinds of crystallization were performed to the phase-change NPs, i.e., slow crystallization and ultrafast crystallization. The slow crystallization were performed to study the size dependence of crystallization temperature for the phase-change NPs, while the ultrafast heating was conducted to study the crystallization kinetics of the phase-change NPs at high temperature.

2.3.1 Slow crystallization

The slow crystallization of the phase-change nanoparticles was studied by in-situ heating in TEM. A single tilt heating holder (Gatan Model 628) with the temperature controlled by a SmartSet Hot Stage controller (Gatan Model 901, with temperature accuracy of 0.1 ^{o}C) was used for in-situ heating. The selected area electron diffraction patterns probing at the same area were recorded at different temperatures; an example for GST NPs is shown in Figure 2.2. The specific heating procedure applied to the various samples are detailed in chapter 4. Then the azimuthal integration procedure was applied to the diffraction patterns recorded at different temperatures. This integration procedure derives in a straightforward manner the intensities for different diffraction rings as function of the distance in reciprocal space to the diffraction centre point, as shown in Figure 2.2c. This integration was performed by the PASAD plug-in (http://www.univie.ac.at/-pasad/) in Digital Micrograph software in order to derive the evolution of the diffraction intensity with temperature. Since the diffraction intensity is directly related to the crystallinity of the NPs, we can obtain the crystallization fraction as a function of temperature by taking peak intensity of certain reflection (220 in Figure 2.2d) at various temperatures, as demonstrated in Figure 2.2d. Fitting this plot with the Boltzmann function, as shown in the red dashed curve in Figure 2.2d, the crystallization temperature of this sample was then derived. The crystallization temperature was defined as the temperature at which the maximum 1st order derivative takes place in the fitting curve, as indicated by the red arrow in Figure 2.2d.

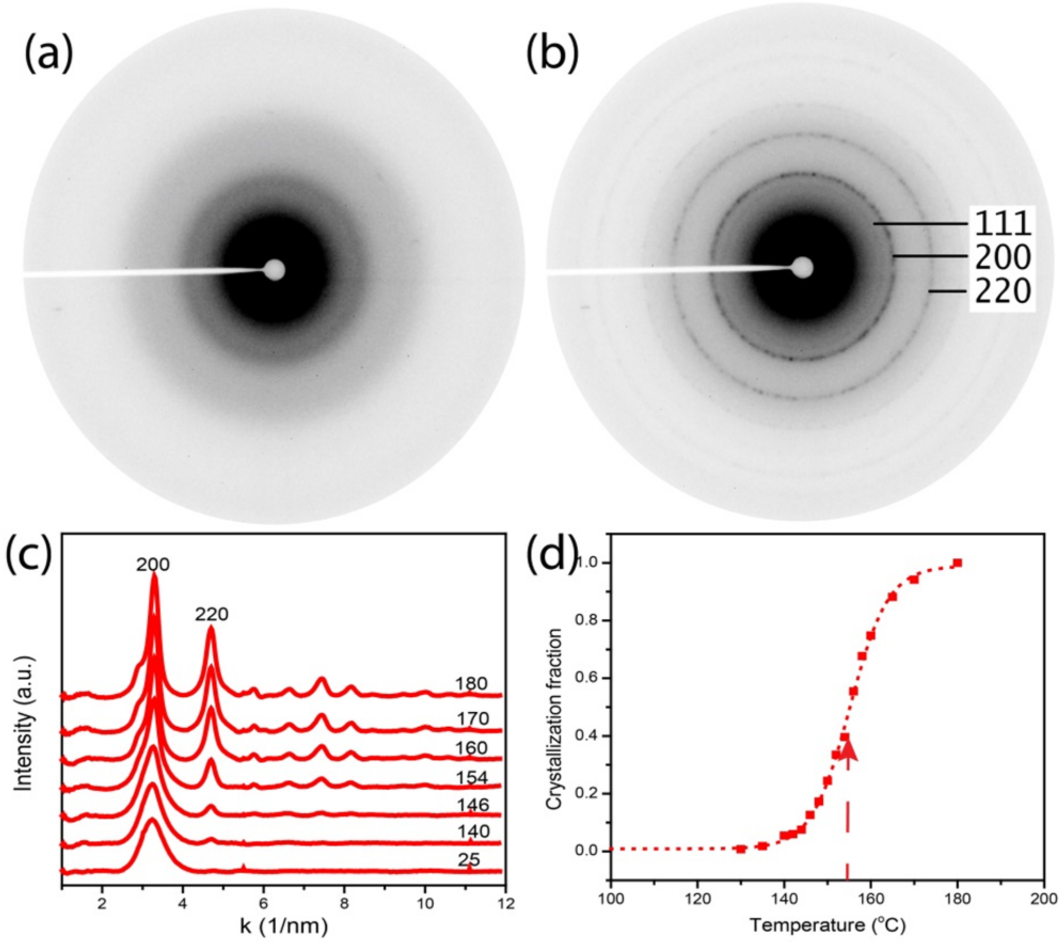

Figure 2.2 Selected area electron diffraction pattern at 25 °C (a) and 180 °C (b). (c) showing the diffraction intensities of different crystal planes at corresponding temperatures and (d) demonstrating the crystallization fraction as a function of temperature. The unit for temperature in (c) is °C.

2.3.2 Ultrafast crystallization

The ultrafast crystallization of the phase-change NPs has been performed by ultrafast differential scanning calorimetry (DSC, Mettler-Toledo Flash DSC 1), as demonstrated in Figure 2.3a. A special chip sensor (USF-1, see Figure 2.3b), containing the active area for heating the sample and the reference area, is used for the ultrafast heating. Figure 2.3c shows a zoomed-in image of an active area of the chip sensor, with a single-flake specimen transferred onto the area. The active area of the chip sensor is only at the central square, in dimension 250×250 μm^2. Unlike traditional

DSC that can only heat and cool the materials up to ~200 K/min, the ultrafast DSC is able to heat the sample with a maximum rate of 40 000 K/s and cool it with a maximum rate of ~10 000 K/s. This ultrafast heating rate thus enables us to investigate the crystallization kinetics of phase-change materials at high heating rate.

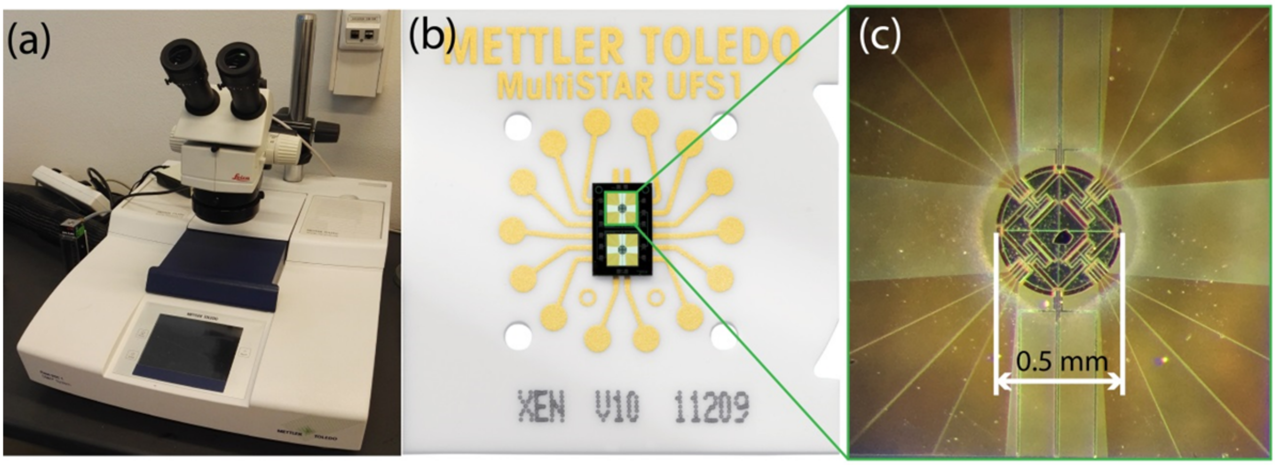

Figure 2.3 The Mettler Toledo ultrafast differential scanning calorimeter used for the present thesis work (a) and the accompanying chip sensor used for the heating (b). (c) shows a zoomed-in image of the active area of a chip sensor on which a small sample (flake containing NPs) is present.

The amorphous phase-change materials that were deposited on pre-cleaned substrates (an example shown in Figure 2.4a) were scraped off into small pieces. Note that a silicon nitride membrane (dedicated TEM grid) was fixed relatively far off-center with respect to the NPs beam hitting the substrate (see Figure 2.4a), in order to reduce the NPs coverage for the aim of characterizing the morphology of the as-deposited individual NPs. Then the materials from the high coverage area in the center of the NPs beam were transferred onto the active area of the chip sensor by a hair, as shown in Figure 2.3c. The materials were then crystallized at different heating rates. Note that in this thesis only crystallization of the phase-change materials can be conducted, because the amorphization of the crystalline phase-change materials requires extremely high cooling rate that is beyond the maximum cooling rate of the system. So the crystallized sample has to be removed from the chip sensor after each heating run in order to analyze a next sample. To minimize the oxidation of the materials during heating, a steady N_2 gas flow is introduced.

Heating rates varying from 10 to 40 000 K/s were used for the phase-change materials. At each heating rate, measurements were repeated at least 3 times for low heating rates and 5-10 times for high heating rates, as the crystallization temperatures become more scattered at high heating rates.

Figure 2.4b demonstrates an example of the DSC traces for GST NPs at 250 K/s and 5 000 K/s. In the DSC traces at 250 K/s, an exothermic peak can be obviously observed around 190 ^{o}C (T_{p1}). This peak corresponds to the amorphous to rock-salt structural transition according to previous (conventional) DSC measurements.[2] When the heating rate is increased, for instance to 5 000 K/s, the T_{p1} shifts to 215 ^{o}C. The crystallization kinetics (such as activation energy, crystal growth rate, viscosity) can be then obtained by investigating the T_{p1} at various heating rates ranging from 10 to 40 000 K/s in combination with proper modeling. In Figure 2.4b, a second exothermic peak that relates to the rock-salt to rhombohedral structural transition can be detected in the trace at 5 000 K/s.

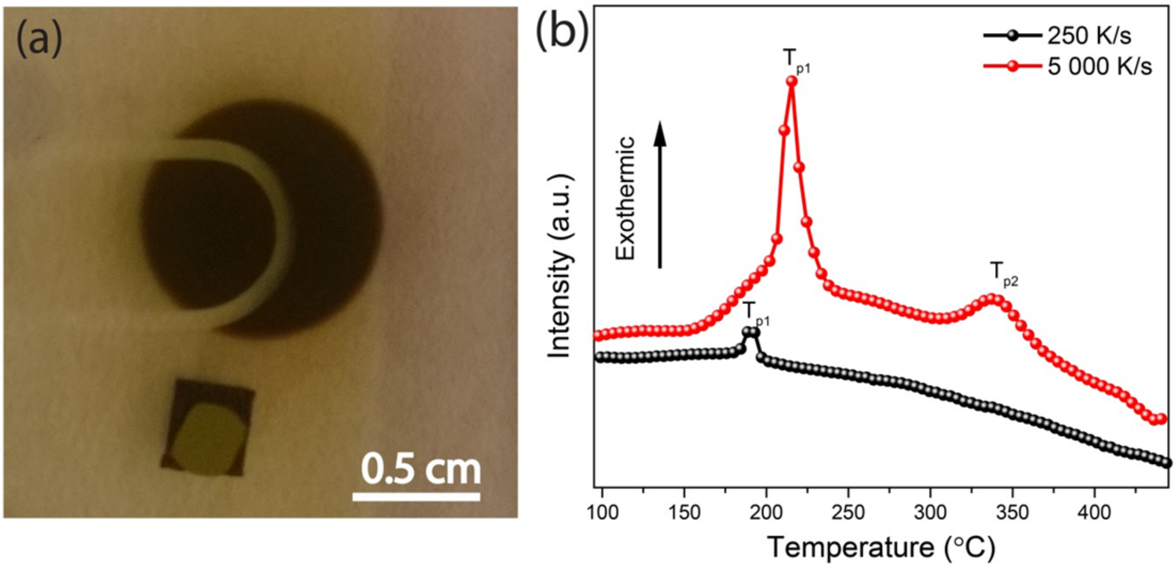

Figure 2.4 The as-deposited GST NPs on a glass substrate (a) for the ultrafast DSC measurements and the corresponding DSC traces at different heating rates (b).

2.4 Numerical modeling

In order to understand the crystallization kinetics of the phase-change materials from the data obtained by ultrafast heating, numerical modeling relying on Johnson-Mehl-Avrami-Kolmogorov (JMAK) theory and growth rate models was performed to simulate the DSC traces for different heating rates.[3–7] Then the modeled crystallization temperatures at different heating rates are fitted to the experimental data by adjusting the parameters in the model. After the fitting, the temperature dependent viscosity and crystal growth rate are derived from the fitted models.

Due to the constant heating rate applied, the heating was for the modeling segmented into a series of small isothermal steps (here we took 0.05 K as step size). At each isothermal step the crystals grew at a given growth rate with a certain shape (i.e. spheres for 3-dimensional growth or flat cylinders for 2-dimensional growth in the thin film flakes). At the end of each temperature, the extended transformed volume can be calculated and therefore the real transformed volume can be obtained, according to JMAK theory. In order to calculate the extended volume descriptions of both nucleation and growth are required.

2.4.1 JMAK theory

In classical JMAK theory, the extended transformed space X_e can be described as:[5,6,8,9]

$$X_e = f\int_0^t I(t)\left[\int_\tau^t u(t)dt\right]^n d\tau \tag{2.1}$$

in which $I(\tau)$ is the time-dependent nucleation rate (per unit of untransformed space) and $u(t)$ is the time-dependent growth rate of the crystals. f and n are shape factors related to the growth shape; i.e. for circular growth in 2 dimensions f and n are π and 2, respectively, and for spherical growth in 3 dimensions f and n are $4\pi/3$ and 3, respectively. The nucleation for the $Ge_2Sb_2Te_5$ thin film (which is a nucleation dominant phase-change material) can be treated using a constant density of pre-existing nuclei (site saturation).[10] In this dissertation, we also adopted this assumption to simplify the modeling. The justification of this simplification will demonstrated in chapter 3 and 5 for Ge-Sb thin film and GeSbTe nanoparticles. We can simplify X_e as:

$$X_e = fN\left[\int_0^t u(t)dt\right]^n \tag{2.2}$$

with N the density of pre-existing nuclei (per unit of untransformed space).

The real transformed space ($X(t)$) can then, according to the JMAK formulism, be directly related to the extended transformed space:

$$X(t) = 1 - \exp[-X_e(t)] \tag{2.3}$$

If we assume that the changing rate of enthalpy (dH/dt) scales linearly with the changing rate of the real transformed space, then the DSC signal can be written as:[11]

$$\text{DSC signal: } \propto \frac{X(T+\delta T) - X(T)}{\delta t} \tag{2.4}$$

with $X(T)$ the real transformed volume at temperature T, δt the time consumed for each isothermal step. In this case, δt is inversely proportional to heating rate ($\delta t = \delta T/\Phi$). Therefore the DSC traces can be modeled based on the above JMAK theory. It is also noticeable that higher heating rates lead to increments of the (area under) exothermic peaks in the DSC traces at higher temperatures.

2.4.2 Crystal growth models

Two models were used in this dissertation to describe the kinetics of the phase-change materials. One is from the work of *Orava* et al.,[10] which is based an expression by *Cohen* and *Grest* (CG model) for the viscosity of glass-forming liquids.[12] The other one is based on the work of *Salinga et al.*[13] who used the MYEGA model for the description of the viscosity of supercooled liquids.[14] The details of these models will be provided in chapter 3. The validity of these two models were verified by comparing the measured crystal growth rate for GeSb thin films with the modeled data from both the models. Note that these above two viscosity models only predict a continuous decrease in slope of the viscosity versus temperature for increasing temperature above the glass temperature. Therefore, these models, although accounting for differences in strong to fragile liquid behavior, can only describe relatively basic viscosity behaviour. For the data obtained by ultrafast heating of GeSbTe NPs this basic behavior turned out insufficient and then a generalized MYEGA model for viscosity, whose details are provided in chapter 5, was utilized to model the DSC traces and fit to the experimental data.

References

(1) Krishnan, G.; Graaf, S. de; Brink, G. H. ten; Persson, P. O. Å.; Kooi, B. J.; Palasantzas, G. *Nanoscale* **2017**, *9* (24), 8149–8156.

(2) Yamada, N.; Ohno, E.; Nishiuchi, K.; Akahira, N.; Takao, M. *J. Appl. Phys.* **1991**, *69* (5), 2849–2856.

(3) A.N. Kolmogorov. *Bull Acad Sci USSR Math Ser* **1937**, *1*, 355–359.

(4) W.A. Johnson, R.F. Mehl. *Trans Aime* **1939**, *135* (8), 396–415.

(5) Avrami, M. *J. Chem. Phys.* **1939**, *7* (12), 1103–1112.

(6) Avrami, M. *J. Chem. Phys.* **1940**, *8* (2), 212–224.

(7) Avrami, M. *J. Chem. Phys.* **1941**, *9* (2), 177–184.

(8) Kooi, B. J. *Phys. Rev. B* **2004**, *70* (22), 224108.

(9) Kooi, B. J. *Phys. Rev. B* **2006**, *73* (5), 054103.

(10) Orava, J.; Greer, A. L.; Gholipour, B.; Hewak, D. W.; Smith, C. E. *Nat. Mater.* **2012**, *11* (4), 279–283.

(11) Kelton, K. F. *Mater. Sci. Eng. A* **1997**, *226–228*, 142–150.

(12) Cohen, M. H.; Grest, G. S. *Phys. Rev. B* **1979**, *20* (3), 1077–1098.

(13) Salinga, M.; Carria, E.; Kaldenbach, A.; Bornhöfft, M.; Benke, J.; Mayer, J.; Wuttig, M. *Nat. Commun.* **2013**, *4*.

(14) Mauro, J. C.; Yue, Y.; Ellison, A. J.; Gupta, P. K.; Allan, D. C. *Proc. Natl. Acad. Sci.* **2009**, *106* (47), 19780–19784.

Chapter 3

Crystallization kinetics of Ge-Sb films

Abstract

The crystallization kinetics of phase-change materials (PCMs) entail a crucial aspect of phase-change memory technology and their study is also of interest to advance the understanding of crystallization in general. Research on crystallization of PCMs remains challenging because of the short (nanosecond) time and small (nanometer) length scales involved. Ultrafast differential scanning calorimetry (DSC) offers a powerful tool to study crystallization via ultrahigh heating rates. Here, we used this tool to study the crystallization kinetics of growth-dominant Ge_7Sb_{93}. Two models describing the viscosity of the undercooled liquid were used to interpret the data and were subsequently crosschecked by independent growth-rate data. With both models the data in Kissinger plots could be fitted well, but one of the models resulted in large discrepancy with the independent data. These results demonstrate that great care is needed when deriving crystal-growth rates from ultrafast DSC measurements because orders of magnitude errors can be made. The present analysis showed a slightly non-Arrhenius crystallization behaviour for the Ge_7Sb_{93} alloy, corresponding to a fragility of 65 and a glass transition temperature of 379 K. The overall viscosity and growth rate of this alloy between the glass and melting temperatures have been revealed, as well as a maximum growth rate of 21 m s^{-1} at ~800 K. Models based on ultrafast DSC data offer interpretation of crystallization kinetics of PCMs and thereby strongly support the design of PCMs for memory applications.

Based on *Crystallization Kinetics of Supercooled Liquid Ge–Sb Based on Ultrafast Calorimetry,*
B. Chen, J. Momand, P.A. Vermeulen, B. J. Kooi, *Crystal Growth & Design* 16.1, (2015),242.

3.1 Introduction

Memories based on phase-change materials (PCMs) demonstrate promising performances for a next generation memory technology.[1,2] PCMs can be switched rapidly and reversibly between amorphous and crystalline phases, offering large optical and electrical contrast. Lying at the heart of PCMs memory technologies, crystallization has aroused for many years a large number of investigations, e.g. though both experiments[3–10] and molecular dynamics simulations[11–14]. Most of the conventional experimental studies on crystallization of PCMs focused on the relatively low temperature region mainly because of limitations in instrumentation.[3,7–10] For instance, *Friedrich et al.*[10] studied the crystallization temperatures of $Ge_2Sb_2Te_5$ alloy via electrical resistance measurement by employing heating rates (Φ) from 0.53 to 5.3 K min^{-1} and strict Arrhenius behavior of crystal growth was found. Similar results were reported by *Park et al* [3] via differential scanning calorimetry (DSC) with Φ ranging from 5 to 20 K min^{-1}. The crystallization temperatures in these two cases are around 420 K. Crystallization kinetics at higher temperatures is not only of interest for theoretical studies but also remarkably important for the real application of PCMs because, due to the high switching speeds that have to be achieved in the applications, crystallization usually happens at the higher temperatures. However, research providing a comprehensive picture of crystallization kinetics involving these higher temperatures still remains a challenge due to the short time and small length scales involved.

Eising et al.[15] reported a direct method to measure the crystal growth rate at higher temperature for Ge_xSb_{1-x} alloys by employing a high speed optical camera and a laser to accelerate crystallization. The growth rate was measured over 5 orders of magnitude. However, the shortcoming of this method, as generally holds for laser-induced crystallization methods, is that the temperature of the sample cannot be directly measured, making it harder to arrive at a comprehensive picture of crystallization kinetics as a function of temperature. In another work, *Salinga et al.*[16] solved this problem by using a laser to only induce an amorphous mark in a thin film on a heater and then use laser-based time-resolved reflectivity measurements to determine the rate by which the mark recrystallizes from its rim at the known temperature set by the heater. A strict Arrhenius behavior in growth velocity from ~10 nm s^{-1} to ~1 m s^{-1} was observed for melt-quenched AgInSbTe (AIST).

Orava et al.[17] achieved important progress regarding the crystallization kinetics of PCMs at higher temperatures by employing ultrafast differential scanning calorimetry (DSC). In this way a large range of heating rates (from 50 to 40 000 K s^{-1}) can be applied, whereby crystallization in a relatively wide temperature range becomes available. Employing a model for viscosity by *Cohen* and *Grest* (the CG model),[18] the growth rate for a wide temperature range between glass and melting temperatures was derived. Strong non-Arrhenius behavior in crystallization kinetics of $Ge_2Sb_2Te_5$ (GST) films was discovered, due to fragile liquid behaviour of the (supercooled) liquid phase subjected to crystallization. This indicated a novel and promising approach to study the crystallization kinetics of PCMs at relatively high temperatures. However, the interpretation of the data obtained from ultrafast DSC is rather indirect and not straightforward. For instance, a very simplified description of nucleation and subsequently Johnson-Mehl-Avrami-Kolmogorov (JMAK) theory[19–23] was used to derive the growth rate of GST from the glass transition temperature (T_g) to the melting temperature (T_m). Moreover, directly measured crystal growth rate data were not used to verify the accuracy of their interpretation of the ultrafast DSC data. Meanwhile, the activation energy for growth provided by this model is clearly higher than that from the conventional measurements; see Figure 1 in (News & Views) perspective by *Wuttig et al.*.[24] Also it is readily observable in this figure that the absolute values obtained by this model are at least three orders of magnitude larger than the ones obtained from conventional measurements for the corresponding temperatures. Moreover, in a recent paper, *Orava et al.*[25] adopted the same method to study the crystallization of AgInSbTe, and a mismatch between the modeled Kissinger plot and the experimental data occurred for Φ above 200 K s^{-1}. These results therefore demonstrate that the derivation of the growth rate data from ultrafast DSC measurements has to be tested (more) carefully.

Here we present such an extensive analysis of ultrafast DSC data to comprehend the crystallization kinetics of Ge_7Sb_{93}. Two models (which we designated the MYEGA and CG models; see 3.3.2 for the details) describing the viscosity and growth rate have been adopted to understand the data. Independent growth rate data for the same alloy, obtained by an optical high speed camera where growth was accelerated by a laser, is used to crosscheck the accuracy of our analysis and the validity of the two models. It turns out that the growth rate obtained by the MYEGA model we adopted here leads to a much better match to the data, while that from the CG model shows 2-3 orders of magnitude overestimation of the growth rate at the measurable temperature region by ultrafast DSC. Results show that the MYEGA model for viscosity and growth rate appears appropriate for PCMs. With this model, ultrafast DSC provides us a novel and powerful method to understand the crystallization behavior of PCMs at a higher temperature which is inaccessible by conventional measurements.

3.2 Experimental and analysis methods

Amorphous Ge_7Sb_{93} films with thickness of 200 nm were deposited on glass substrates using co-sputtering with a Unaxis Sputter coater. The deposition rate was 2.5 nm s^{-1}. The films were, without breaking the vacuum, directly capped with a (5 nm) layer of ZnS-SiO_2. More details can be found in our previous work.[26]

Ultrafast heating was then conducted by differential scanning calorimetry for the flakes of the films. They were scraped off from the glass substrate, and then deposited on the active area of a chip sensor (keeping the reference area clean). Heating rates (Φ) in the measurements spanned about three orders of magnitude, i.e. ranged from 50 to 40000 K s^{-1}. The thermal lag between the chip sensor and the phase-change flake is shown in Appendix and it can be seen that the thermal lag dose not influence the shift of the crystallization peak temperature obtained by increasing the Φ.

In this paper, two crystal growth-rate models were adopted to determine the growth rate for the present Ge_7Sb_{93} alloy. These models will be called CG and MYEGA in this article, respectively. Using these models we thus explicitly assume that crystallization occurs in a supercooled liquid. This is expected, but *Salinga et al.*[16] indicated that amorphous PCMs are actually in a glass state and that for crystallization events at relatively low temperatures the phase transition instead might be directly from amorphous to crystalline (without entering the supercooled liquid) phase.

From our previous work we established that the nucleation of Ge_xSb_{1-x} occurs after a certain incubation time and after that only growth of crystal is significant, i.e. we have pre-existing nuclei (site saturation); see Figure 3.7 of the Appendix. Therefore, the main process we are looking at here is the growth of crystals. The number of nuclei per unit (untransformed) volume was therefore assumed to be a constant (N), neither time nor temperature dependent. The same assumption was made in the work of *Orava et al.*.[17,25] However, in their analysis for $Ge_2Sb_2Te_5$ it was not independently checked whether this assumption is justified. Here, we clearly have this justification; see Appendix.

3.3 Results and discussion

3.3.1 DSC traces obtained from experiments and numerical simulations

Figure 3.1a displays direct traces of ultrafast DSC measurements performed on Ge_7Sb_{93} powdered films for heating rates ranging from 50 to 40 000 K s^{-1}. It shows that the crystallization peak temperature (T_p) shifts to higher temperatures for higher Φ, i.e. from 450 K at 50 K s^{-1} to 504 K at 40 000 K s^{-1}. Figure 3.1b shows the numerically simulated DSC traces for the corresponding Φ after

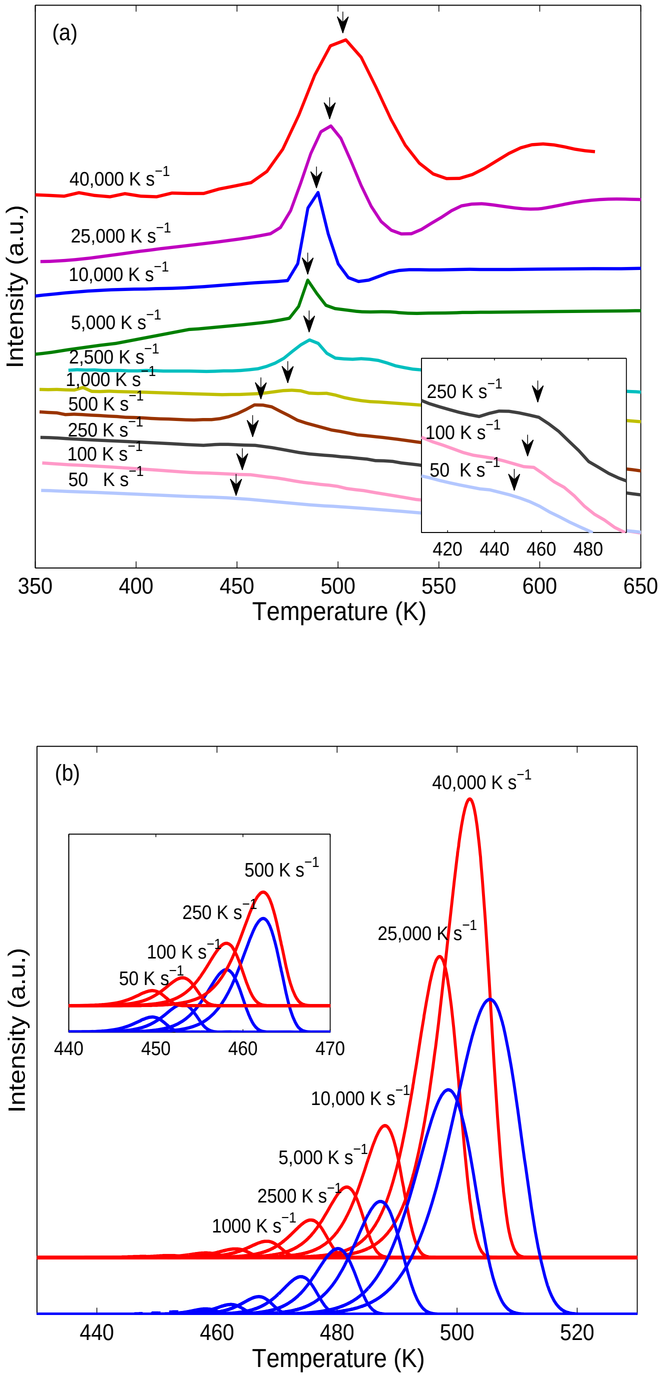

Figure 3.1 Ultrafast DSC traces obtained experimentally and by numerical simulation. The crystallization peak temperatures shift to higher temperature when the heating rate Φ is increased. (a) experimental DSC traces at different Φ, ranging from 50 K s^{-1} to 40 000 K s^{-1}. The T_p are indicated by black arrows. (The magnitude of the exothermic peaks increase with increasing Φ.) (b) Numerically calculated DSC traces by MYEGA (red lines) and CG (blue lines) models for all the Φ used experimentally. Inset shows the zoomed in exothermic peak of the lower Φ. Good match of T_p between the measured data and the calculated data can be observed for both models. Insets show the close-up of the DSC peaks for lower Φ.

fitting data in the Kissinger plot with the MYEGA and CG models. More details about this fitting are provided in the next section. The red curves in Figure 3.1(b) are calculated using the MYEGA model, while the blue curves are from the CG model. In both models T_p shows good agreement with the measured data in Figure 3.1a, with a negligible difference in T_p at higher Φ. For instance, the T_p at 40 000 K s^{-1} is 502.2 K for the MYEGA model and 504.4 K for the CG model. It is worth noting that the (areas under the) exothermic peaks increase significantly with increasing Φ, because the DSC signal is proportional to the Φ.[27] Similar as in the ultrafast DSC traces described in the work of *Orava et al.*,[17] also here the traces do not show any signature of a glass transition (separated from the crystallization peak). This is not generally the case, because in our earlier work on SeTe alloys the glass transition and crystallization were separated well in the ultrafast DSC traces.[28] However, this work also showed that the difference between T_g and T_p decreases and vanishes when the glass forming ability of the alloy becomes poorer and disappears. PCMs of interest for high switching speed applications, like $Ge_2Sb_2Te_5$ and Ge_7Sb_{93}, have to be poor glass formers and therefore in general will not have clearly separated T_g and T_p.

3.3.2 Kissinger plot and fitting of data

According to theory from Kissinger,[29] the activation energy for crystallization (Q) is proportional to the gradient of $\ln(\Phi/T_p^2)$ versus $1/T_p$, as described by Equation 3.1:

$$\frac{Q}{R} = -\frac{d(\ln(\Phi/T_p^2))}{d(1/T_p)} \tag{3.1}$$

with Q the activation energy for crystallization, Φ heating rate, *R* the gas constant and T_p the peak temperature in the DSC trace. It is straightforward to derive the activation energy for crystallization if we plot $\ln(\Phi/T_p^2)$ versus $1/T_p$ according to Equation 3.1. In traditional DSC measurements, due to the relatively low and narrowly confined Φ, typically a constant activation energy Q is found. As a result, strict Arrhenius behavior with a linear Kissinger plot in crystallization is generally observed.[3,10] In contrast, the Kissinger plot as based on the ultrafast DSC measurements performed here is slightly curved, as shown in Figure 3.2. Note that the data in Figure 3.2 is weighted to be the most representative data in our measurements. As described in the methods section, the T_p remarkably vary in the ultrafast DSC measurements, especially at high Φ. Therefore, the 2-3 data points with lowest T_p values for a certain Φ were given to the most weight to be presented in Figure 3.2, since they correspond to the best thermal contact between the chip sensor and the

Ge_7Sb_{93} flakes. The red solid circles in Figure 3.2 are the experimental data for Φ from 50 K s^{-1} to 40 000 K s^{-1}. Numerical simulations were performed to analyze this curved behavior of the data in the Kissinger plot and subsequently understand the crystallization kinetics of the Ge_7Sb_{93} alloy.

JMAK theory is used to perform numerical simulations to obtain DSC traces along with modeled Kissinger plots. To perform these simulations, the temperature dependence of the crystal growth rate *U(T)* is essential. In this paper, two different models for *U(T)* have been used.

The first one is based on work of *Salinga et al.* (and *Mauro et al.*), in which the growth rate can be written as:[16]

$$U(T) = \frac{4r_{atom}k_BT}{3\pi\lambda^2 R_{hyd}\eta(T)}[1-\exp(-\frac{\Delta G(T)}{k_BT})] \tag{3.2}$$

with r_{atom} the atomic radius(~1.5 Å), λ the diffusional jump distance (~1 Å), R_{hyd} the hydrodynamic radius (~0.5 Å), k_B the Boltzmann constant and $\Delta G(T)$ the change of Gibbs free energy. All these above values are the same as were taken for AgInSbTe.[16] According to *Thomson* and *Spaepen*,[30] $\Delta G(T)$ in Equation 3.2 can be estimated from the latent heat of melting (ΔH_m), approximately 0.22 eV at^{-1},[31] and the melting temperature T_m:

$$\Delta G(T) = \frac{\Delta H_m(T_m - T)}{T_m}(\frac{2T}{T_m + T}) \tag{3.3}$$

Where T_m is taken from Ge-Sb phase diagram as 887 K.[32]

Finally, an accurate description of the viscosity $\eta(T)$ is required in Equation 3.2. According to *Mauro et al.*[33] $\eta(T)$ can be modeled for glass-forming liquids as follows:

$$\log_{10}\eta(T) = \log_{10}\eta_\infty + (12-\log_{10}\eta_\infty)\frac{T_g}{T}\exp[(\frac{m}{12-\log_{10}\eta_\infty}-1)(\frac{T_g}{T}-1)] \tag{3.4}$$

with η_∞ the viscosity at infinite temperature, which is estimated here as: $\log_{10}\eta_\infty = -3$ and m the fragility. The main idea of fitting the experimental data in the Kissinger plot (Figure 3.2) is to adjust the parameters, i.e., T_g , m , and the number density of nuclei *N* (per unit of untransformed space). The best fit (smallest χ^2 value leading to R^2 of 0.924) is shown as the red curve in Figure 3.2, with T_g =379 K, m =65, with a proper value of *N* (for more details, see Appendix). These values are plausible and consistent, because in a previous study the T_g of Ge_9Sb_{91} and Ge_8Sb_{92} were obtained by an independent method as 395 K and 382 K, respectively.[15] According to *Kalb et al.*[34] T_g is found to be related to the crystallization (peak) temperature T_p in PCMs, ~10 K below T_p when a constant Φ of 40 K min^{-1} was applied to GST and AIST. Therefore, consistent with our finding it is expected that the T_g of Ge_7Sb_{93} is slightly lower than the ones of Ge_9Sb_{91} and Ge_8Sb_{92}, since the T_p of Ge_xSb_{1-x} alloys decreases with the decrement of x.[9] The m of this alloy is 65, which is also close to the ones of Ge_9Sb_{91} and Ge_8Sb_{92} (59 and 61, respectively) as found by an independent method and indicates a trend of slightly increasing m with decreasing Ge concentration.

The other model we used for the growth rate is the same as adopted by *Orava et al.* and it is based on the expression by *Cohen* and *Grest* for the viscosity of glass-forming liquids. *Orava et al.* used this model also for fitting data of $Ge_2Sb_2Te_5$ powdered films in a Kissinger plot and thereby describing the viscosity and growth rate.[17] According to the CG model the kinetic coefficient for crystal growth U_{kin} can be written as:[17]

$$\log_{10} U_{kin} = A - \frac{2B}{T - T_0 + [(T - T_0)^2 + 4CT]^{1/2}} \tag{3.5}$$

with A, B, C, T_0 input parameters. Then the real growth rate $U(T)$ as a function of temperature is:[17]

$$U(T) = U_{kin}[1 - \exp(-\frac{\Delta G(T)}{RT})] \tag{3.6}$$

with R the gas constant and $\Delta G(T)$ the driving force for crystallization, which in this case is also described by Equation 3.3.

Using the same fitting procedure as for the MYEGA model, the modeled Kissinger plot (the blue curve in Figure 3.2) for the CG model matches well with the experimental data. The best fit we can obtain here offers B =119.2， C =1.5, T_0 =443 K, with R^2 of 0.937. T_0 is supposed to be 10% to 17% higher than the measured T_g ,[18] which is 379 K from fitting by the MYEGA model and indeed T_0 is 17% higher than that in this fitting. The parameter A in this model (see Equation 3.5) is not relevant for fitting the data in the Kissinger plot, but it is crucial to determine the absolute values of the viscosity and growth rate as function of temperature as will be discussed in the next two sections of this chapter.

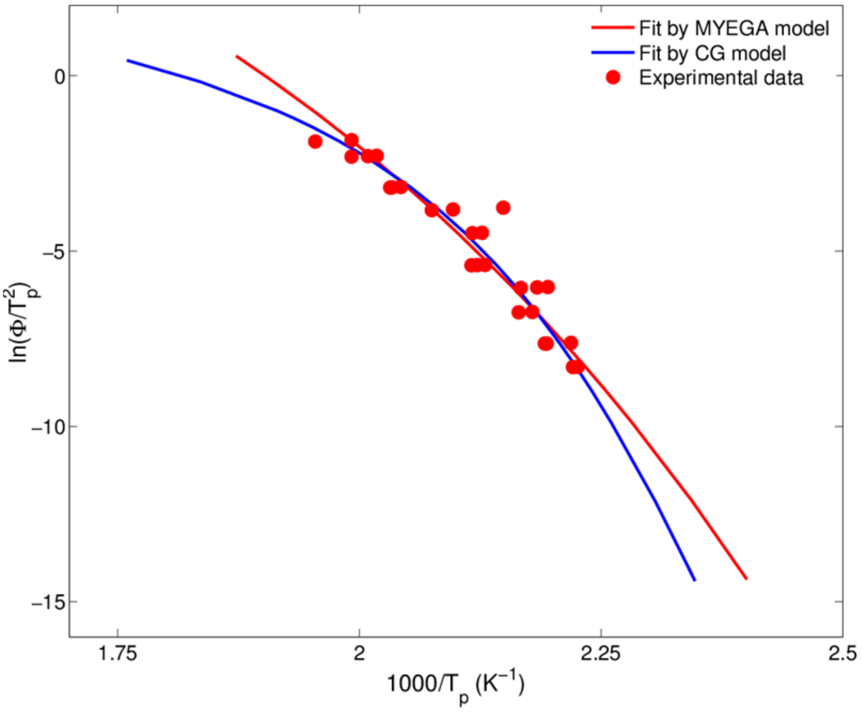

Figure 3.2 Kissinger plot with fittings for the MYEGA and the CG models. The red circles are the most weighted experimental data obtained by ultrafast DSC at Φ from 50 to 40 000 K s^{-1}. The red curve is the modeled Kissinger plot using the MYEGA model for growth rate. The fit quality can be valued by adjusted R^2, 0.924 here. The blue curve is the modeled Kissinger plot using the CG model, with R^2 of 0.937. Taking the scatter in the data into account, these 2 fittings can be considered as good fits. Slight curvature can be seen in Kissinger plot of experimental data as well as the ones of these 2 models. However, the difference in curvature between these 2 models is obvious, as the CG model gives much stronger curvature than the MYEGA model.

3.3.3 Viscosity and fragility

Figure 3.3 shows the viscosity of the Ge_7Sb_{93} flaked films as based on fitting the two models to the data in the Kissinger plot (shown in Figure 3.2). As described by Equation 3.4, the viscosity can be easily obtained once the T_g and m values have been derived from fitting the MYEGA model. Employing these two values obtained in the previous section, the temperature dependence of viscosity is shown as the red line in Figure 3.3, with a m of 65. The region marked in thick red (0.75~0.85 T_g/T) in these lines represents the temperature region that was analyzed using ultrafast DSC measurements of this alloy.

To obtain η and m in the CG model, the kinetic coefficient U_{kin} (Equation 3.5) has to be transposed. By assuming $\eta \propto U_{kin}^{-1}$ and setting $\eta(T_m)$ to 1.2 × 10^{-3} Pa s with T_m the melting temperature, the viscosity is obtained shown as the blue, dashed curve. The latter requirement is actually used to determine the (still unknown) value of A in Equation 3.5. Note that this model does not provide a value for T_g , so, it is assumed to be 379 K here, as we obtained from the MYEGA model. As can be seen in Figure 3.3, the viscosity at T_g slightly deviates from 10^{12} Pa s, which is a widely accepted value directly associated with T_g for glass forming liquids. This can be a result of the decoupling of $\eta \propto U_{kin}^{-1}$. So we take the decoupled equation $U_{kin} \propto \eta^{-\zeta}$ to derive the viscosity, combined with setting $\eta(T_g)$ to 10^{12} Pa s. The fitted ζ here is 0.97. The blue solid line is the η

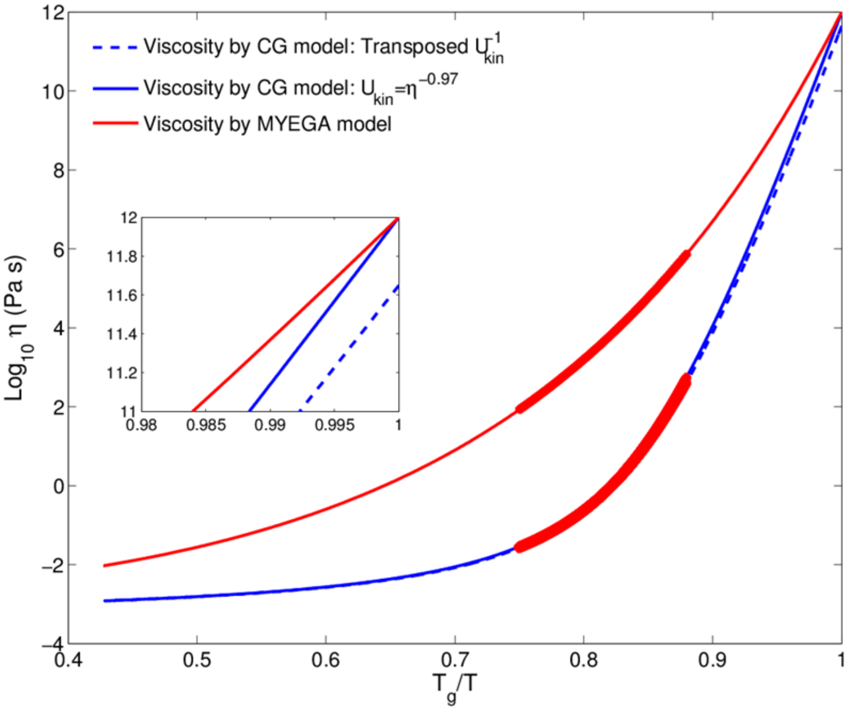

Figure 3.3 Angell plots for temperature dependence of viscosity from MYEGA and CG models. The red line is derived from the MYEGA model, in which the viscosities at T_g and T_∞ are fixed to 10^{12} and 10^{-3} Pa s, respectively. The fragility m is fitted to be 65 for this model, close to the values obtained for Ge_8Sb_{92} and Ge_9Sb_{91} alloys in reference.[15] The blue dashed lines are the viscosity obtained for the CG model by transposing $U_{kin}(\eta \propto U_{kin}^{-1})$ and by using the additional boundary condition $\eta(T_m)=1.2\times10^{-3}$ Pa. Note that in this way the viscosity at T_g is slightly different from 10^{12} Pa s. Then, the $\eta(T_g)$ is set to 10^{12} Pa s by using $U_{kin}=\eta^{-\zeta}$, with ζ=0.97 here, as shown as the blue, solid line. The m is derived to be 86 for this CG model. As can be nicely seen in this figure, the CG model gives steeper curve at T_g , leading to higher m. The thicker red regions on both curves indicate the temperature region in which the peaks temperatures in the ultrafast DSC have been obtained. Inset is the close-up of the area close to T_g .

after the decoupling is taken into account. The *m*, defined as $m = \left. \frac{d(\log_{10} \eta(T))}{d(T_g / T)} \right|_{T=T_g}$, in this case of the CG model applied to this alloy leads to a value of 86 which is thus substantially larger than the *m* obtained by the MYEGA model.

3.3.4. Growth rate

The main purpose of performing ultrafast DSC here is to obtain the overall temperature dependence of growth rate and by doing so also the maximum growth rate of the alloy can be extrapolated. The red curve in Figure 3.4 shows for the MYEGA model the growth rate as function of temperature transposed from the viscosity using Equation 3.2. The non-Arrhenius temperature dependence of the growth rate can be readily observed. In the measured temperature region from ultrafast DSC, i.e. from ~0.5 to ~0.57 T_m (450 K to 505 K, marked in red in Figure 3.4), the derived growth rate matches well with independent data of Ge_7Sb_{93} (the blue squares in Figure 3.4), where crystal growth was measured directly by employing a high-speed optical camera and by accelerating the growth using a laser.[15] The maximum growth rate is readily extrapolated as 21 m s^{-1} at 800 K (~0.90 T_m) from this plot, which is slightly higher than that of Ge_8Sb_{92}, ~15 m s^{-1} previously reported in Ref. 15. *Adelerhof* [35] reported experimental data for the maximum growth rate of $Ge_{10}Sb_{90}$ as 50 m s^{-1} and that for Ge_7Sb_{93} should be higher than 60 m s^{-1} by extrapolating the trend in this paper showing that the growth rate increases with decreasing Ge concentration. However, the materials they studied were melt-quenched alloys, which usually exhibit a higher growth rate than the as-deposited materials we study here. For example, the growth rates of melt-quenched AgInSbTe PCMs are measured 2-3 orders of magnitude higher than the ones of as-deposited AgInSbTe.[16] The maximum growth rate obtained here can therefore readily shift to a value higher than 50 m s^{-1} once the materials become melt-quenched.

It is worth noting that the Stokes-Einstein relation is intrinsically included in Equation 3.2 in the MYEGA model. The growth rate *U* directly relates to the diffusivity *D*, while in Stokes-Einstein equation *D* couples to viscosity η by $D(T) \propto k_B T / \eta(T)$. However, it is well accepted that the Stokes-Einstein equation decouples below ~1.2 T_g,[14,36] i.e. 454 K for this alloy. In Figure 3.4, the modeled growth rate from the MYEGA model matches excellently with the independent data beyond 450 K, while below that some discrepancy arises. This discrepancy can therefore probably stem from the decoupling. With the decoupling considered, we take $U \propto \eta^{-\zeta}$ with ζ =0.9 to calculate the growth rate from 379 K (T_g) to 450 K (~1.2 T_g). The green line in Figure 3.4 shows the decoupled, modeled growth rate, with a clearly better match to the independent data. The excellent match between our fitting data and the independent data from Ref. 15 demonstrates that the method (with MYEGA model) adopted here to analyze the ultrafast DSC data appears reliable. This suggests a proper method to study the ultrafast DSC measurements and an appropriate model to study the crystallization kinetics of this alloy at relatively high temperatures not reachable with conventional measurement techniques.

Meanwhile, the CG model is also used to evaluate the temperature dependence of growth rate for this alloy. Again, consistently with the previous section, an extra relation is required to determine the value of the parameter *A* in Equation 3.5 in order to obtain the absolute value of the growth rate. Similar to Ref. 17, the effective diffusion coefficient *D* can be derived by Stokes-Einstein equation from viscosity η:

$$D = \frac{k_B T}{3\pi a \eta} \tag{3.7}$$

with a the effective jump distance. Instead of 0.3 nm as in Ref. 17, here we take a = 0.15 nm. For growth dominated by diffusion, the U_{kin} at T_m is given by $U_{kin}(T_m) = D(T_m)/a$. So $U_{kin}(T_m)$ is 54 m s^{-1}, close to the maximum crystallization velocity measured by *Adelerhof* [35] and four times the one of GST (13.5 m s^{-1}).[17] An important factor is that the GeSb alloy is a growth-dominated PCM, whereas GST (such as $Ge_2Sb_2Te_5$) is a nucleation-dominant PCM. Moreover, it is known that the highest crystal growth rates in PCMs have been observed for Sb-rich alloys. Therefore the substantial higher $U_{kin}(T_m)$ derived for the current Ge_7Sb_{93} than for GST is according to expectations. The blue curve in Figure 3.4 is the obtained growth rate via the CG model. The maximum growth rate *U* through extrapolation here is 17 m s^{-1} at 695 K (~0.78 T_m). The values of maximum growth rate obtained from both the MYEGA and CG models are very close, which can also shows the rationality of setting the $U_{kin}(T_m)$ value in the CG model to 54 m s^{-1}.

Nevertheless, as can be clearly observed in Figure 3.4, the growth rate at the measuring temperature range derived from the CG model is unexpectedly 2-3 orders of magnitude higher than the independent data, implying a strong overestimation of the growth rate in this CG model to describe the growth rate under ultrafast DSC in Ge_7Sb_{93} alloy. A possible reason for this large discrepancy could be the parameter *A* in Equation 3.5, which directly affects the real growth rate (and viscosity) of this alloy. So we tried instead to vary the *A* value to obtain a better match to the independent growth rate data. A better match can be found, still not as good as the MYEGA model, however an unacceptable low maximum growth rate of 0.17 m s^{-1} is then obtained (see Appendix). These present findings thus seriously question the validity of the CG model, at least for the present alloy. Moreover the CG model already requires, even excluding the parameter *A*, three fitting parameters to describe the viscosity, whereas the *Mauro* description only requires two fitting parameters (T_g and m). A final disadvantage of the CG model is that it offers no direct information about the T_g of the alloy. One has to assume a value of T_g when calculating viscosity because T_g is not observed in the ultrafast DSC traces.

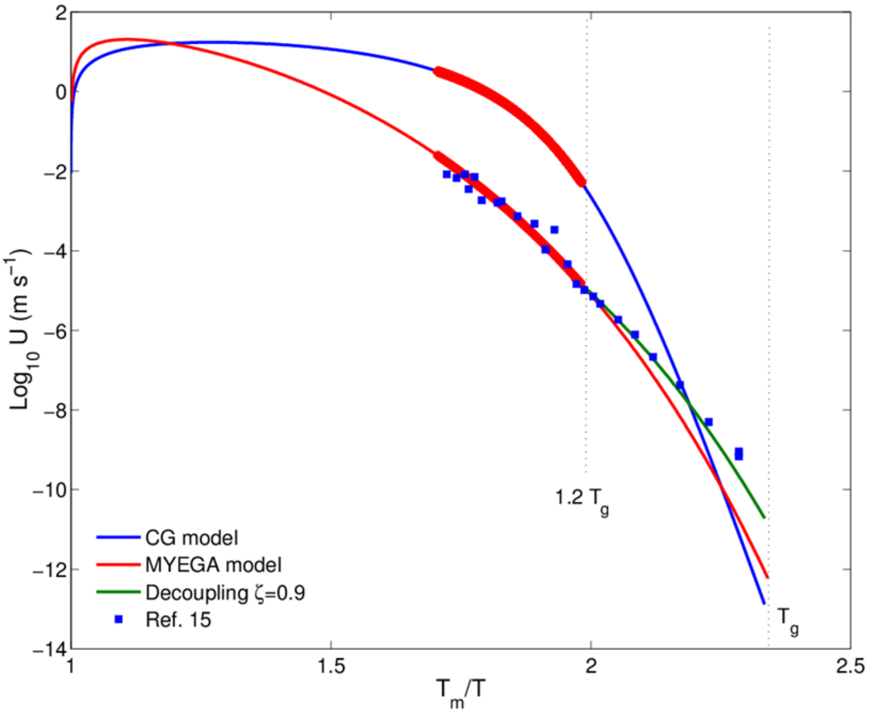

Figure 3.4 Overall temperature dependence of growth rate derived from the MYEGA and CG models. The red curve shows the growth rate of the Ge_7Sb_{93} alloy from T_g to T_m given by Equation 3.2 of the MYEGA model. Blue squares are the growth rate of this alloy, measured by a high speed optical camera and laser acceleration.[15] The green curve shows the growth rate below 1.2 T_g from the MYEGA model, with a decoupling between viscosity and growth rate adopted (ζ=0.9 in $U \propto \eta^{-\zeta}$). The blue curve displays the overall growth rate as function of temperature obtained from the CG model, which results in a 2-3 orders of magnitude overestimation of the growth rate observed in the temperature region of ultrafast DSC. The maximum growth rates given by the MYEGA and CG models are 21 m s^{-1} and 17 m s^{-1}, respectively. The thicker red regions on both curves indicate the temperature region in which the peaks temperatures in the ultrafast DSC have been obtained.

In a perspective of *Wuttig et al.*,[24] it is clearly noticeable in the figure provided that the growth rate derived from the CG model is, for the temperature range of conventional measurements, 3-4 orders of magnitude larger than the independent measured data provided in this figure. Moreover, this model also leads to a substantially larger activation energy for $Ge_2Sb_2Te_5$ within the temperature region where data have been obtained by conventional measurements. For $Ge_2Sb_2Te_5$ thin films it is well-established that the activation energy for crystallization and growth near T_g is in the range 2.2 – 3.0 eV.[7,10,37–42] However, the CG model leads to an unphysically high value beyond 5 eV near T_g (~2.35 T_m/T). These two mismatches thus further strengthen and generalize our conclusion that the CG model seems inappropriate to describe the viscosity and kinetics of PCMs.

3.4 Conclusions

Ultrafast DSC has been employed to study the crystallization kinetics of a growth-dominant phase change material, Ge_7Sb_{93}. Models for growth rate (of phase-change materials) and viscosity (of supercooled liquids) from *Salinga et al.* and *Mauro et al.* were used to analyze the ultrafast DSC data. Fitting these models to the data provides a glass transition temperature of 379 K and a fragility of 65 for this alloy. The overall temperature dependences of the viscosity and growth rate from glass transition to melting temperatures are revealed as well, from which a maximum growth rate of 21 m s^{-1} at ~800 K is extrapolated for supercooled Ge_7Sb_{93} alloy. Next to this model of *Salinga* and *Mauro* (MYEGA) the ultrafast DSC data was also fitted based on the model used by *Orava et al.,* which employs an equation by *Cohen* and *Grest* (CG) to describe the viscosity of glass-forming liquids. In order to test the validity of both models, independent data, in which the growth rate was directly measured as a function of temperature, was used. This test showed that the MYEGA model agrees very well with the data, but the CG model results in orders of magnitude discrepancies. Our analysis shows that the CG model seems inappropriate to describe the viscosity and kinetics of PCMs. This also shows that one has to be careful when deriving crystal growth rates or viscosities on the basis of ultrafast DSC measurements and that some comparison with directly measured growth rates or viscosities is generally required.

Appendix

Thermal lag of the ultrafast DSC

Because of the open structure of the chip sensor where the sample is heated only single sided, it is necessary to estimate the thermal lag of the ultrafast DSC, the most significant source of which includes two parts: 1) delayed heat transfer at the interface between the aluminum stage and sample due to low heat transfer coefficient (*h*) and 2) temperature gradients inside the sample.

The second factor can be assessed by the dimensionless Biot number:[43]

$$B = \frac{hL}{\kappa} \tag{3.8}$$

where h is the heat transfer coefficient, L the sample thickness and κ the thermal conductivity of the sample materials. The temperature gradient within a sample is negligible if $B << 1$, giving a uniform thermal distribution in the sample. Typical metal casting experiments gives the value of h in the range between 5 and 20 kW m^{-2} K^{-1}.[44] The thickness of the sample we investigate is 200 nm. For amorphous PCMs, κ could be very low (0.17 W m^{-1} K^{-1} for $Ge_{15}Sb_{85}$ at 20 ^{o}C [45]). Taking these values we then obtain a Biot number in the range from 0.005 to 0.05, inferring that the assumption of a uniform temperature distribution within the sample is reasonable. Therefore the dominate concern is the thermal lag due to the thermal transfer at the interface between the chip sensor and the sample.

The thermal lag caused by the heat transfer between the chip sensor and the sample can be estimated by:

$$\Delta T = \frac{C_p L}{h} \Phi \tag{3.9}$$

with C_p the heat capacity per unit volume, L the thickness and Φ the heating rate. We take the value of Sb (no data found for GeSb) thin film: $C_p = 1.39 \times 10^6$ J m^{-3} K^{-1}.[46] With the value for h and L, the ΔT is then in the range 0.5 to 6 K at the maximum heating rate 40 000 K s^{-1}. This thermal lag will not affect the breakdown of the Arrhenius behavior, which starts at 10 000 K s^{-1}, at which the thermal lag is still very small. The main concern of our method is the thermal contact between the sample and the chip sensor, which can vary for different samples as the melt-quench method, which ensures good conformal contact between sample and sensor surface, cannot be applied to our measurements for the phase-change materials.

To confirm a good thermal contact of the non-melt-quenched sample, we also tested the onset temperature (T_{on}) of melting endotherm of scraped-off indium pieces. A thin indium layer with a thickness of 30 nm was deposited on pre-cleaned glass. Then this layer was scraped off and formed small pieces (hardly no flat flakes due to the excellent ductility of indium). Then the small pieces of indium with the sizes of roughly 20×20 μm^2 were then transferred on the chip sensor of ultrafast DSC, following with ultrafast heating at high heating rates. Also here we repeated this measurements for several times at each heating rate and selected the lowest peak temperature values for the best thermal contact as we also do in our measurements of the phase-change materials (PCMs). The temperature at the onset of melting, T_{on}, we measured in this way is 160 °C at a heating rate of 20 000 K s^{-1}, which is similar to the data obtained for melt-quench indium flakes, as depicted in Figure 3.5, indicating that the thermal contact of non-melt-quenched samples do not significantly degrade. Therefore the data we obtained for PCMs (using a non-melt-quenching method) are reliable.

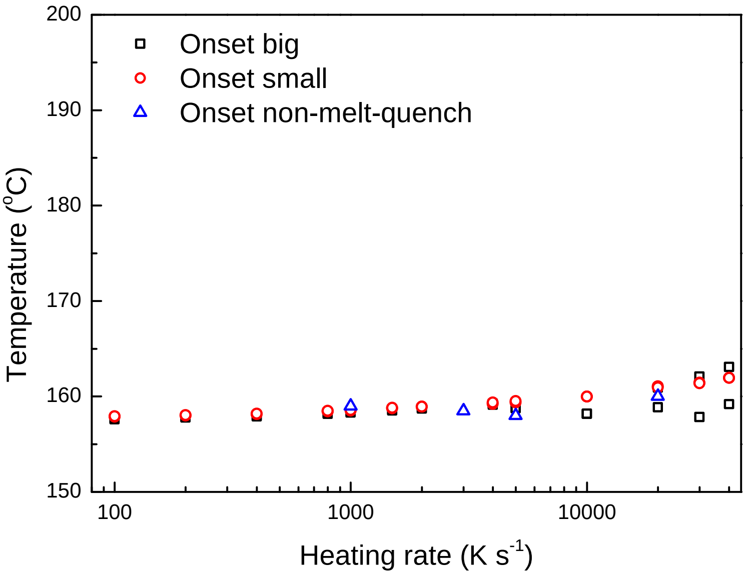

Figure 3.5 Onset temperature of melting endotherm for indium samples prepared by different methods, indicating the good reliability of the method used in this work.

To minimize the possible influence of bad thermal contact between the specimen and the chip sensor, we also repeated measurements many times at each heating rates, especially at high heat rates (above 10 000 K s^{-1}) and then selected the lowest several (3 to 5) peak temperature as the most representative data for fitting.

Optimization process in Kissinger plot

As shown by *Kelton*,[27] the DSC signal is directly proportional to the rate by which the fraction transformed $X(T_i)$ changes. By changing the input parameters in these two growth-rate models also the T_p at a certain heating rate (Φ) can be varied. By adjusting all the parameters, a modeled Kissinger curve can be fitted to experimental data in the Kissinger plot. The fitting procedure used here is the downhill Simplex method due to *Nelder* and *Mead*.[47] In a Kissinger plot the *x* data is equivalent to the $1000/T_p$, where the *y* data correspond to $\ln(\Phi/T_p^2)$. The χ^2 in the fitting procedure was defined as the difference between the experimentally measured data x (x_i) and the modeled data x (x_{mod}) in the Kissinger plot: $\chi^2 = \sum_{i=1}^{k}(x_i - x_{\text{mod}})^2$, because in the Kissinger plot the *y* data hardly changes at a certain Φ for different T_p. In the Simplex method starting estimations for the fitting parameters have to be provided. It turned out essential to have a reasonable starting value for the number density of nuclei.

Estimation of number density of nuclei *N*

During fitting the data in the Kissinger plot by means of the growth models and JMAK theory, we find that the nucleation density *N* impacts the final fitting results. For instance, the fitting fragility *m* is shifted from 65 to 95 in the MYEGA model if the *N* is exaggeratedly lowered from 10^{16} m^{-3} to 10^{10} m^{-3}. Interestingly, this change in *N* does not affect the value of the glass transition temperature T_g obtained by fitting the data in the Kissinger plot. Figure 3.6 shows in an Angell plot the result of this fitting with these two fixed values of *N*.

Because of the importance to have a reasonable estimate for *N*, it is required to have a reasonable approximation of the nuclei numbers during heating in the ultrafast DSC. The strength of our current approach is that we have this estimate based on our earlier work employing a high speed optical camera to monitor the nucleation and growth of crystals in the 200 nm thick Ge_7Sb_{93} films.[15] The phase transition of these films was investigated via isochronal heating on a ceramic heater at a Φ of 10 °C min^{-1}. Observable nuclei develop at about 130 °C. Figure 3.7 a-b show the change of nuclei with temperature, increasing for the area observed from 123 at 133.3 °C to 147 at 142.3 °C. The number of nuclei thus only increases by ~20%. An approximated value for *N* is achieved as ~4.1×10^{14} m^{-3} at 142 °C when a 3-dimensional growth model is adopted for the crystals and considering the thickness of this film (200 nm). From the video made from this measurement, it is clear that the number of nuclei hardly increase after 140 °C for this Φ. After the initial nucleation below 135 °C, the dominant process of crystallization is thus growth of crystals. Moreover, in all our measurements of crystallization of Ge_7Sb_{93} films we observed that all crystals observed in a certain area tend to have the same size. These observations thus show that the constant nuclei assumption in the numerical calculations via JMAK theory is justified.

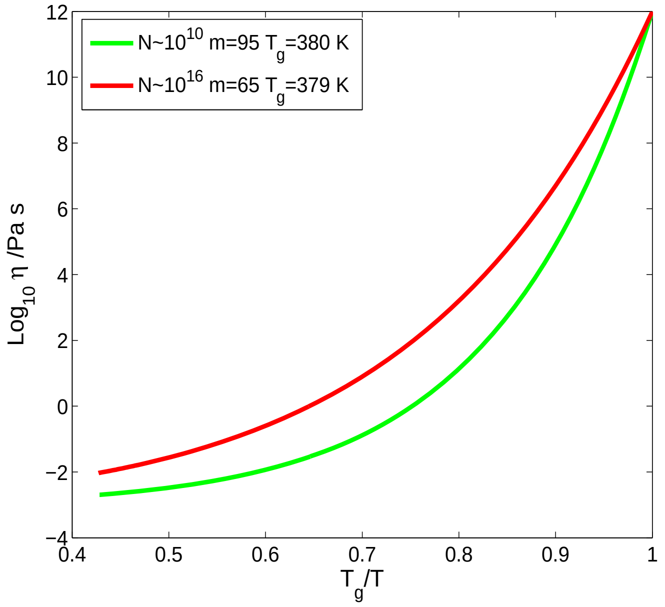

Figure 3.6 Angell plot with different number density of nuclei N. This figure displays the viscosity as function of temperature for two *N* values, i.e. 10^{10} m^{-3} to 10^{16} m^{-3} in order to demonstrate the importance to have a reasonable estimate for *N*. While the fitted T_g scarcely changed (~380 K), the m changes remarkably from 95 to 65.

However, in another measurement, it is found that scraping off the Ge_7Sb_{93} films remarkably enlarges the possibility of nucleation as shown in Figure 3.7c, where areas which have been scratched (and which probably experienced compressive stress) experience earlier nucleation than the surrounding PCM under isothermal heating, resulting in a greater value for *N*. Accelerated crystallization by applying modest compressive stresses to Ge_6Sb_{94} or Ge_7Sb_{93} films has also been demonstrated by our previous work.[48] Stress-induced crystallization of $Ge_{15}Sb_{85}$ has also been discussed by *Shakhvorostov et al.*.[49] Therefore, the real *N* in the ultrafast DSC measurements must be larger than 10^{14} m^{-3}. On the other hand, with an *N* value larger than 10^{17} m^{-3} the data in the Kissinger plot could not be fitted. So, the reasonable region of *N* values is 10^{15} to 10^{16} m^{-3} in our fitting, and the one we used is 10^{16} m^{-3}. Note this is the starting value employed in the fitting procedure using the downhill Simplex method and therefore still some minor adjustment of number density of nuclei *N* is possible as a result of the fitting procedure. For this fitting a value of 5×10^{16} m^{-3} is derived for *N*.

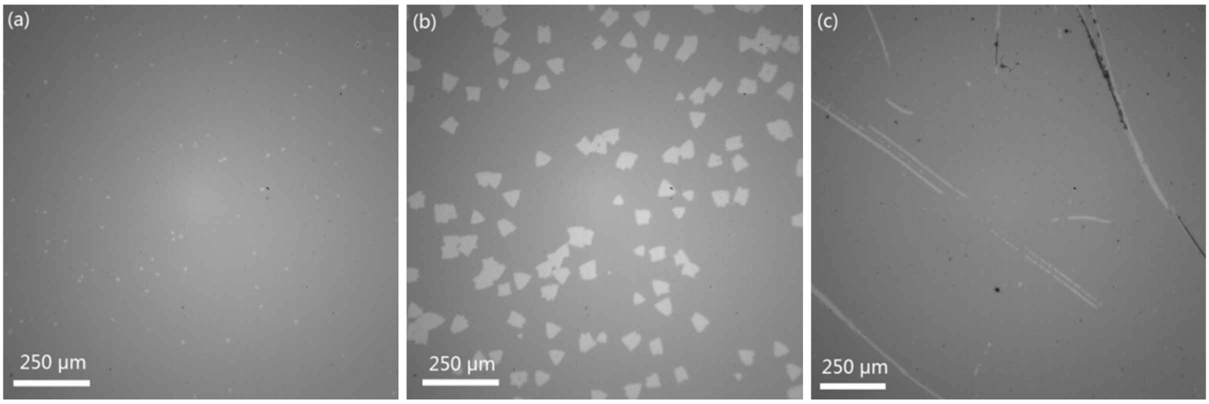

Figure 3.7 Ge_7Sb_{93} films under isochronal heating. (a) shows the nuclei number of 123 at 133.3 °C; (b) shows the number of nuclei changes to 147 at 142.3 °C. From (a) and (b) the density of nuclei can be derived for both 2-dimensional (8.2×10^{7} m^{-2}) and 3-dimensional (4.1×10^{14} m^{-3}) crystal growth for JMAK theory at 142 °C, as the thickness of the film is 200 nm. (c) shows the pressure-induced nucleation on Ge_7Sb_{93} films. (c) The scratches made by a hair nucleate earlier than the surrounding materials under isothermal heating at 125°C , with an obviously higher nuclei density.

Effect of the *A* parameter in the *Cohen* & *Grest* expression for determining the growth rate

In Figure 3.8, the influence of the value of *A* in the CG model (see Equation 3.5) on the growth rate is shown. The blue curve shows the growth rate derived from the Stokes-Einstein equation, identical to the one in Figure 3.4, leading to a maximum growth rate (U_m) of 17 m s^{-1}. The green curve in this figure is derived when *A* is set to the 0, which is the value employed in the fitting of the Kissinger plot (Figure 3.2). A U_m of 0.17 m s^{-1} is obtained here. Then, the value of *A* is adapted in order to match the independent data from Ref. 15. Then *A* becomes -0.4 and the corresponding growth rate curve is the khaki one in Figure 3.8. It is nicely shown that this modeled growth rate matches well with the independent data in the limited measurement region of the ultrafast DSC which is between 450 and 505 K, but still leads to a poor fit for temperatures below 450 K. Moreover, this *A* value results in a unacceptable low value of U_m (0.07 m s^{-1}). From the original equation and from the graph it is obvious that the effect of *A* in the C&G model is that it only changes the absolute value of the of the growth rate and thus only results in a vertical shift of the curves in Figure 3.8. The present results thus strongly suggest that this C&G model is not suitable to describe the growth rate of PCMs, at least for the growth dominated GeSb alloy. However, quite similar discrepancies between modelled and experimental results are observable for the nucleation dominated $Ge_2Sb_2Te_5$ alloy in Figure 1 of Ref. 24. Therefore, indeed, it appears justified to question the appropriateness of the CG model for PCMs in general.

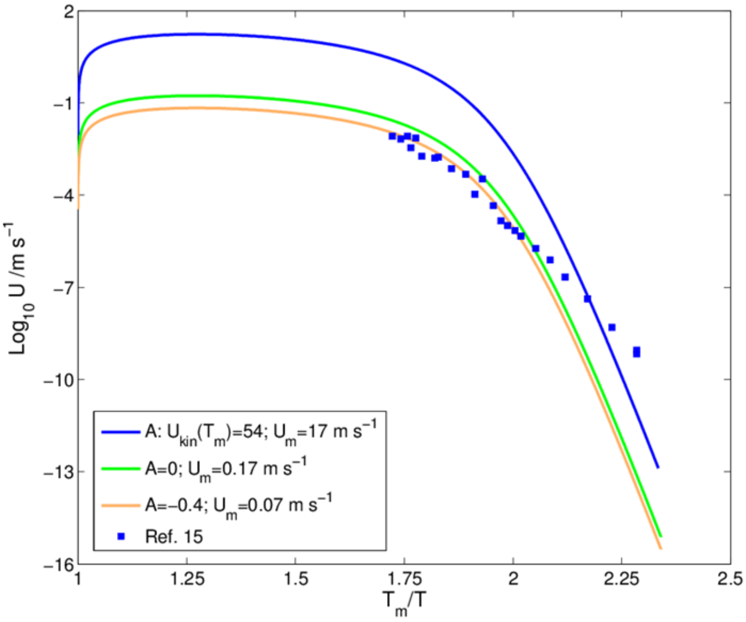

Figure 3.8 Growth rate from the CG model for different values of parameter *A*. The green curve is identical to the one shown in the Figure 3.4 in the main text, which leads to a maximum growth rate value (U_m) of 17 m s^{-1}. The khaki curve relates to the value *A*=0, which is the one used for fitting in the Kissinger plot. A U_m of 0.17 m s^{-1} is obtained. Then the value of *A* is set to make the modeled growth rate match to the independent data. *A*=-0.4, the green curve is obtained as the growth rate. Although good match to the data can be seen, an unacceptable value of U_m (0.07 m s^{-1}) is derived here.

References

(1) Raoux, S.; Welnic, W.; Ielmini, D. *Chem. Rev.* **2010**, *110* (1), 240–267.

(2) Wuttig, M.; Yamada, N. *Nat. Mater.* **2007**, *6* (11), 824–832.

(3) Park, J.; Kim, M. R.; Choi, W. S.; Seo, H.; Yeon, C. *Jpn. J. Appl. Phys.* **1999**, *38* (8R), 4775.

(4) Coombs, J. H.; Jongenelis, A. P. J. M.; Es-Spiekman, W. van; Jacobs, B. a. J. *J. Appl. Phys.* **1995**, *78* (8), 4906–4917.

(5) Kooi, B. J.; Hosson, J. T. M. D. *J. Appl. Phys.* **2004**, *95* (9), 4714–4721.

(6) Rocca, J.; Erazú, M.; Fontana, M.; Arcondo, B. *J. Non-Cryst. Solids* **2009**, *355* (37–42), 2068–2073.

(7) Kalb, J.; Spaepen, F.; Wuttig, M. *Appl. Phys. Lett.* **2004**, *84* (25), 5240–5242.

(8) Kooi, B. J.; Groot, W. M. G.; Hosson, J. T. M. D. *J. Appl. Phys.* **2004**, *95* (3), 924–932.

(9) Raoux, S.; Jr, C. C.; Krusin-Elbaum, L.; Jordan-Sweet, J. L.; Virwani, K.; Hitzbleck, M.; Salinga, M.; Madan, A.; Pinto, T. L. *J. Appl. Phys.* **2009**, *105* (6), 064918.

(10) Friedrich, I.; Weidenhof, V.; Njoroge, W.; Franz, P.; Wuttig, M. *J. Appl. Phys.* **2000**, *87* (9), 4130–4134.

(11) Hegedüs, J.; Elliott, S. R. *Nat. Mater.* **2008**, *7* (5), 399–405.

(12) Matsunaga, T.; Akola, J.; Kohara, S.; Honma, T.; Kobayashi, K.; Ikenaga, E.; Jones, R. O.; Yamada, N.; Takata, M.; Kojima, R. *Nat. Mater.* **2011**, *10* (2), 129–134.

(13) Zhang, W.; Ronneberger, I.; Zalden, P.; Xu, M.; Salinga, M.; Wuttig, M.; Mazzarello, R. *Sci. Rep.* **2014**, *4*.

(14) Sosso, G. C.; Colombo, J.; Behler, J.; Del Gado, E.; Bernasconi, M. *J. Phys. Chem. B* **2014**, *118* (47), 13621–13628.

(15) Eising, G.; Van Damme, T.; Kooi, B. J. *Cryst. Growth Des.* **2014**, *14* (7), 3392–3397.

(16) Salinga, M.; Carria, E.; Kaldenbach, A.; Bornhöfft, M.; Benke, J.; Mayer, J.; Wuttig, M. *Nat. Commun.* **2013**, *4*.

(17) Orava, J.; Greer, A. L.; Gholipour, B.; Hewak, D. W.; Smith, C. E. *Nat. Mater.* **2012**, *11* (4), 279–283.

(18) Cohen, M. H.; Grest, G. S. *Phys. Rev. B* **1979**, *20* (3), 1077–1098.

(19) A.N. Kolmogorov. *Bull Acad Sci USSR Math Ser* **1937**, *1*, 355–359.

(20) W.A. Johnson, R.F. Mehl. *Trans Aime* **1939**, *135* (8), 396–415.

(21) Avrami, M. *J. Chem. Phys.* **1939**, *7* (12), 1103–1112.

(22) Avrami, M. *J. Chem. Phys.* **1940**, *8* (2), 212–224.

(23) Avrami, M. *J. Chem. Phys.* **1941**, *9* (2), 177–184.

(24) Wuttig, M.; Salinga, M. *Nat. Mater.* **2012**, *11* (4), 270–271.

(25) Orava, J.; Hewak, D. W.; Greer, A. L. *Adv. Funct. Mater.* **2015**, n/a-n/a.

(26) Eising, G.; Niebuur, B.-J.; Pauza, A.; Kooi, B. J. *Adv. Funct. Mater.* **2014**, *24* (12), 1687–1694.

(27) Kelton, K. F. *Mater. Sci. Eng. A* **1997**, *226–228*, 142–150.

(28) Vermeulen, P. A.; Momand, J.; Kooi, B. J. *J. Chem. Phys.* **2014**, *141* (2), 024502.

(29) Kissinger, H. E. *Anal. Chem.* **1957**, *29* (11), 1702–1706.

(30) Thompson, C. V.; Spaepen, F. *Acta Metall.* **1979**, *27* (12), 1855–1859.

(31) Kalb, J. A.; Wuttig, M. Publikationsserver der RWTH Aachen University 2006.

(32) Olesinski, R. W.; Abbaschian, G. J. *Bull. Alloy Phase Diagr.* **1986**, *7* (3), 219–222.

(33) Mauro, J. C.; Yue, Y.; Ellison, A. J.; Gupta, P. K.; Allan, D. C. *Proc. Natl. Acad. Sci.* **2009**, *106* (47), 19780–19784.

(34) Kalb, J. a.; Wuttig, M.; Spaepen, F. *J. Mater. Res.* **2007**, *22* (03), 748–754.

(35) Derk Jan Adelerhof, European Phase Change and Ovonics Symposium, 2004, epcos.org (http://www.epcos.org/library/Library2004.htm).

(36) Ediger, M. D. *Annu. Rev. Phys. Chem.* **2000**, *51* (1), 99–128.

(37) Ohshima, N. *J. Appl. Phys.* **1998**, *83* (10), 5244–5250.

(38) Privitera, S.; Bongiorno, C.; Rimini, E.; Zonca, R. *Appl. Phys. Lett.* **2004**, *84* (22), 4448–4450.

(39) Morales-Sánchez, E.; Prokhorov, E. F.; González-Hernández, J.; Mendoza-Galván, A. *Thin Solid Films* **2005**, *471* (1–2), 243–247.

(40) Redaelli, A.; Pirovano, A.; Tortorelli, I.; Ielmini, D.; Lacaita, A. L. *IEEE Electron Device Lett.* **2008**, *29* (1), 41–43.

(41) Choi, Y.; Jung, M.; Lee, Y.-K. *Electrochem. Solid-State Lett.* **2009**, *12* (7), F17–F19.

(42) Tominaga, J.; Shima, T.; Fons, P.; Simpson, R.; Kuwahara, M.; Kolobov, A. *Jpn. J. Appl. Phys.* **2009**, *48* (3S1), 03A053.

(43) Incropera, F. P.; De Witt, D. P. **1985**.

(44) Şahin, H. M.; Kocatepe, K.; Kayıkcı, R.; Akar, N. *Energy Convers. Manag.* **2006**, *47* (1), 19–34.

(45) Risk, W. P.; Rettner, C. T.; Raoux, S. *Appl. Phys. Lett.* **2009**, *94* (10), 101906.

(46) Kalb, J. A. **2006**.

(47) Nelder, J. A.; Mead, R. *Comput. J.* **1965**, *7* (4), 308–313.

(48) Eising, G.; Pauza, A.; Kooi, B. J. *Cryst. Growth Des.* **2013**, *13* (1), 220–225.

(49) Shakhvorostov, D.; Nistor, R. A.; Krusin-Elbaum, L.; Martyna, G. J.; Newns, D. M.; Elmegreen, B. G.; Liu, X.; Hughes, Z. E.; Paul, S.; Cabral, C.; Raoux, S.; Shrekenhamer, D. B.; Basov, D. N.; Song, Y.; Müser, M. H. *Proc. Natl. Acad. Sci.* **2009**, *106* (27), 10907–10911.

Chapter 4

Size-dependent crystallization of GeSbTe nanoparticles

Abstract

Chalcogenide-based nanostructured phase-change materials (PCMs) are considered promising building blocks for non-volatile memory due to their high write and read speeds, high data-storage density, and low power consumption. Top-down fabrication of PCM nanoparticles (NPs), however, often results in damage and deterioration of their useful properties. Gas-phase condensation based on magnetron sputtering offers an attractive and straightforward solution to continuously down-scale the PCMs into sub-lithographic sizes. Here we unprecedentedly present the size dependence of crystallization for $Ge_2Sb_2Te_5$ (GST) NPs, whose production is currently highly challenging for chemical synthesis or top-down fabrication. Both amorphous and crystalline NPs have been produced with excellent size and composition control with average diameters varying between 8 and 17 nm. The size-dependent crystallization of these NPs was carefully analyzed through in-situ heating in a transmission electron microscope, where the crystallization temperatures (T_c) decrease when the NPs become smaller. Moreover, methane incorporation has been observed as an effective method to enhance the amorphous phase stability of the NPs. This work therefore elucidates that GST NPs synthesized by gas-phase condensation with tailored properties are promising alternatives in designing phase-change memories constrained by optical lithography limitations.

Based on *Size dependent and tunable crystallization of GeSbTe phase-change nanoparticles*,
B. Chen, G. ten Brink, G. Palasantzas, B. J. Kooi, *Scientific Reports* 6, (2016), 39546.

4.1 Introduction

Phase-change materials (PCMs) have attracted intensive interests, because they offer large optical and electrical contrast between amorphous and crystalline phases in combination with rapid and reversible switching between these two phases and with excellent prospects for down-scaling. This unique set of properties makes PCMs excellently suited for data storage applications (rewriteable optical media and phase-change random-access memory)[1–3] and future applications, including neuromorphic computing,[4,5] flexible displays,[6] logic devices[7], plasmonic-based circuits,[8] optically reconfigurable metasurfaces and all-photonic devices.[9] Because of the potential advantages, such as ultra-high switching speed and density of data storage,[10,11] down-scaling of the PCMs into nanostructured form has evoked intensive explorations, where pronounced size-dependence on physical properties has been revealed, such as size-dependent crystallization and polar ordering.[12–15] For example, solution based GeTe nanoparticles (NPs) with an average diameter of 1.8 nm display a crystallization temperature (T_c) of 400 °C, 220 °C higher than bulk GeTe (~180 °C).[12,13] Furthermore, size-dependent nucleation and activation energy for crystal growth have been observed $Ge_2Sb_2Te_5$ (GST) nanowires when down-scaled their widths to tens of nanometers.[15]

GST, the prototypical PCMs, exhibits the fastest phase transition measured in memory devices so far.[7] The technological relevance of scaling memory devices and the scientific interest to understand size-effects on crystallization have stimulated many investigations on three dimensional down-scaling of GST PCMs. GST nanogaps, connected by carbon nanotube electrodes, have been prepared via top-down process, displaying a much lower switching current (two orders of magnitude) than the ‘state-of-the-art’ devices.[11,16] Nevertheless it is highly challenging to control the sizes of the phase-change nanogaps (ranging from 20 nm to 300 nm in 100 memories) as they are for instance produced by electrical breakdown of the carbon nanotube. In another work,[17] GST nanodots have been prepared by self-assembled block-copolymers as a patterning template for PCM deposition, where GST nanodots with an average diameter of around 15 nm show an anomalously direct transition from the amorphous to the rhombohedral phase at around 400 °C with some unknown peaks in X-ray diffraction patterns, bypassing the rock-salt phase which is usually formed for more bulk-like GST during heating.

Compared to top-down processing, bottom-up techniques provide remarkably better control in size and shape of the materials.[18] Although solution based synthesis can produce extraordinary GeTe NPs, it remains highly challenging to synthesize other PCMs NPs, such as binary GeSb or even more complicated ternary (pseudo-binary) GeSbTe systems.[18] Laser ablation is another alternative that has been explored to produce GST NPs, yet inconsistent but exceptional results have been reported on the crystallization of GST NPs. The GST NPs prepared by this method were observed to form a rhombohedral phase dominated mixture at lower temperature and to have pure rock-salt structure at higher temperatures. Although the same phase-change sequences are observed, the critical temperatures showed a big discrepancy in these two works (300 and 400 °C [19] versus 100 and 200 °C,[20] respectively). More importantly, the wide size distribution of these NPs (4-30 nm and 5-25 nm) makes them unsuitable to explore the size-dependent crystallization. From the contradictory results on GST NPs described above, the crystallization of GST NPs remains elusive, in particular concerning the size-dependence of crystallization. More elaborate and systematic investigations are desired to understand size dependence of the amorphous to crystalline transition of GST NPs. Magnetron sputtering based on gas-phase condensation is a one-step and promising solution-free method to produce NPs. The NPs produced by this method are 'clean' (without surrounding ligands), enabling to exempt the possible influence from the ligands. The narrow size distributions of the produced NPs enable statistical studies on the size-dependence of crystallization. In this manuscript we present a systematic study of the crystallization of as-deposited amorphous GST NPs with scalable sizes varying with a factor of two. Adopting magnetron sputtering based on inert gas condensation, the lithographic limitations in size are overcome. Size-dependent crystallization has been unprecedentedly observed for these NPs via in-situ heating in a transmission electron microscope (TEM). Simultaneously, methane, as an incorporation gas, has been found to remarkably increase the crystallization temperatures, indicating a facile method to enhance the stability of the amorphous GST NPs. This study therefore can facilitate further developments of devices based GST PCMs at sub-lithographic scales.

4.2 Experimental methods

4.2.1 $Ge_2Sb_2Te_5$ nanoparticles preparation

The $Ge_2Sb_2Te_5$ (GST) nanoparticles (NPs) with different phase states and sizes were produced by magnetron sputtering with inert gas condensation in a home-modified nanoparticle system Nanosys50 from Mantis Deposition Ltd. The sample chamber was evacuated to a base pressure of 10^{-8} mbar. Argon (purity of 99.9999%) was used to produce the supersaturated vapour via magnetron sputtering the $Ge_2Sb_2Te_5$ target (purity of 99.99%). Hydrogen or methane was used to facilitate the formation of clusters. Note that the amount of hydrogen or methane used can only be specified qualitatively, because a gauge measuring the gas flow precisely is lacking. Different discharge currents were used to modify the as-deposited phase of the NPs, i.e., 0.15 A for amorphous NPs and 0.3 A for crystalline NPs. Helium (purity of 99.999%) was used to tune the sizes of the NPs. The NPs were directly deposited on carbon grids for transmission electron microscope characterization.

4.2.2 $Ge_2Sb_2Te_5$ nanoparticles characterization

The morphology of the NPs was characterized instantly after deposition by transmission electron microscope (TEM, JEOL 2010) at 200 kV. The crystalline structure was characterized by high-resolution TEM in JEOL 2010F at 200 kV. The composition of the NPs was characterized by energy disperse X-ray spectrometry (EDS) attached to the TEMs (Thermo Instruments on the JEOL 2010 and Bruker Quantax on the JEOL 2010F). In-situ heating was used to measure the crystallization temperature of the amorphous NPs. The in-situ heating in TEM (JEOL 2010) was performed to monitor the crystallization process right after the deposition of the phase-change NPs. A single tilt heating holder (Gatan Model 628) with the temperature controlled by a SmartSet Hot Stage controller (Gatan Model 901) was used for in-situ heating. The temperature accuracy of the indicator is about 0.1 °C. Although the absolute error to determine the actual temperature of the observed TEM specimen area can be substantially larger, it is essential to note here that the observed *differences* in temperature (e.g. as a function of particle size or methane addition) when reproducing experiments very carefully can indeed be very small. Heating rates adopted here were about 1 °C min^{-1} at temperatures above 100 °C. Selected area electron diffraction patterns were recorded at the same area when the sample was heated to a certain temperature. The area selected to record the diffraction patterns were close to the copper bar at the edge of the whole TEM membrane, to minimize the temperature gradient between the heating area and the NPs. During heating, the electron beam was shifted to the copper bar in order to avoid the influence of the electron beam on the crystallization of the NPs.[21] At each temperature step (2 °C), a time interval of 30 seconds was taken for the sake of stabilization of the TEM membrane to avoid the influence of drifting caused by thermal expansion. In the experiments we adopted the largest selected area diffraction aperture (JEOL 2010) for all the measurements, which probes an area of the sample with a diameter of 2.5 µm. Since the NP density on the sample is in the range from 1500-3000 μm^{-2}, the number of particles analyzed to determine a crystallization temperature T_c is typically in-between 7500-15000. Azimuthal integration has been applied to the diffraction patterns in order to derive in a straightforward manner the intensities for different diffraction rings as function of the distance in reciprocal space to the centre point. The azimuthal integration of the diffraction patterns was performed by the PASAD plug-in (http://www.univie.ac.at/-pasad/) in Digital Micrograph software in order to derive the evolution of the diffraction intensity with temperature.[22] The errors in T_c have been determined as the standard error directly obtained from our fitting procedure in the software (Origin 8.5). The fitting quality was estimated by the adjusted R^2.

4.3 Results and Discussion

4.3.1 Control of crystallinity

In order to characterize the stoichiometry of the nanoparticles (NPs), energy dispersive X-ray spectrometry (EDX) has been performed. Results show for a large number of particles an average ratio of Ge:Sb:Te=20:23:57 (±1) at.% for all the samples produced, demonstrating an extraordinary agreement with the nominal composition of $Ge_2Sb_2Te_5$ (Ge:Sb:Te=22:22:56 at.%). An EDX spectrum is shown as an example in Figure 4.5 of the Appendix A. It is important to control the phase state for the as-deposited NPs, both out of scientific interest but also because of the challenge to amorphize the NPs directly upon deposition allowing subsequent crystallization to be studied. By tuning the deposition settings, both amorphous and crystalline NPs have been successfully produced. The phase state of these NPs was confirmed by high resolution transmission electron microscopy (HRTEM), as shown in Figure 4.1. Figure 4.1a displays the amorphous nature of the as-deposited NPs due to the lack of lattice fringes, which in contrast can be unambiguously observed in crystalline NPs; see Figure 4.1b. The measured interplanar spacings are d_{111}=0.353 nm, d_{200}=0.306 nm. Associated with the measured value of the angle between these two planes (~54.5°) derived from both the HRTEM image and the corresponding fast Fourier transform (FFT, as shown in inset of Figure 4.1b), a rock-salt structure with a lattice parameter of 0.612±0.005 nm is derived. This lattice parameter is about 2% extended compared to the value (0.600-0.601 nm) for bulk $Ge_2Sb_2Te_5$ PCMs.[23,24] We consistently found this 2% extension for a large number of particles and this is also consistent with the observation for GST NPs in another work (0.611±0.002 nm).[25] The (200) and the (111) planes are labelled in the FFT image (inset in Figure 4.1b), suggesting a rock-salt structure with a zone axis of <110].

A core-shell structure is absent for the NPs in the HRTEM images, indicating that the NPs were not significantly oxidized. The FFT image (inset of Figure 4.1b) also confirms this because no splitting of diffraction spots can be observed, demonstrating only one kind of crystal structure in the nanoparticle. The HRTEM image also shows the single crystal nature of the nanoparticle. Actually from all the HRTEM images recorded no sign of polycrystalline structures has been observed for the GST NPs, most probably due to the small size of the NPs (less than 20 nm in diameter).

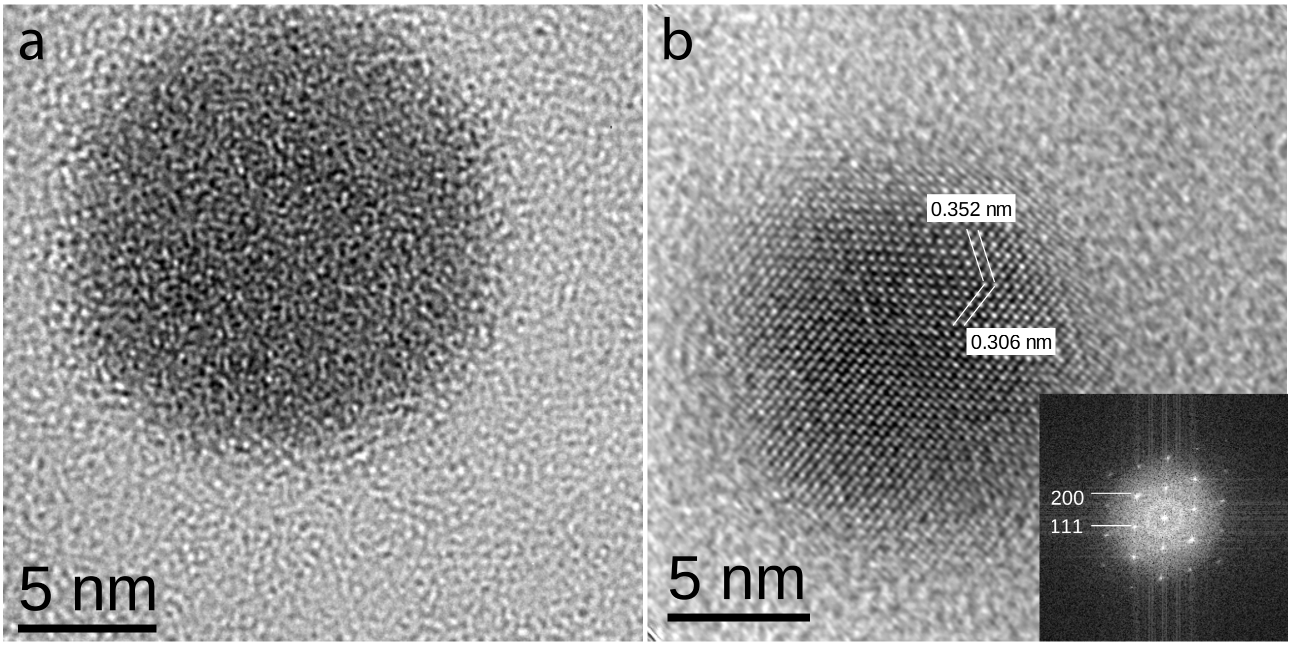

Figure 4.1 High resolution transmission electron microscopy (HRTEM) images of the amorphous (a) and crystalline (b) $Ge_2Sb_2Te_5$ nanoparticles (GST NPs). (b) shows that GST nanoparticle possesses a rock-salt structure, and that imaging is recorded along the <110] zone axis. The lattice parameter given by this HRTEM image is 0.612±0.005 nm, 2% extended compared to the bulk GST. Inset in (b) displays the fast Fourier transform of this image with two reflections indicated.

The only difference in directly creating either amorphous or crystalline NPs is the discharge current applied to the magnetron sputtering nanocluster deposition system, leading to a difference in power supplied to the system. In comparison to the crystalline sample, a lower current was used for the amorphous sample (0.30 versus 0.15 A). In a previous work, it has been demonstrated that the solubility and the diffusivity of the atoms in the NPs can be tuned by adjusting the deposition settings (i.e., the power and the argon flow), where higher input power indeed caused phase segregation in Mo-Cu NPs.[26] The higher power input leads to a higher kinetic energy to the atoms in the plasma, resulting in the formation of liquid phase clusters. As is well known, an extremely high quenching rate (above 10^9 K s^{-1} [27–29]) is required to produce amorphous phase PCMs since they have to be in general poor glass formers. Since the quenching rate is not high enough in the aggregation chamber to form amorphous phase, crystalline NPs develop. When a lower discharge current is used, clusters remain below the melting temperature and atoms randomly coalesce and then form NPs. The energy of the atoms (Ge/Sb/Te) gained in the plasma is sufficient to form a nanoparticle, but not enough to overcome the energy barrier of forming a crystalline structure, where amorphous phase is formed analogous to sputtered amorphous films. This hypothesis can be further confirmed by the fact that the ratio of crystalline NPs among all the NPs produced becomes smaller when helium gas (while the other settings remain the same) is used to accelerate the cooling rate in the aggregation chamber. Note that the critical discharge current required to form the liquid state of GST system is much lower than that of the Mo-Cu system (0.55 A), because the melting temperature of Mo-Cu is much higher than the one of GeSbTe.

4.3.2 Morphology and size distribution

As described in the previous section, the discharge current has significant impact on the phase state of the as-deposited NPs. So a relatively low discharge current (0.15 A) was used to produce amorphous NPs. The morphology of these NPs was characterized by TEM, as shown in Figure 4.2. Figure 4.2a-c show the GST NPs with different sizes. The amorphous nature of these NPs is confirmed by the selected area electron diffraction (SAED) patterns (insets in the bright field images), owing to the fact that lacks sharp diffraction features, but exists a broad halo. The amorphous NPs exhibit approximately spherical morphology, while the crystalline ones display anisotropic features with facets. Note that the NPs shown here were produced with hydrogen as extra gas on top of the standard argon gas. No literature has been found to confirm the fact that a potential doping with hydrogen has influence on the crystallization temperature (T_c) of PCMs. With more helium as cooling gas in the cluster system, the sizes of the NPs can be significantly reduced due to the two-fold impact of helium: 1) helium is a better thermal conductor than argon, leading to more efficient reduction of kinetic energy of the atoms in the plasma; 2) the presence of helium increases the pressure in the aggregation chamber, resulting in a bigger driving force pushing the NPs out of the aggregation volume to the main chamber.[26,30] No helium was used for the preparation of the NPs in Figure 4.2a, while 10 and 20 sccm of helium were adopted to reduce the diameter of the NPs shown in Figures 4.2b and 4.2c, respectively. The average diameters of these 3 samples are 13.2±1.4 nm, 10.7±1.7 nm and 8.4±1.7 nm, as shown in Figure 4.2d, which will be referred to as big, medium and small NPs.

All of the NPs in these three samples show a relatively narrow size distribution. Figure 4.2 also suggests that the size distributions become wider when the average sizes of NPs shrink, i.e., from 10% for the big NPs (13.2 nm) to ~20% for the small ones (8.4 nm). The as-deposited NPs are well separated when the coverage is low; see individual NPs with low coverage (~ 7%) in Figure 4.6 of the Appendix A. When the coverage becomes higher (~15 % in Figure 4.2), which is essential to have enough signal in SAED patterns when performing in-situ heating in TEM (see next section), the overlapping between NPs becomes inevitable. However, clear boundaries (see the examples indicated by the white arrows in Figure 4.2a) can be observed between NPs, demonstrating that coalescence does not occur in these samples. However, when the amount of helium used is large, a small fraction of coalesced NPs can be observed (2 clusters of coalesced NPs can be seen in area with dimension of 250×250 nm^2), indicated by the white arrows in Figure 4.2c. This coalescence most probably stems from the higher purity of the helium aggregation gas than argon.

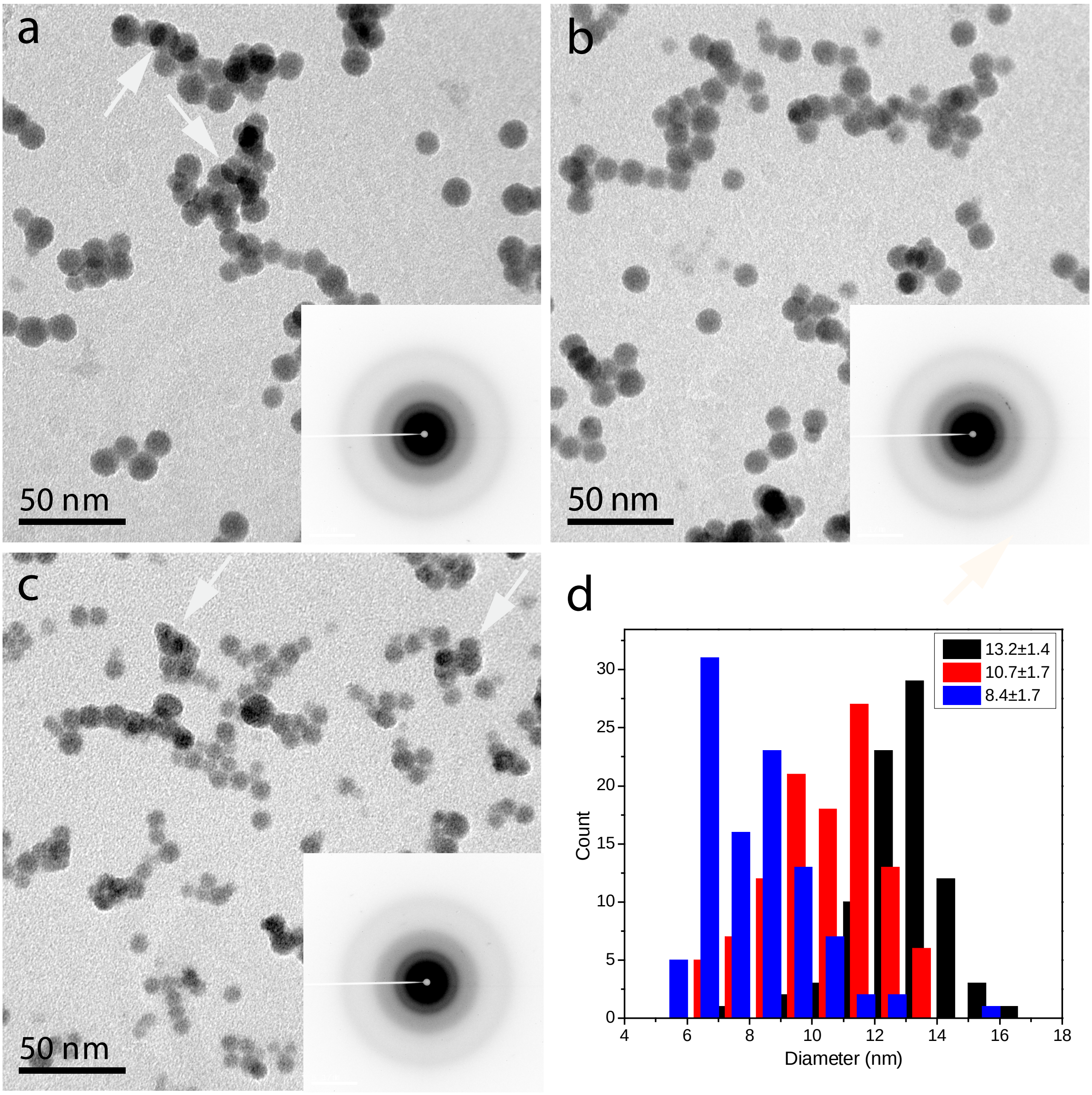

Figure 4.2 Bright field TEM images of amorphous GST NPs with different average diameters (Ø). a) large NPs, Ø=13.2±1.4 nm; b) medium-sized NPs, Ø=10.7±1.7 nm; c) small NPs, Ø=8.4±1.7 nm. (d) shows the corresponding size distributions for these three samples. The white arrows in a) indicate NP overlap, but not real aggregation, whereas the white arrows in c) indicate NP aggregation.

The small NPs always have the tendency to coalesce in order to reduce their surface energy, making coalescence energetically favorable. The impurities on the surface of the NPs, generally in the form of a thin oxide shell, play a role in preventing the NPs from coalescing. In our experiment, helium has a higher purity than argon (99.9999 % vs 99.999 %). When only argon is used, the small amount of impurity causes an oxide shell (rich in Ge, because this is the element with the highest oxygen affinity) outside the NPs, that prevents the NPs from coalescence. When more pure helium gas is used, less oxide will be formed and therefore coalescence can take place. Moreover, when helium is used the NP size is reduced and thereby the driving force for coalescence is increased, as shown in Figure 4.2c.

4.3.3 Size-dependent crystallization

Crystallization is one of the most relevant properties to be explored when PCMs are scaled down as it also directly links to the stability of the amorphous phase. Because of the small scale (~10 nm) of the objects and therefore extremely low mass (in nanogram scale), it is extremely difficult to study the crystallization of the NPs by for instance conventional differential scanning calorimetry (DSC). In-situ heating in a TEM therefore has been performed to characterize the crystallization process for the GST NPs. As can be observed in Figure 4.3a-c, the broad amorphous halo of the GST NPs changes into sharp rings in the diffraction patterns under heating. The evolution of the diffraction patterns as a function of temperature during in-situ heating in TEM indicates the crystallization process of GST NPs, as shown in Figure 4.3d. By fitting the evolution of the intensity for {220} planes (as shown in Figure 4.3e), the T_c of the GST NPs have been derived (details of the methods, see the method in chapter 2 and 4).

The T_c derived from fitting are 143.8±0.5 °C, 139.8±0.3 °C and 138.3±0.6 °C for the big, medium and small NPs. Note that the T_c for bulk GST range from 150 to 160 °C for different measurements.[31–35] It is noticeable that the coalescence of the NPs produced with 20 sccm helium flow has negligible impact on the T_c of the NPs due to the small number of coalesced NPs compared to the total number of NPs (2 clusters vs ~100 NPs in Figure 4.2c). Hence, a (weak) size-dependence of crystallization is revealed here for GST NPs. Interestingly the T_c decrease when the average sizes of nanoparticles reduce, which is opposite to the observation for GeTe NPs.[12,13] 1st order derivatives of these fitting curves have been obtained and are depicted in Figure 4.7 of the Appendix A. It is noticeable that the full width at half maximum (FWHM) (of the peaks in the derivative curves) for the small NPs is slightly larger than that of the big NPs, indicating that a wider temperature range is needed to completely crystallize the small NPs.

Furthermore, the bright field TEM images for NPs after heating demonstrate that the GST NPs do not evaporate or coalesce during heating. The only visible alteration from these images is the more apparent electron scattering contrast, as the crystalline part usually appears darker in bright field image. Even at the overlapping boundaries, the circular rim of these NPs remains very clear. In contrast, significant sintering of NPs was observed in GeTe NPs by chemical synthesis during crystallization.[13]

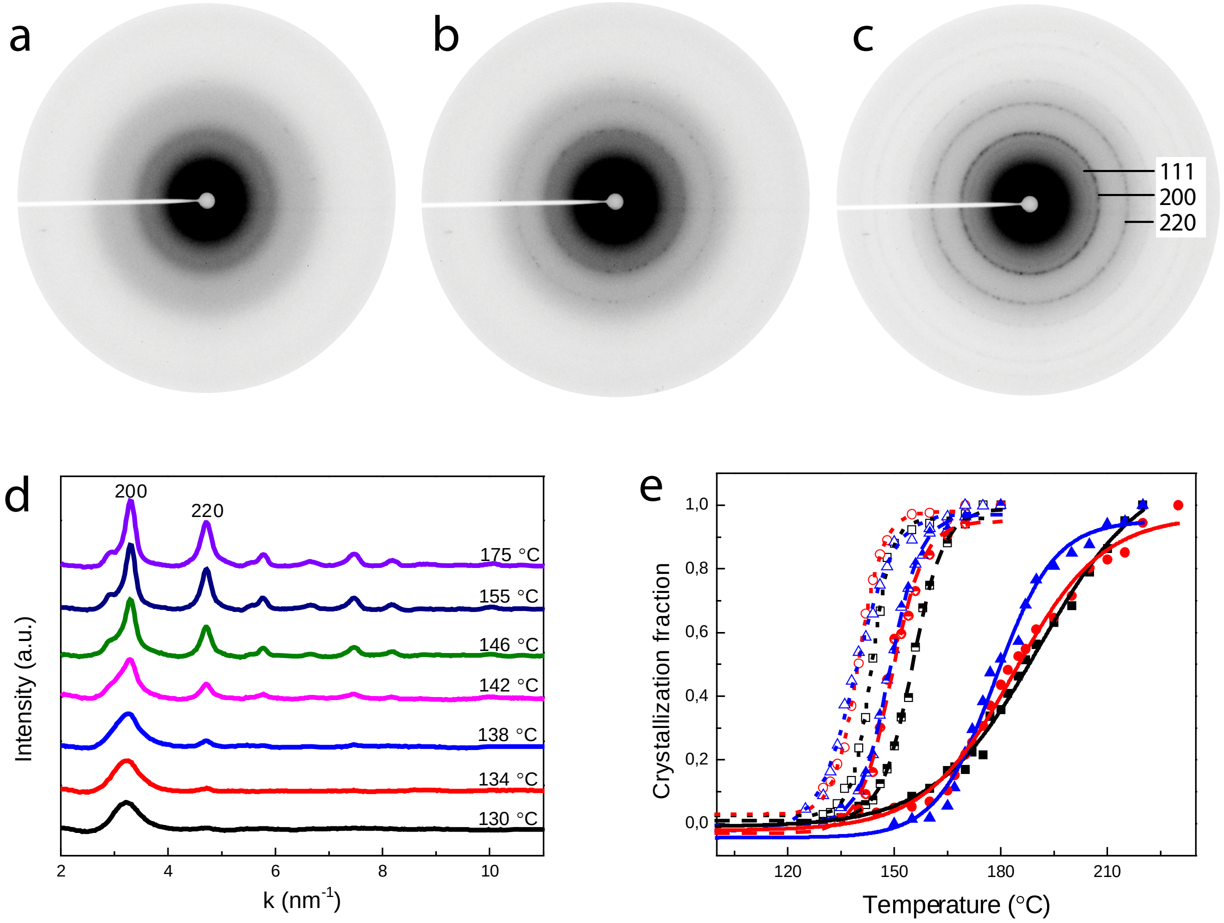

Figure 4.3 Crystallization of GST NPs via in-situ heating. (a)-(c) show the selected area electron diffraction patterns of the big NPs shown in Figure 4.2a at room temperature, 140 and 175 °C, respectively. Only an amorphous halo exists in the diffraction pattern recorded at room temperature. Some faint, discrete diffraction spots appear when the sample is heated to 140 °C, and finally sharp diffraction rings consisting of discrete spots confirm the phase transition process. (d) Evolution of the diffraction patterns as a function of the heating temperature. (e) The normalized phase transformation fraction as function of temperature for three different sets of samples, where each set comprises three samples with different average NP diameters. The open symbols are for the NPs produced with hydrogen, while the half open and solid symbols are for the NPs produced with low and high amounts of methane, respectively. Black, red and blue colour means big, medium-sized and small NPs in each session, respectively. The continuous curves in this figure are the fitting results using the Boltzmann function. The fitting quality of was estimated by adjusted R^2, which is in the range 0.988 to 0.998.

4.3.4 Enhancement of the amorphous stability via methane

As shown in the previous section, the T_c of the GST NPs slightly decreases when the average sizes of the NPs reduce. Although the decrease here is not dramatic, further down-scaling (e.g. to sub 5 nm) is likely to create some challenges for the stability of the amorphous phase. However, a facile method to increase the T_c (therefore the stability of the amorphous phase) of the GST NPs has been discovered. Instead of using hydrogen as extra gas, methane was used to initiate the deposition process. NPs with different sizes have been produced both with low and high amounts of methane, as shown in Figure 4.8 and 4.9 in the Appendix A. Figure 4.8 depicts the morphology of the GST NPs produced with a low amount of methane. Helium was also employed here to reduce the sizes of the NPs. The average diameters of these three samples (Figure 4.8a-c) are 15.1±1.4 nm, 9.8±1.9 nm and 7.9±1.6 nm, respectively. Sizes distributions of these 3 samples are shown in Figure 4.8d, displaying a narrow size dispersion of these samples. A high amount of methane was further used to confirm that the incorporation of methane plays a role in stabilizing the amorphous state of the GST NPs. The TEM images in Figure 4.9 depict the morphology of these NPs. The average diameters of these three samples (Figure 4.9a-c) are 16.8±1.4 nm, 14.5±1.6 nm and 10.7±1.8 nm. Narrow size distributions of these 3 samples are displayed in Figure 4.9d. Similar to the NPs produced with hydrogen, the smaller the NPs are, the wider the size distribution of the NPs become. Coalesced NPs cannot be observed in the bright field TEM images, but only the overlapping of NPs with distinct boundaries. The spherical shape of the NPs indicates their amorphous nature, which is also confirmed by the SAED patterns (insets in Figure 4.8 and 4.9).

For the carbon concentration in the NPs, we could determine by EDS that the NPs produced with the addition of a high amount of methane contained significantly more carbon than the NPs produced with hydrogen (when only the four elements C, Ge, Sb and Te are considered we found 22±11 at.% C and 8±2 at.% C, respectively, whereas a negligible amount of carbon is found for the silicon nitride membrane substrate as reference). The detected amount of carbon can be present both within and surrounding the NPs. Moreover, accurate quantification of the carbon concentration with EDS, particularly for large surface area material such as based on NPs, is by itself already difficult. Therefore, we use the qualitative description of low and high amounts of methane in the present work, where our results still demonstrate that the carbon concentration connected to the NPs increase when going from the NPs produced with hydrogen to ones with a low amount of methane and then to ones with the high amount of methane.

Similar to the previous section, in-situ heating in TEM was performed to characterize the crystallization of these NPs produced with the addition of methane. The transformed phase fractions as function of temperature for these NPs are depicted in Figure 4.3e. The half open symbols are data for the NPs produced with a low amount of methane, while the solid symbols in this figure denote the data for the NPs produced with high amount of methane. The black, red and blue colours represent the big, medium and small NPs, respectively. The T_c obtained through fitting are 155.2±0.2 °C, 149.2±0.5 °C, 148.8±0.2 °C for the big, medium and small NPs produced with low amount of methane. In comparison to the T_c derived for the NPs produced with hydrogen, a significant increase (~10 °C) in T_c is obtained. Furthermore, the high amount of methane during production leads to even higher T_c, i.e., 190.8±1.7 °C, 183.7±1.1 °C, and 177.9±1 °C for the big, medium and the small NPs, respectively. Hence a strong effect (more than 35 °C increase) of methane on the T_c has been observed here for the GST NPs.

Figure 4.7 in the Appendix A presents the 1st order derivatives of the fitting curves in Figure 4.3e, where the T_c of these samples was derived from the peak temperature. From this figure, it is noticeable that the incorporation of methane not only influences the onset temperature of crystallization, but also the crystallization speed. In comparison with the ones produced with hydrogen (open symbols in Figure 4.3e) and low amount of methane (half open symbols in Figure 4.3e), the FWHM for the ones with high amount of methane (solid symbols in Figure 4.3e) is significantly larger, suggesting that a larger temperature range is required to accomplish the crystallization process.

It is well-known that crystallization involves two processes: nucleation and subsequent crystal growth. The width in temperature (non-abruptness) of the crystallization process originates from the difference in incubation time for nucleation of the various NPs, because the crystal growth rate is fast (above 10^{-6} m s^{-1} for GST thin films at this temperature [36]) once nucleation has occurred in an NP and will finish within the time for stabilizing the specimen (30 s). The overall crystallization curves shown in Figure 4.3e therefore represent the ensemble of the crystallization of individual NPs with their variation in the incubation times for nucleation. For the temperature interval we consider the nucleation rate increases with time and temperature. Therefore, we would expect a more abrupt crystallization when this transition occurs at higher temperatures. However, in the case of methane addition, where the transition is shifted to higher temperature, we observe a slower transition. This thus implies that the addition of a high amount of methane retards the overall process of crystallization significantly. The effect of methane is thereby similar to carbon doping which retards the crystallization process in $Ge_2Sb_2Te_5$ films.[37]

The T_c as a function of size and the incorporated methane is illustrated in Figure 4.4. In addition, the T_c of GeTe NPs (black diamonds and triangles) are also shown in this figure for contrast.[12,13] All the values of the average diameters and the T_c are displayed in Table 4.1 of the Appendix B. Similar size-dependent trends are observed for all of these samples, no matter the NPs are produced with hydrogen or methane. In comparison to the size-dependence of the T_c, the methane gas produces a much more pronounced effect.

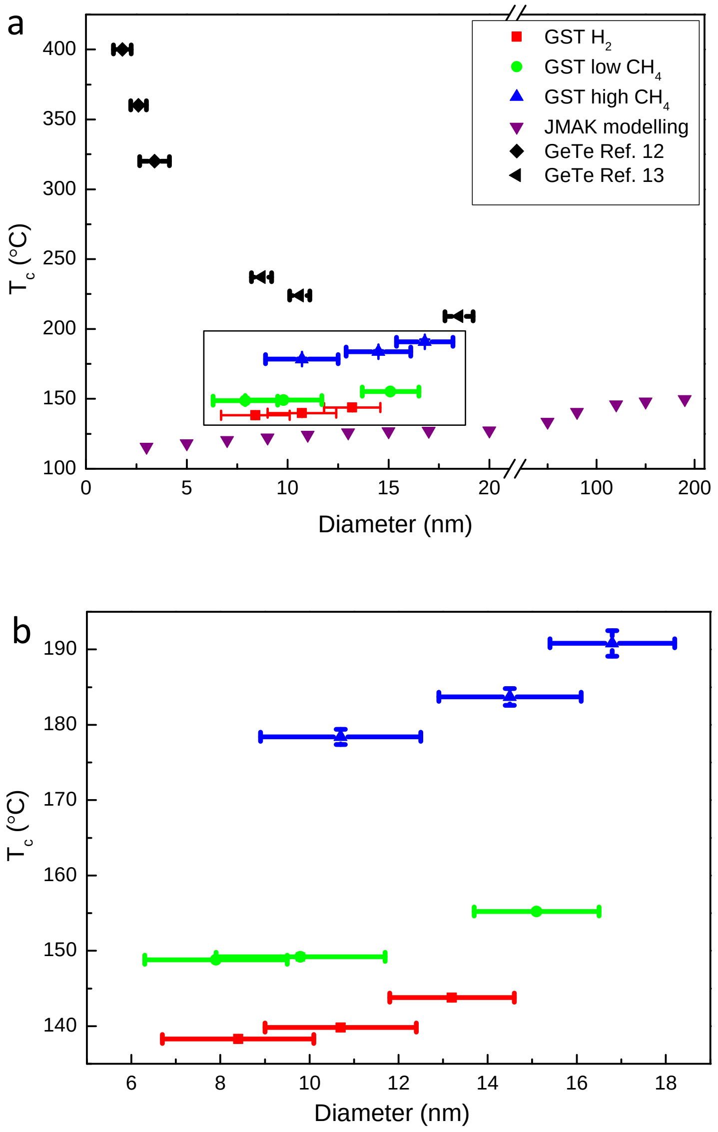

Figure 4.4 (a) Size-dependence of the crystallization temperatures for GST and GeTe NPs. The blue triangles, green circles and red squares are the T_c data for GST NPs at different diameters and different incorporation gases as determined in the present work. The data in black are T_c for GeTe NPs at different diameters as taken from literature.[12,13] Opposite size-dependence of T_c can be observed for GeTe and GST NPs. Numerically calculated data based on experimental data from GST nanowires are displayed in purple triangles,[15] demonstrating the same trend as the GST NPs in the present work. (b) The close-up of the rectangular area in (a).

Size-dependent crystallization has been reported in many glass forming liquids. For example, lower crystallization temperature has been reported when the sizes of Si NPs reduce.[38] However, the weak relation between the size and T_c is unexpected for GST NPs. In previous works,[10,15] the activation energy for crystal growth has been reported to reduce from 2.34 eV to 1.86 eV for $Ge_2Sb_2Te_5$ nanowires when their widths reduce from 190 nm to 20 nm. Meanwhile, the nucleation rates increase at least 4 orders of magnitudes due to surface-induced heterogeneous nucleation. Based on these two factors, it is understood that the GST NPs show decreasing T_c when the average sizes decline.

Analogous to previous work,[39] we performed numerical calculations based on Johnson-Mehl-Avrami-Kolmogorov (JMAK) theory and adopting the same heating rate as used in the in-situ TEM measurements in order to simulate the crystallization curves for the relevant sizes around those of the NPs. Utilizing data for size-dependent activation energy and nucleation rate originally found for GST nanowires,[15] the simulated size-dependence of crystallization for GST NPs is presented in Figure 4.4 (purple triangles). The T_c of NPs with a diameter of 200 nm in these numerical calculations is set to ~150 °C, close to that of bulk GST. The same trend of size-dependence can be readily observed for the modelling and the experimental data we obtained for GST NPs (red, green and blue points), i.e., a slight decrease in T_c when the sizes become smaller. However, the T_c observed for the non-doped GST NPs (red squares in Figure 4.4) in the present work are ~20 °C higher than the theoretically predicted values, suggesting that the size-dependence of crystallization for the current GST NPs is weaker than that of nanowires.

In a previous work,[25] a higher T_c (~180 °C) for GST NPs with a diameter of 5.7±1 nm was observed compared to that of bulk GST. Nevertheless, this difference in T_c probably originates from the discrepancy in stoichiometry, as it was also reported that the composition for the NPs (Ge:Sb:Te=28:27:45) differed considerably from the nominal stoichiometry of $Ge_2Sb_2Te_5$ (Ge:Sb:Te=22:22:56). It should be noted that the composition affect the T_c of GST ternary alloy pronouncedly.[40] For instance, the T_c of $Ge_2Sb_2Te_4$ film is reported as 175 °C.[24] Moreover, the alumina layer used to cap the NPs in the previous work is also likely to increase T_c. Providing a compressive stress to the NPs by the capping layer, the amorphous phase can be stabilized, therefore the transformation from amorphous to crystalline is retarded.[41–44] No further information on crystallization of GST NPs with varying sizes has been reported by this group. In comparison, the composition (Ge:Sb:Te=20:24:56, ±1) obtained from the EDS for the NPs we produced here is in remarkably good agreement with the nominal stoichiometry of $Ge_2Sb_2Te_5$ and no capping layer is used in our work.

Surprisingly, the opposite size-dependence trend was found for GeTe NPs studied previously (the black data points in Figure 4.4a),[12,13] where a sharp increase in T_c was observed for decreasing particle size. GeTe NPs with a diameter of 1.8 nm exhibit a T_c of 400 °C in comparison to ~180 °C for bulk GeTe.

The minor size-dependence in the crystallization temperature of the GST NPs observed here is favourable for memory applications, because simultaneously, it is expected that the melting temperatures (T_m) will drop as the NPs become smaller. A sharp decrease in T_m with decreasing size has been widely observed in many different systems, like Au NPs,[45] Ag NPs,[46] and Sn NPs.[47] Since the SET (crystallization) process is usually operated at temperatures between T_c and T_m, a strongly increasing T_c, as observed for GeTe, would be problematic, because it generates a smaller operation window for crystallization and an accompanying reduction in maximum crystallization rate.

Enhancing the stability of amorphous phase in a proper range is usually favourable since higher T_c represents better data retention (at operating temperature e.g. up to 100 °C). The present work demonstrates that the extra gas (methane) plays a promising role to stabilize the amorphous phase of the GST NPs. It has been demonstrated that it is possible to form carbon as by-product when methane is used to accelerate the nucleation in the cluster system.[30] Therefore, carbon can be randomly doped into the NPs during the nucleation of the NPs inside the cluster source. Note that a carbon shell was unambiguously detected for Cu NPs in HRTEM image in a previous work by our group,[28] yet it cannot be clearly observed for the GST NPs in HRTEM image, as demonstrated in Figure 4.10a of the Appendix A. Considering (1) the similarity of the method to produce NPs here and the magnetron sputtering utilized to produce carbon doped GST thin films and (2) the strong effect of methane addition on T_c, we draw the conclusion that this increase of T_c is mainly due to carbon doping and not a carbon shell. In GST and GeTe films, carbon doping has been reported as an effective method to stabilize the amorphous phase. For example, 9 at.% of carbon dopant in $Ge_2Sb_2Te_5$ films results in an increment of ~10 °C of T_c compared to the non-doped film. Further, a high amount of doping (18 at.% of carbon) leads to an increment of 40 °C of T_c.[37] This influence of doping on NPs is surprisingly prominent since the partial pressure of methane is very low (less than 1% even with the high amount of methane) compared to the deposition pressure (determined mostly by argon and helium flow and the target atoms) during sample preparation. In GeTe films, the carbon dopant influence the T_c more intensely, where 4% of carbon dopant results in a T_c of ~290 °C compared to ~180 °C for the non-doped GeTe film.[48] In both cases, the activation energy for crystallization have been increased pronouncedly by carbon doping. To conclude, the tuneable T_c of the GST NPs using methane as an incorporation gas provides an attractive way to enhance the amorphous phase stability. As described above, carbon doping retards the amorphous to crystallization transition, leading to a reduction in crystallization speed around and below T_c.

However, the activation energy for crystallization for carbon doped GST films is higher than that of the non-doped ones.[37] Therefore, the crystallization speed at real operation temperature, which can be 400-500 °C, can probably reach or exceed the speed of non-doped GST. This is very favourable, because then both the data retention as well as SET speed are improved.

4.3.5 Crystallography of the *in-situ* heated GST NPs

The crystal structure after crystallization was determined by HRTEM for the NPs produced with hydrogen and the low amount of methane. Despite some visible {220} facets in the HRTEM image (on the left and right sides of the NP) shown in Figure 4.10a, the faceting is hardly visible in overview images (with lower magnification). A difference between the crystalline NPs directly formed in our NPs deposition system and the ones formed by heating initial amorphous NPs can be expected, because the former ones form directly out of liquid NPs, whereas the latter form inside initially glass-like NPs. This for instance has a clear impact on the temperature and viscosity of the NPs material in which the crystals nucleate and grow. For the crystals forming in the liquid NPs the temperature is higher and the viscosity lower giving much more flexibility during crystallization to affect the initial spherical shape of the NPs to facetted ones. On the other hand, for the crystals forming in the glass-like NPs the temperature is lower and the viscosity higher giving much more rigidity during crystallization not allowing clear overall shape-changes of the initial spherical shape of the NPs to facetted ones.

Surprisingly, a mixture of metastable rock-salt and rhombohedral structures is observed. For the rock-salt structure, the lattice parameter obtained from HRTEM images is consistent with the one of the as-deposited crystalline NPs, with lattice parameter a=0.612±0.005 nm, as shown nicely in Figure 4.10a of the Appendix A. From Figure 4.10b, clear vacancy layers (VL) can be observed in the HRTEM image. This VL is normally absent in rock-salt structure due to the random distribution of the vacancies in this structure, indicating that the transition to the more stable rhombohedral structure, which for bulk GST is expected for clearly higher temperatures,[21,28,32] is already initiated after heating to 175 °C. Moreover, oxide shells or other crystal structures are not observed from these images, suggesting that oxidation is insignificant during heating.

The incorporation gas should not play a role for the merging of VL as the mixture of these two structures is observed in the NPs produced with both hydrogen and methane. A possible reason for this is that the transition temperature from rock-salt structure to rhombohedral structure (T_{c2}) is significantly reduced with scaling down of the PCMs. For $Ge_2Sb_2Te_5$ phase-change films, this temperature has been reported ranging from 240 °C to 370 °C for different measurements.[21,28,32]

However, a size-dependence of T_{c2} has been observed in $Ge_2Sb_2Te_5$ films. While the transition temperature from amorphous to rock-salt structure is hardly changed, the T_{c2} is pronouncedly reduced when the thicknesses of films are reduced. At a thickness of 20 nm, the later temperature has been lowered to ~200 °C.[49] Since the diameters of the GST NPs in the present manuscript are smaller than 20 nm, an even lower temperature is possible for the rock-salt to trigonal structural transition. The samples we performed HRTEM characterization on have been heated to 175 °C, so probably we have reached the onset temperature of the second phase transition. However, this transition is not detected in the SAED patterns in TEM. Further systematic work is needed to understand the mixed structure.

4.4 Conclusions

We have introduced a facile method to produce phase-change $Ge_2Sb_2Te_5$ (GST) nanoparticles (NPs) with excellent crystallinity, size and composition control. The rock-salt structure of the GST NPs exhibit ~2 % extension in lattice parameter compared to bulk GST. In-situ heating of amorphous NPs in transmission electron microscope shows that crystallization is size-dependent, where the crystallization temperatures (T_c) decrease when the NP sizes decrease. However the difference in T_c is only a few Kelvin when the sizes of NPs are typically reduced by a factor of 2 (from 17 to 8 nm), which is preferable for applications. Numerical modelling via JMAK theory illustrates that surface-induced heterogeneous nucleation is able to explain this size dependent crystallization. We expect this phenomenon to be present and dominant in down-scaled phase-change materials. The presence of methane gas during deposition gives rise to a large increase in T_c of ~35 °C compared to when methane is absent and hydrogen is used instead. This work shows for the first time (i) the size-dependent crystallization of GST NPs and (ii) the tuneable crystallization temperatures of GST NPs when methane gas is added during sputtering. Hence, our approach is relevant for the designing of phase-change memories and PCMs-based devices with an active PCM size clearly below 20 nm, which is very hard to achieve with optical lithography.

Appendix A

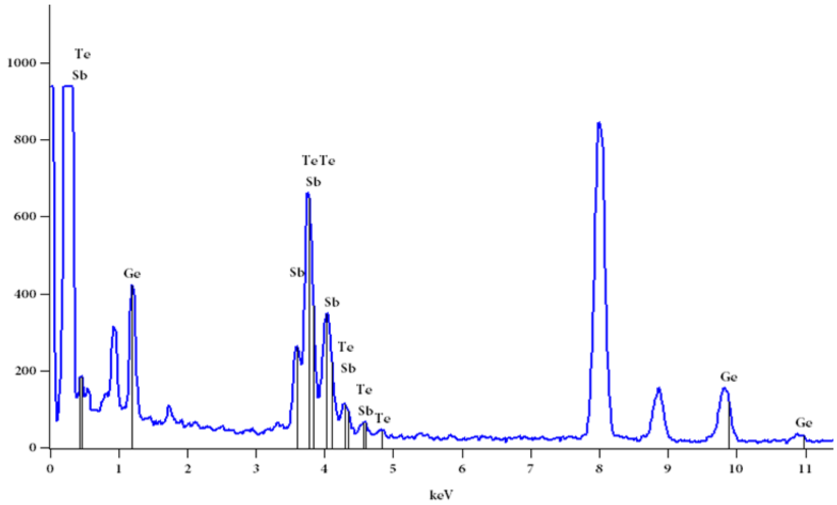

Figure 4.5 Energy dispersive X-ray spectrum, providing information on the stoichiometry of the NPs. The ratio of Ge:Sb:Te derived from the spectrum is 20:23:57 (±1) at%, showing good agreement with the nominal composition of $Ge_2Sb_2Te_5$.

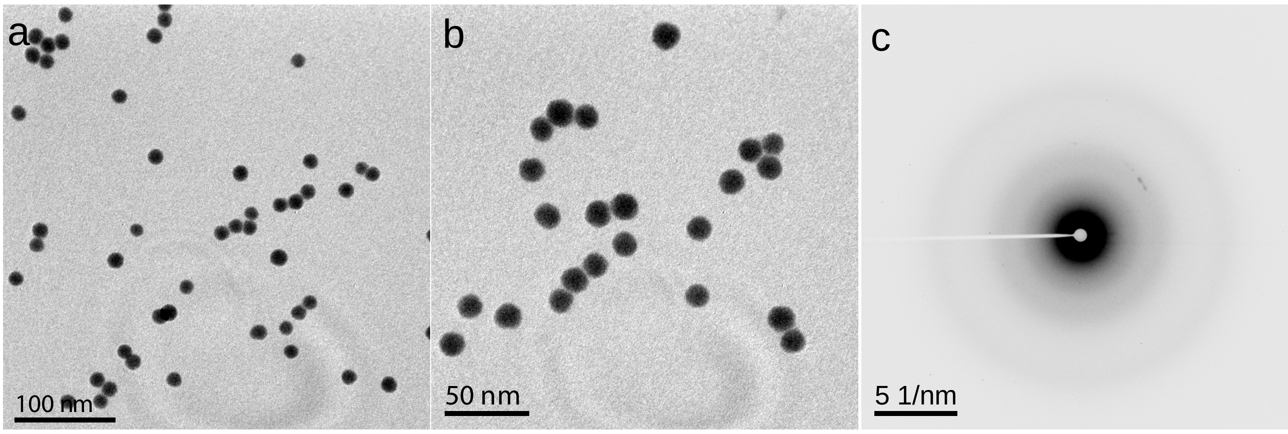

Figure 4.6 Bright-field TEM images showing a low NP coverage (~7.3 %). Overlapping of NPs is not observed in the images (a) and (b). The lack of Bragg diffraction spots in the electron diffraction patterns (c) demonstrates the amorphous nature of these NPs.

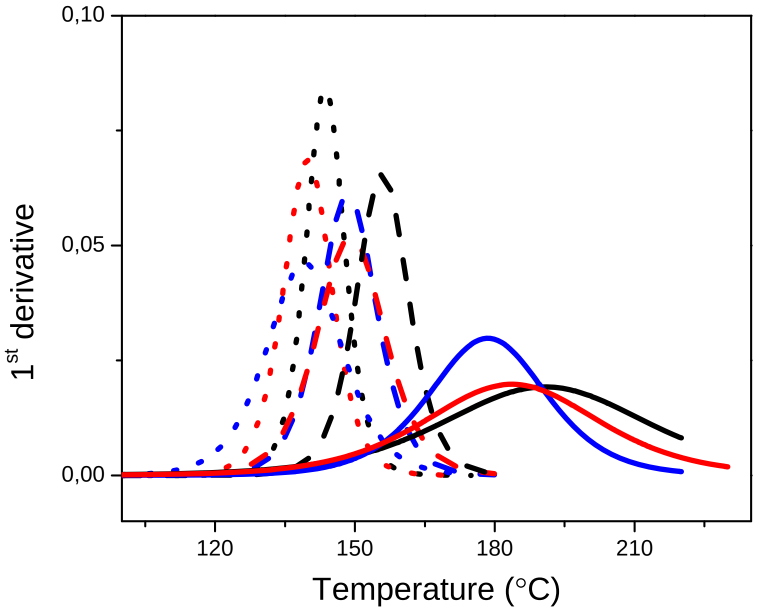

Figure 4.7 The 1st derivatives of the fitted curves in Figure 4.3e of the main text, with the peak indicating the crystallization temperature (T_c) of each sample. Black, red and blue colour means big NPs, the medium-sized NPs and the small NPs in each session.

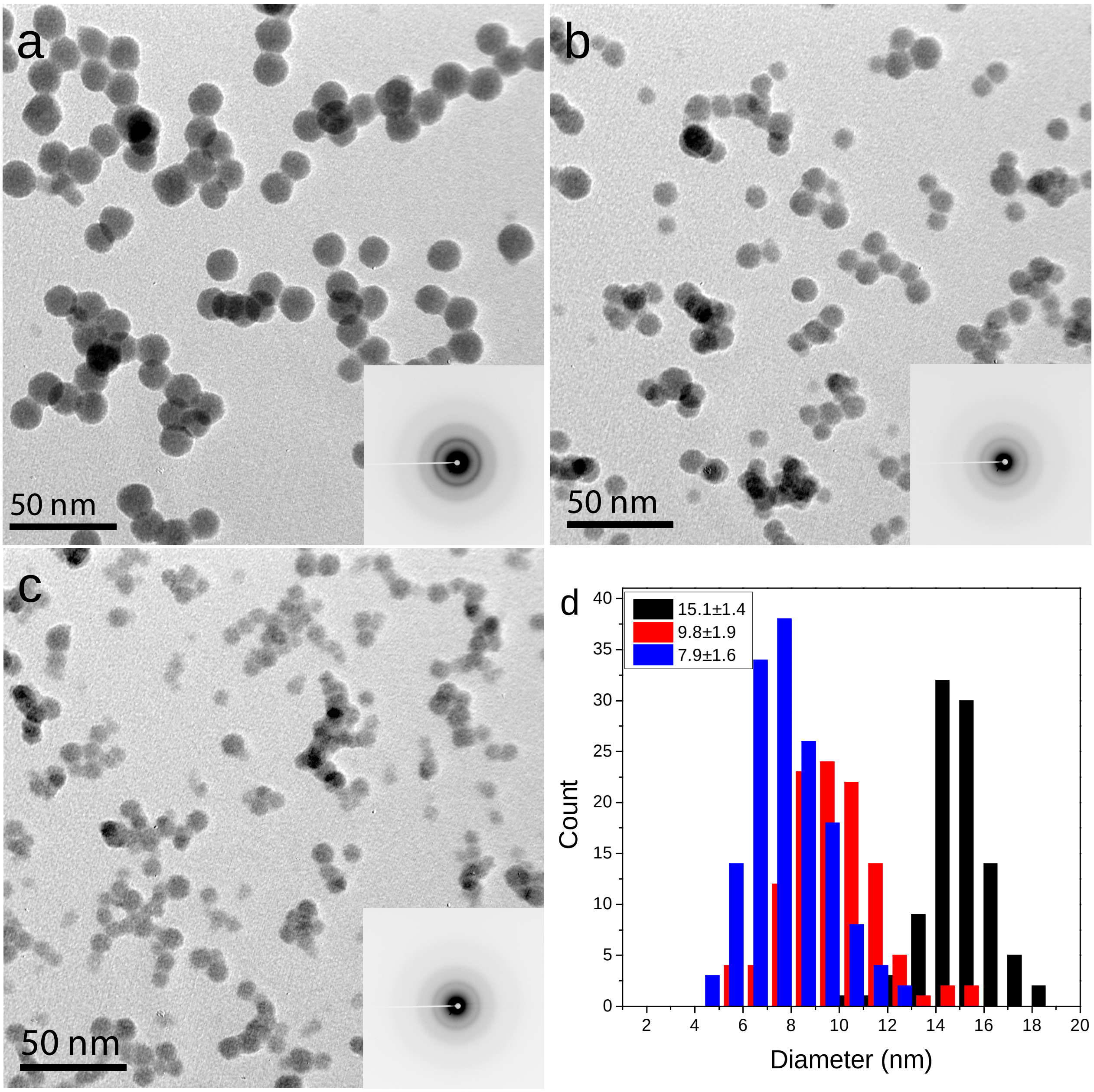

Figure 4.8 TEM images (a-c) showing the morphology of the GST NPs produced with a low amount of methane. The amount of helium used was 0 (a), 10 (b) and 20 (c) sccm. The average diameters of the NPs shown in the three pannels are 15.1±1.4 nm (a), 9.8±1.9 nm (b) and 7.9±1.6 nm (c). (d) Size distributions of the three different samples shown in a-c. Insets SAED patterns in the images in a-c indicate the amorphous nature of the NPs.

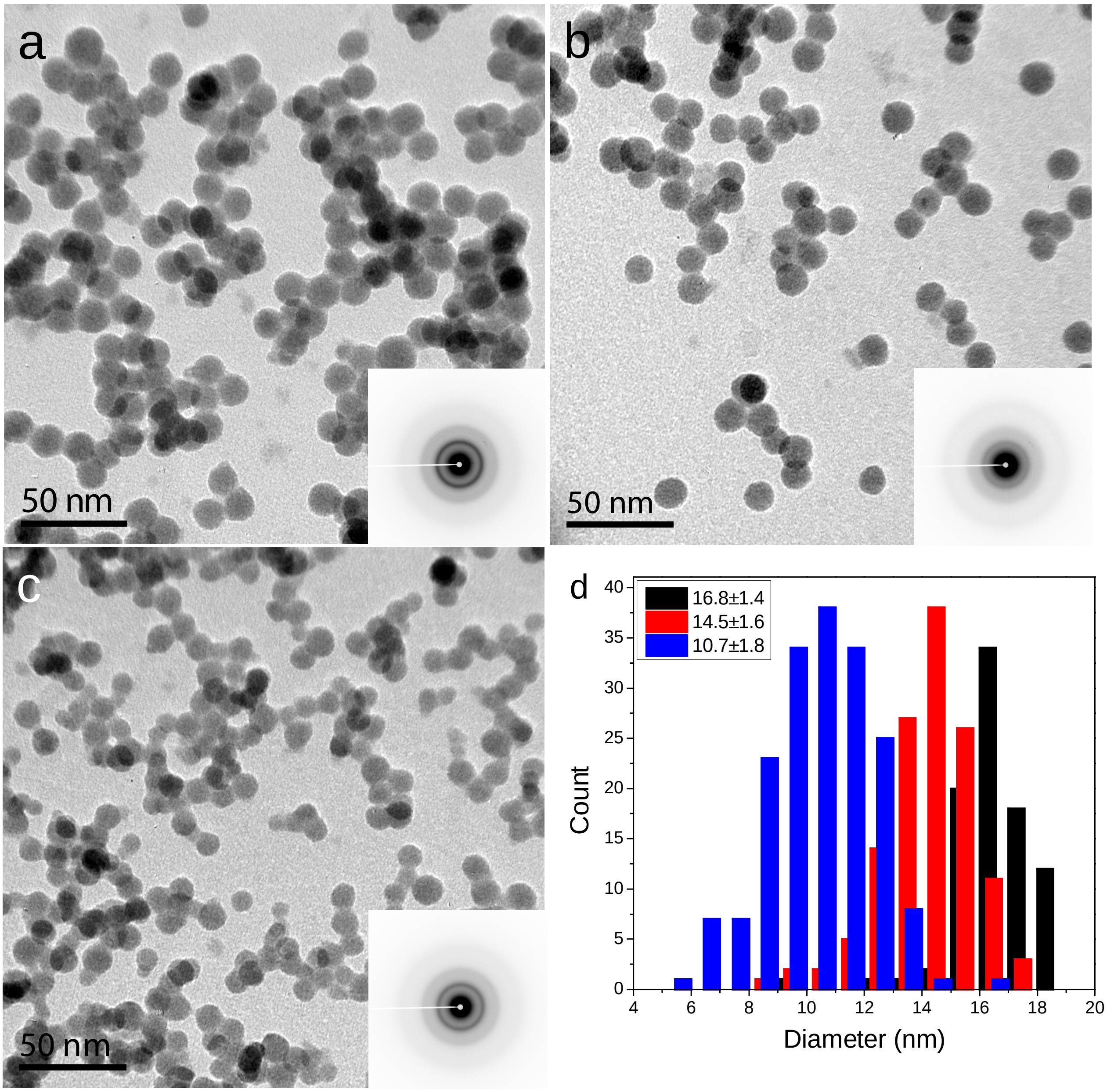

Figure 4.9 TEM images (a-c) showing the morphology of the GST NPs produced with a high amount of methane. The amount of helium used was 0 (a), 10 (b) and 20 (c) sccm. The average diameters of the NPs shown in the three pannels are 16.8±1.4 nm (a), 14.5±1.4 nm (b) and 10.7±1.8 nm (c). (d) Size distributions of the three different samples shown in a-c. Insets SAED patterns in these images a-c indicate the amorphous nature of the NPs.

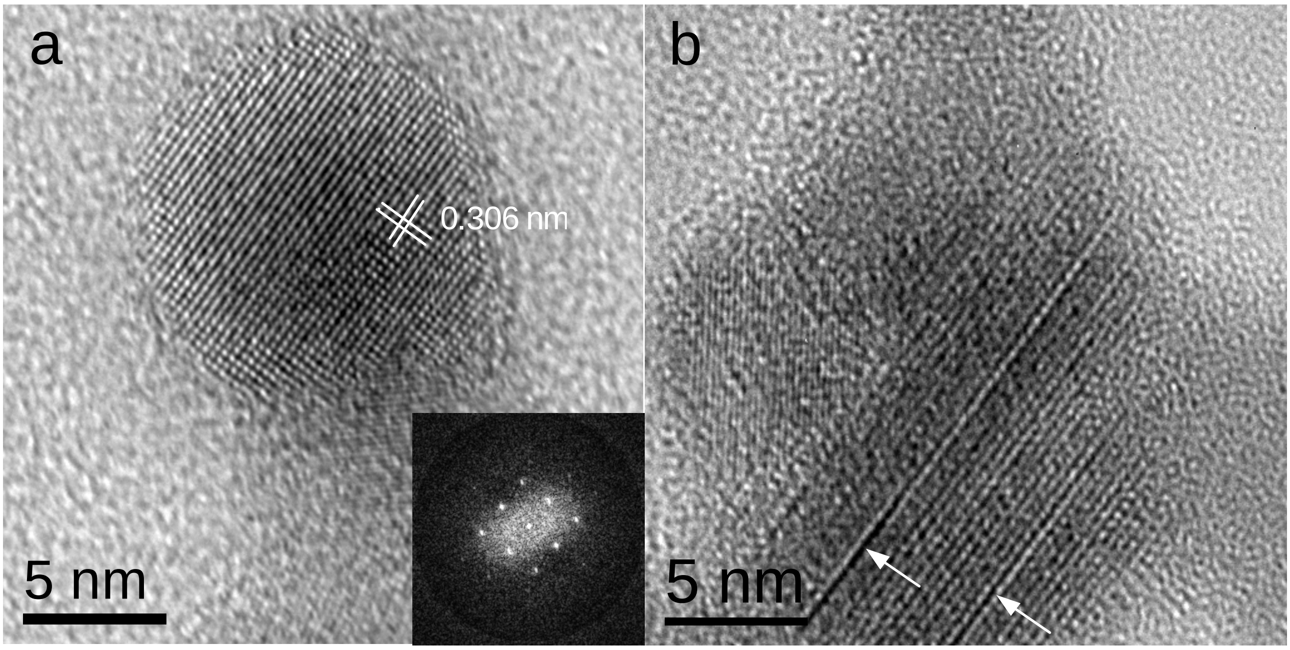

Figure 4.10 HRTEM images showing the FCC and trigonal crystal structures of within GST NPs after heating. (a) HRTEM image shows the rock-salt structure in [100> zone axis with interplannar spacing d_{200}=0.306 nm, suggesting consistent lattice parameter to the one of the as-deposited crystalline NPs. Inset shows the fast Fourier transform of this NP, confirming the rock-salt structure. (b) HRTEM image shows the vacancy layers formed in NPs as indicated by the white arrows. These layers show the onset of the transition from the metastable (rock-salt) to the stable (rhombohedral) phase of GST where initially vacancy layers develop which transform later to Van-der-Waals gaps.

Appendix B

Table 4.1 The crystallization temperatures (T_c) of all the different types of NPs samples analyzed in this chapter.

	Big		**Medium**		**Small**	
	Size (nm)	T_c (°C)	Size (nm)	T_c (°C)	Size (nm)	T_c (°C)
H_2	13.2±1.4	143.8±0.5	10.7±1.7	139.8±0.3	8.4±1.7	138.3±0.6
Low CH_4	15.1±1.4	155.2±0.2	9.8±1.9	149.2±0.6	7.9±1.6	148.8±0.2
High CH_4	16.8±1.4	190.8±1.7	14.5±1.6	183.7±1.1	10.7±1.8	178.4±1

References

(1) Wuttig, M. *Nat. Mater.* **2005**, *4* (4), 265–266.

(2) Wuttig, M.; Yamada, N. *Nat. Mater.* **2007**, *6* (11), 824–832.

(3) Raoux, S.; Welnic, W.; Ielmini, D. *Chem. Rev.* **2010**, *110* (1), 240–267.

(4) Lee, T. H.; Loke, D.; Huang, K.-J.; Wang, W.-J.; Elliott, S. R. *Adv. Mater. Deerfield Beach Fla* **2014**, *26* (44), 7493–7498.

(5) Tuma, T.; Pantazi, A.; Le Gallo, M.; Sebastian, A.; Eleftheriou, E. *Nat. Nanotechnol.* **2016**, *advance online publication*.

(6) Hosseini, P.; Wright, C. D.; Bhaskaran, H. *Nature* **2014**, *511* (7508), 206–211.

(7) Loke, D.; Skelton, J. M.; Wang, W.-J.; Lee, T.-H.; Zhao, R.; Chong, T.-C.; Elliott, S. R. *Proc. Natl. Acad. Sci.* **2014**, *111* (37), 13272–13277.

(8) Rudé, M.; Simpson, R. E.; Quidant, R.; Pruneri, V.; Renger, J. *ACS Photonics* **2015**, *2* (6), 669–674.

(9) Wang, Q.; Rogers, E. T. F.; Gholipour, B.; Wang, C.-M.; Yuan, G.; Teng, J.; Zheludev, N. I. *Nat. Photonics* **2016**, *10* (1), 60–65.

(10) Lee, S.-H.; Jung, Y.; Agarwal, R. *Nat. Nanotechnol.* **2007**, *2* (10), 626–630.

(11) Xiong, F.; Liao, A. D.; Estrada, D.; Pop, E. *Science* **2011**, *332* (6029), 568–570.

(12) Caldwell, M. A.; Raoux, S.; Wang, R. Y.; Wong, H.-S. P.; Milliron, D. J. *J. Mater. Chem.* **2010**, *20* (7), 1285–1291.

(13) Arachchige, I. U.; Soriano, R.; Malliakas, C. D.; Ivanov, S. A.; Kanatzidis, M. G. *Adv. Funct. Mater.* **2011**, *21* (14), 2737–2743.

(14) Polking, M. J.; Urban, J. J.; Milliron, D. J.; Zheng, H.; Chan, E.; Caldwell, M. A.; Raoux, S.; Kisielowski, C. F.; Ager, J. W.; Ramesh, R.; Alivisatos, A. P. *Nano Lett.* **2011**, *11* (3), 1147–1152.

(15) Lee, S.-H.; Jung, Y.; Agarwal, R. *Nano Lett.* **2008**, *8* (10), 3303–3309.

(16) Xiong, F.; Bae, M.-H.; Dai, Y.; Liao, A. D.; Behnam, A.; Carrion, E. A.; Hong, S.; Ielmini, D.; Pop, E. *Nano Lett.* **2013**, *13* (2), 464–469.

(17) Zhang, Y.; Raoux, S.; Krebs, D.; Krupp, L. E.; Topuria, T.; Caldwell, M. A.; Milliron, D. J.; Kellock, A.; Rice, P. M.; Jordan-Sweet, J. L.; Wong, H.-S. P. *J. Appl. Phys.* **2008**, *104* (7), 074312.

(18) Caldwell, M. A.; Jeyasingh, R. G. D.; Wong, H.-S. P.; Milliron, D. J. *Nanoscale* **2012**, *4* (15), 4382.

(19) Choi, H. S.; Seol, K. S.; Takeuchi, K.; Fujita, J.; Ohki, Y. *Jpn. J. Appl. Phys.* **2005**, *44* (10R), 7720.

(20) Park, G.-S.; Kwon, J.-H.; Kim, M.; Yoon, H. R.; Jo, W.; Kim, T. K.; Zuo, J.-M.; Khang, Y. *J. Appl. Phys.* **2007**, *102* (1), 013524.

(21) Kooi, B. J.; Groot, W. M. G.; Hosson, J. T. M. D. *J. Appl. Phys.* **2004**, *95* (3), 924–932.

(22) Gammer, C.; Mangler, C.; Rentenberger, C.; Karnthaler, H. P. *Scr. Mater.* **2010**, *63* (3), 312–315.

(23) Nonaka, T.; Ohbayashi, G.; Toriumi, Y.; Mori, Y.; Hashimoto, H. *Thin Solid Films* **2000**, *370* (1–2), 258–261.

(24) Wuttig, M.; Lüsebrink, D.; Wamwangi, D.; Wełnic, W.; Gilleßen, M.; Dronskowski, R. *Nat. Mater.* **2007**, *6* (2), 122–128.

(25) Ghezzi, G. E.; Morel, R.; Brenac, A.; Boudet, N.; Audier, M.; Fillot, F.; Maitrejean, S.; Hippert, F. *Appl. Phys. Lett.* **2012**, *101* (23), 233113.

(26) Krishnan, G.; Verheijen, M. A.; ten Brink, G. H.; Palasantzas, G.; Kooi, B. J. *Nanoscale* **2013**, *5* (12), 5375.

(27) Peng, C.; Cheng, L.; Mansuripur, M. *J. Appl. Phys.* **1997**, *82* (9), 4183–4191.

(28) Simpson, R. E.; Krbal, M.; Fons, P.; Kolobov, A. V.; Tominaga, J.; Uruga, T.; Tanida, H. *Nano Lett.* **2010**, *10* (2), 414–419.

(29) Lencer, D.; Salinga, M.; Wuttig, M. *Adv. Mater.* **2011**, *23* (18), 2030–2058.

(30) Brink, G. H. ten; Krishnan, G.; Kooi, B. J.; Palasantzas, G. *J. Appl. Phys.* **2014**, *116* (10), 104302.

(31) Park, J.; Kim, M. R.; Choi, W. S.; Seo, H.; Yeon, C. *Jpn. J. Appl. Phys.* **1999**, *38* (8R), 4775.

(32) Friedrich, I.; Weidenhof, V.; Njoroge, W.; Franz, P.; Wuttig, M. *J. Appl. Phys.* **2000**, *87* (9), 4130–4134.

(33) Privitera, S.; Rimini, E.; Bongiorno, C.; Zonca, R.; Pirovano, A.; Bez, R. *J. Appl. Phys.* **2003**, *94* (7), 4409–4413.

(34) Kalb, J.; Spaepen, F.; Wuttig, M. *J. Appl. Phys.* **2003**, *93* (5), 2389–2393.

(35) Wei; Xiaoqian; Shi; Luping; Chong; Chong, T.; Zhao; Rong; Lee; Koon, H. *Jpn. J. Appl. Phys.* **2007**, *46* (4S), 2211.

(36) Orava, J.; Greer, A. L.; Gholipour, B.; Hewak, D. W.; Smith, C. E. *Nat. Mater.* **2012**, *11* (4), 279–283.

(37) Zhou, X.; Wu, L.; Song, Z.; Rao, F.; Zhu, M.; Peng, C.; Yao, D.; Song, S.; Liu, B.; Feng, S. *Appl. Phys. Lett.* **2012**, *101* (14), 142104.

(38) Hirasawa, M.; Orii, T.; Seto, T. *Appl. Phys. Lett.* **2006**, *88* (9), 093119.

(39) Chen, B.; Momand, J.; Vermeulen, P. A.; Kooi, B. J. *Cryst. Growth Des.* **2016**, *16* (1), 242–248.

(40) Reifenberg, J. P.; Panzer, M. A.; Kim, S.; Gibby, A. M.; Zhang, Y.; Wong, S.; Wong, H.-S. P.; Pop, E.; Goodson, K. E. *Appl. Phys. Lett.* **2007**, *91* (11), 111904.

(41) Kolobov, A. V.; Haines, J.; Pradel, A.; Ribes, M.; Fons, P.; Tominaga, J.; Katayama, Y.; Hammouda, T.; Uruga, T. *Phys. Rev. Lett.* **2006**, *97*, 035701.

(42) Kolobov, A. V.; Haines, J.; Pradel, A.; Ribes, M.; Fons, P.; Tominaga, J.; Steimer, C.; Aquilanti, G.; Pascarelli, S. *Appl. Phys. Lett.* **2007**, *91* (2), 021911.

(43) Caravati, S.; Bernasconi, M.; Kühne, T. D.; Krack, M.; Parrinello, M. *Phys. Rev. Lett.* **2009**, *102* (20), 205502.

(44) Sun, Z.; Zhou, J.; Pan, Y.; Song, Z.; Mao, H.-K.; Ahuja, R. *Proc. Natl. Acad. Sci.* **2011**, *108* (26), 10410–10414.

(45) Dick, K.; Dhanasekaran, T.; Zhang, Z.; Meisel, D. *J. Am. Chem. Soc.* **2002**, *124* (10), 2312–2317.

(46) Xiao, S.; Hu, W.; Yang, J. *J. Phys. Chem. B* **2005**, *109* (43), 20339–20342.

(47) Lai, S. L.; Guo, J. Y.; Petrova, V.; Ramanath, G.; Allen, L. H. *Phys. Rev. Lett.* **1996**, *77* (1), 99–102.

(48) Betti Beneventi, G.; Perniola, L.; Sousa, V.; Gourvest, E.; Maitrejean, S.; Bastien, J. C.; Bastard, A.; Hyot, B.; Fargeix, A.; Jahan, C.; Nodin, J. F.; Persico, A.; Fantini, A.; Blachier, D.; Toffoli, A.; Loubriat, S.; Roule, A.; Lhostis, S.; Feldis, H.; Reimbold, G.; Billon, T.; De Salvo, B.; Larcher, L.; Pavan, P.; Bensahel, D.; Mazoyer, P.; Annunziata, R.; Zuliani, P.; Boulanger, F. *Solid-State Electron.* **2011**, *65–66*, 197–204.

(49) Peng, H. K.; Cil, K.; Gokirmak, A.; Bakan, G.; Zhu, Y.; Lai, C. S.; Lam, C. H.; Silva, H. *Thin Solid Films* **2012**, *520* (7), 2976–2978.

Chapter 5

Crystallization Kinetics of GeSbTe Nanoparticles

Abstract

Although nanostructured phase-change materials (PCMs) are considered as the building blocks of next generation phase-change memory and other emerging optoelectronic applications, the kinetics of the crystallization, the central property in switching, remains ambiguous in the high temperature regime. Therefore, we present here an innovative exploration of the crystallization kinetics of $Ge_2Sb_2Te_5$ (GST) nanoparticles (NPs) exploiting differential scanning calorimetry with ultrafast heating up to 40 000 K s^{-1}. Our results demonstrate that the non-Arrhenius thermal dependence of viscosity at high temperature becomes an Arrhenius-like behavior when the glass transition is approached, indicating a fragile-to-strong (FS) crossover in the as-deposited amorphous GST NPs. The overall crystal growth rate of the GST NPs is unraveled as well. This unique feature of the FS crossover is favorable for memory applications as it is correlated to improved data retention. Furthermore, we show that methane incorporation during NP production enhances the stability of the amorphous NP phase (and thereby data retention), while a comparable maximum crystal growth rate is still observed. These results offer deep insight in the crystallization kinetics of nanostructured GST, paving the way for designing non-volatile memories with PCM dimensions below 20 nm.

Based on *Crystallization Kinetics of GeSbTe Phase-Change Nanoparticles Resolved by Ultrafast Calorimetry*, B. Chen, G. ten Brink, G. Palasantzas, B. J. Kooi, *The Journal of Physical Chemistry C* 121.15 (2017): 8569.

5.1 Introduction

$Ge_2Sb_2Te_5$ (GST), one of the prototypical phase-change materials (PCMs), enables rapid and reversible switching between its amorphous and crystalline phases, which is accompanied by large optical and electrical contrast. This unique feature makes GST attractive for data-storage applications [1–3] and a strong contender for emerging applications, such as solid-state displays,[4] optical modulators,[5] neuromorphic computing,[6,7] on-chip photonic circuitry,[8] and plasmonic-based circuits.[9] Crystallization lies at the heart of the switching in phase-change technology, thus a solid understanding of the crystallization kinetics entails a crucial aspect of designing phase-change memory.

Conventional measurements are only able to investigate crystallization kinetics within a relatively low temperature range (near the glass transition temperature).[10–13] However, in actual applications, crystallization generally takes place at higher temperatures. Despite its scientific and technologic relevance, the analysis of the crystallization kinetics at these high temperatures has remained for a long time highly challenging due to the ultrashort time and length scales (ns and nm) involved. This situation persisted until very recently, where ultrafast differential scanning calorimetry (DSC) was utilized to explore the crystallization process of GST films with heating rates up to 40 000 K s^{-1}.[14] Using subsequent extensive modeling, growth rates ranging from the glass transition temperature to the melting temperature were derived for the film structures, showing a remarkable breakdown of Arrhenius behavior in the viscosity at heating rates beyond ~500 K s^{-1}. Non-Arrhenius thermal dependence of the viscosity at high temperatures has lately been widely observed in both nucleation-dominated and growth-dominated PCMs. For instance, for GST confined in memory cells it was demonstrated that non-Arrhenius thermal dependence of crystallization at high temperatures crosses over to a wide temperature range at lower temperatures where still Arrhenius behavior prevails.[15–17] In recent years, also for other PCMs, such as GeTe films,[18] supercooled and melt-quenched AgInSbTe films[19–21] and GeSb films,[22,23] the crystallization kinetics have been determined based on non-conventional techniques with measurements spanning relatively wide temperature ranges. All these works confirm the breakdown of Arrhenius dependence for amorphous PCMs at high temperatures. However, a question that remains is whether this breakdown can be described on the basis of a model for viscosity with a single value for the fragility.

In parallel, down-scaling the GST into (sub-lithographic) nanostructures generates tremendous advantages for PCM-based memory including ultrafast switching, low switching power and ultra-high density. Therefore, many efforts have been devoted to enter this promising field.[24,25] In this context, the fabrication of monodisperse GST nanoparticles (NPs) with good size- and composition-control has been a great challenge for a long time. We achieved a breakthrough by exploiting a technique based on gas-phase condensation and magnetron sputtering, which is capable to meet the requirements of GST NPs fabrication.[26] Size dependent crystallization was observed through *in-situ* heating in a transmission electron microscope. Yet this previous work mainly focused on the crystallization at relatively low temperatures because of the limitation inherent to the *in-situ* TEM heating method. Therefore, the crystallization kinetics of GST NPs remains unknown for the high temperature regime. In this manuscript we present a facile method to synthesize size- and composition-controlled $Ge_2Sb_2Te_5$ nanoparticles via gas-phase condensation, followed by the unprecedented exploration of crystallization kinetics of GST NPs via ultrafast DSC. By varying the heating rate more than three orders of magnitude, the temperature dependent viscosity and growth rate of the crystallization have been unraveled, providing evidence for a fragile-to-strong crossover in as-deposited amorphous GST NPs. Moreover, it is shown that methane addition during NP production is advantageous for application of NPs in PCMs based devices due to the fact that it increases the amorphous phase stability near the glass transition temperature, whereas the maximum switching speed at high temperature is not reduced.

5.2 Experimental methods

5.2.1 GeSbTe nanoparticles synthesis

The $Ge_2Sb_2Te_5$ (GST) nanoparticles (NPs) were directly deposited on a pre-cleaned glass substrate without capping layer. The deposition system is demonstrated in detail in chapter 2. The substrate was put close to the aperture of the aggregation chamber in order to synthesize a large amount of NPs. The main chamber (to collect the NPs) is evacuated to a pressure of 10^{-8} mbar. Amorphous GST NPs were directly synthesized by sputtering the GST target (purity of 99.99%), employing a low current (0.105 A) to avoid the formation of crystalline NPs. The Ar gas flow (purity of 99.9999%) used for the two types of samples analyzed in the present work is 35 sccm, with H_2/CH_4 (purity of 99.99%) as extra gas to facilitate the development of nascent clusters in the plasma. In this chapter, we show the ability of preparing nanoparticles with a large yield that is enough to perform ultrafast heating in DSC. The morphology and stoichiometry were characterized by transmission electron microscope (JEOL 2010) at 200 kV.

5.2.2 Ultrafast differential scanning calorimetry measurement

The phase transitions of the samples were measured by ultrafast DSC. Instead of the loose powder/multi-flakes we used for Ge-Sb PCMs, a single planar flake consisting of GST NPs parallel to the sensor surface was adopted here to run the measurements. The approximate area that was subjected to ultrafast heating is roughly 60×60 μm^2 and 20×20 μm^2 for NPs (H_2) and NPs (CH_4), respectively. This methodology remarkably increases the thermal contact between the materials and the chip sensor. Actually, our results show that all previously published ultrafast DSC work employing loose powder or multi-flakes (of PCMs) can contain erroneous results for the higher heating rate (and thus temperature) regime. The heating rates (Φ) adopted in this manuscript vary from 10 to 40 000 K s^{-1}. The thermal lag of the measurement was evaluated in the Appendix B of this chapter.

5.2.3 Numerical modeling

As described in chapter 2, numerical modeling was adopted to interpret the data obtained by ultrafast DSC. The viscosity model (MYEGA model) we employed successfully for the Ge-Sb alloy turned out inadequate to explain the Arrhenius behavior persisting for such a large temperature range in the Kissinger plot (Figure 5.3) presented in this chapter. Therefore, the generalized MYEGA model was adopted for the fitting.[27] Note that in all the fittings performed in this manuscript, the fractional Stokes-Einstein relation between viscosity and growth rate has been used, with ξ=0.65 suggested by previous work.[14] The details of JMAK modeling can be found in chapter 2. For this JMAK model, descriptions of nucleation and growth are required. For the description of nucleation it is assumed that it is independent of time and temperature, i.e. we assume a constant nuclei density (site saturation), analogous to what was adopted for the modeling of GST films.[14] However, in Figure 5.8 of the Appendix A of this chapter, we show that the results hardly change when we adopt a more intricate steady-state nucleation model. The details of the fitting process in the Kissinger plot can be found in Appendix of chapter 3.

Apart from the ultrafast DSC data presented in the Kissinger plot also two relevant data points, one for GST NPs (H_2) and one for GST NPs (CH_4), were added for very low heating rates Φ (0.03 K s^{-1}) based on our previous in-situ TEM work.[26] The data point for GST NPs (H_2) is reliable, but it is not precise for GST NPs (CH_4). The reason is that it is hard to accurately control for different sample batches the amount of methane incorporated in the gas phase during the NPs sample production. Therefore, this single data point for GST NPs (CH_4) in the Kissinger plot is not used when fitting the JMAK based model to the experimental data.

5.3 Results and Discussion

5.3.1 Morphology and size distribution

Size-dependent crystallization has been observed for $Ge_2Sb_2Te_5$ (GST) nanoparticles (NPs),[26] where the size, morphology, structure and crystallization temperature of the as-deposited NPs have been characterized by transmission electron microscopy (TEM). As shown in Figure 5.1, relatively mono-disperse GST NPs have been synthesized, with average diameters 16.0±1.3 and 16.8±1.7 nm for NPs synthesized with either H_2 or CH_4 added to the base Ar gas, hereafter named NPs (H_2) and NPs (CH_4). Detailed size distributions of these two samples can be found in Figure 5.6 of the Appendix A. The similar sizes and narrow size distribution of the two GST NPs (CH_4) and (H_2) samples exclude size effects on the crystallization observed in the present work. Although the NPs were produced with a relatively high coverage, they are not coalesced but only aggregated, as can be seen clearly in Figure 5.1.

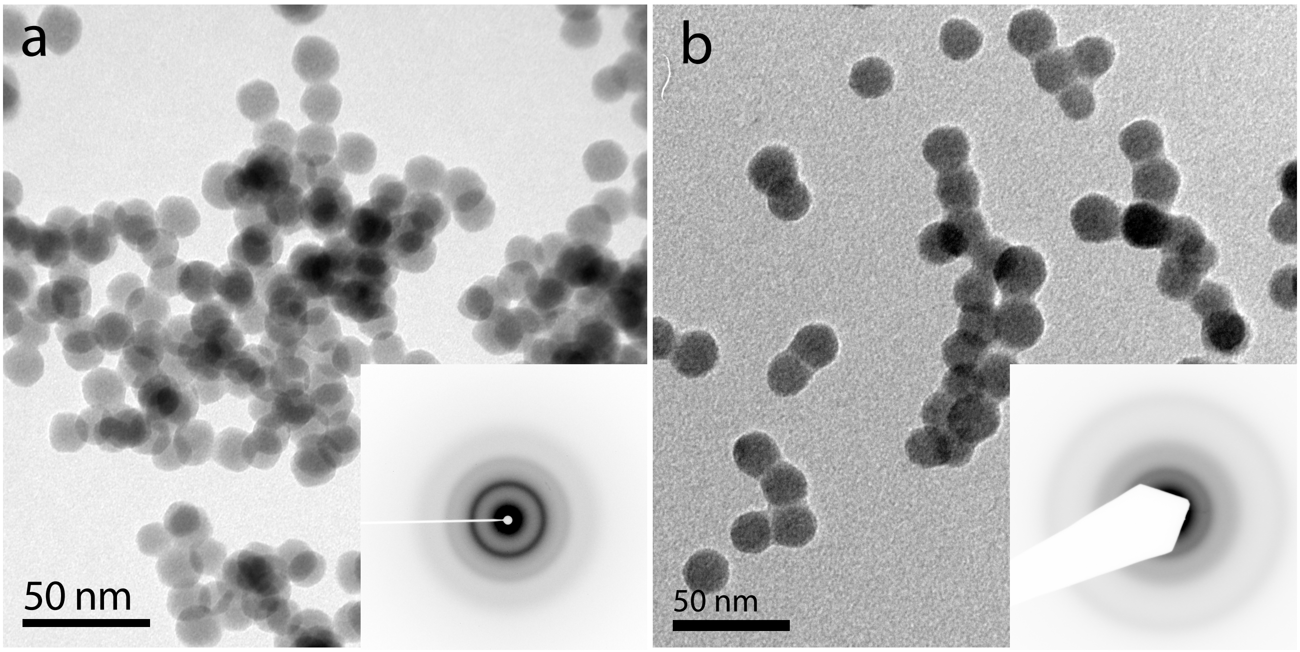

Figure 5.1 Morphology of $Ge_2Sb_2Te_5$ (GST) nanoparticles (NPs). (a), (b) Bright field image of the GST NPs produced with H_2 (NPs (H_2)) and CH_4 (NPs (CH_4)), respectively. The average diameters of the NPs in these two samples are 16.0±1.3 and 16.8±1.7 nm, respectively. Insets show the selected area electron diffraction patterns of the corresponding NPs, clearly demonstrating the amorphous nature of the as-deposited NPs.

The spherical morphology is an indication of the amorphous nature of the NPs, which is further confirmed by selected area electron diffraction (SAED). As manifested by the insets of Figure 5.1, the SAED patterns demonstrate that the NPs are amorphous due to the lack of sharp crystalline rings. The composition of these NPs is Ge:Sb:Te=19:24:57 (±1) at.%, as determined by energy dispersive X-ray spectrometry. Note that the TEM grids were located at the periphery of the NP cluster beam during production, retaining a lower coverage in comparison to the center part. High yield synthesis of GST NPs has been achieved by gas-phase condensation in order to obtain a good signal to noise ratio when performing differential scanning calorimetry (DSC) with ultrafast heating. Moreover, we have demonstrated that the NPs do not coalesce during thermal heating in a transmission electron micscope.[26] Therefore, the above factors enable and ensure the thermal analysis of well-characterized NPs via ultrafast DSC.

5.3.2 Crystallization by ultrafast DSC

The obtained ultrafast DSC traces for the two GST NPs (H_2) and NPs (CH_4) samples are shown in Figure 5.2a-b. The heating rates (Φ) used to obtain the data of the present work vary more than three orders of magnitude, from 10 to 40 000 K s^{-1}. Note that a detectable signal of crystallization only appears for Φ beyond 50 K s^{-1} for the NPs (CH_4). The temperatures for the amorphous to rock-salt transition (T_{p1}) drastically increase when higher Φ are applied to both samples; e.g., T_{p1} of NPs (H_2) shifts from 440 K at 10 K s^{-1} to 542 K at 40 000 K s^{-1}. Figure 5.2 also shows that NPs (CH_4) have an (expected) higher T_{p1} than NPs (H_2), particularly at low Φ. For example, T_{p1} for NPs (CH_4) is ~20 K higher than that of NPs (H_2) at 50 K s^{-1}. In a previous work, we have revealed by *in-situ* heating in a TEM that methane addition during GST NPs production remarkably increase the T_{p1} at relatively low heating rates.[26] Nevertheless, here we observe that this gap of T_{p1} gradually decreases when Φ becomes higher, and finally vanishes when Φ reaches 40 000 K s^{-1}. Surprisingly, at high Φ we observe a big divergence in T_{p1} for GST NPs (H_2) compared to GST films as reported in earlier work.[14] While the T_{p1}'s are very similar at 50 K s^{-1}, the T_{p1} of GST films becomes ~90 K higher than that of the NPs (H_2) at 40 000 K s^{-1}. This gap can (at least partly) stem from two origins: 1) the thermal lag between the thin film and the ultrafast chip sensor, as is discussed in detail in chapter 3. 2) It is still very well likely that the kinetics of NPs differs from that of thin films. We did not have the appropriate thin film samples to verify this and these tests are beyond the scope of the present work, but they are of interest for future research.

Furthermore, the rock-salt to trigonal structural transition is also unambiguously observed for the NPs (H_2) in the ultrafast DSC traces when Φ is above 250 K s^{-1}. The signal of this transition is unexpected but intriguing as it was not detected for GST films via ultrafast DSC measurement in

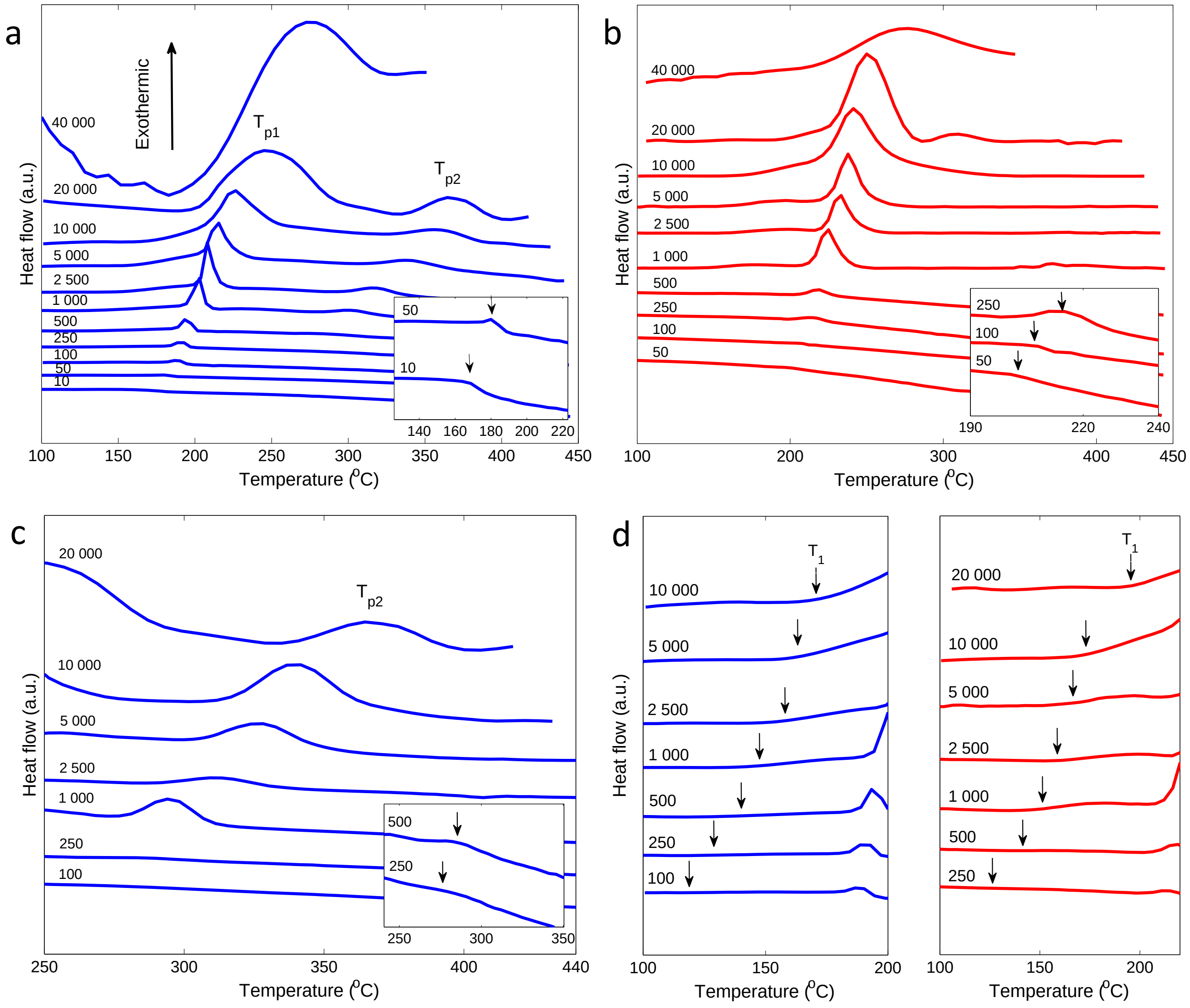

Figure 5.2 Ultrafast DSC traces for GST NPs. (a), (b) Ultrafast DSC traces for GST NPs (H_2) and NPs (CH_4) , respectively, for heating rates (Φ) ranging from 10 to 40 000 K s^{-1}. Insets of (a) and (b) show the close-up of the crystallization peaks at lower Φ . (c) Zoomed-in ultrafast DSC traces of rock-salt to rhombohedral structural transition in NPs (H_2) at Φ ranging from 250 to 20 000 K s^{-1}. (d) Evolution of the structural relaxation temperatures with Φ for NPs (H_2) and NPs (CH_4). The blue and red curves in the figures hold for NPs (H_2) and NPs (CH_4), respectively.

previous work.[14] This transition temperature (denoted hereafter as T_{p2}) displays a clear dependence on Φ as well, where it increases when Φ rises, even with a more drastic increment compared to T_{p1} . Locating at around 553 K at 250 K s^{-1}, T_{p2} moves to 633 K at 20 000 K s^{-1}, as depicted in Figure 5.2c. It is noticeable that T_{p2} is invisible in the DSC signal at the lowest Φ, because of the small heat release involved compared to the amorphous to rock-salt transition. Interestingly, the rock-salt to trigonal structural transition is unobservable in NPs (CH_4) in the present work (as shown in Figure 5.2b). Several explanations could correlate to this feature: i) the addition of methane alters T_{p2} to too high temperature which is beyond the upper limit of ultrafast DSC (450 °C); ii) the incorporation of methane suppresses this structural transition completely; iii) with methane the transition can still occur but with reduced latent heat (or spread over a larger temperature range) such that it is not detected by the ultrafast DSC. More systematic research is necessary before drawing conclusions on this second transition and this is out of the scope of the present work. However, the appearance of this specific transition also indicates good thermal contact between the chip sensor and the NPs flake, as the heat release involved in this transition is much smaller than that of the amorphous to rock-salt transition. The obtained T_{p2} for GST NPs is much lower than that of the GST films due to the expected strong size-dependence of T_{p2}, where it has been observed to reduce sharply with decreasing thickness of GST films.[28]

In the ultrafast DSC traces, a heat release prior to the amorphous to rock-salt transition is also observed, indicated as T_1 in Figure 5.2d. This exothermic heat flow was ascribed to structural relaxation of the amorphous phase by previous researchers,[29] as the temperature is too low for crystallization. For instance, for GST NPs (H_2) at a heating rate of 100 K s^{-1} the temperature T_1 is 120 ^{o}C compared to the crystallization temperature T_{p1} of ~180 ^{o}C. At this T_1 temperature, crystallization only occurs after very long times. For example, for GST nanowires with a width of 60 nm, the amorphous phase can remain present for ~10^6 seconds.[24] Therefore, with high heating rate (100 K/s), the heating process from 25 to 125 ^{o}C takes only 1 second that is way below the time required to start crystallization at 120 ^{o}C. Therefore no signal for crystallization should be observed at these temperatures indicated by the arrows in Figure 5.2d. This structural relaxation has been found in other amorphous materials, such as silicon and germanium, and it is attributed to the presence of a spectrum of activation energies for the sites where relaxation takes place.[30,31] For both the GST NPs (CH_4) and NPs (H_2) samples, T_1 moves towards the onset of the amorphous to rock-salt transition as Φ rises.

5.3.3 Kissinger analysis

To further understand the crystallization kinetics of the NPs, Kissinger analysis is employed. For crystallization, the activation energy can be obtained using the following equation proposed by Kissinger:[32]

$$\frac{Q}{R} = -\frac{d\ln(\Phi / T_p^2)}{d(1/T_p)} \tag{5.1}$$

with Q the activation energy for crystallization, R the gas constant, Φ the heating rate, and T_p the peak temperature in the DSC signal. For a crystallization process complying with Arrhenius behavior, the (constant) activation energy can be derived straightforwardly. Figure 5.3a shows the crystallization data for GST NPs obtained by ultrafast DSC at different Φ, with the blue and red solid circles signifying T_{p1} data for NPs (H_2) and NPs (CH_4), respectively. The single flake methodology (instead of an ensemble of loose flakes) utilized in running the ultrafast heating here effectively improves the thermal contact between the chip sensor and the NPs flake, inducing clearly less scatter in T_{p1} in comparison with the employment of loose powder or multi-flakes. At low Φ, the Arrhenius behavior is maintained, as indicated by the Kissinger plot (Figure 5.3). Surprisingly, the Arrhenius behavior for the NPs persists for a considerably larger Φ range (up to 10 000 K s^{-1}) in contrast to GST films previously studied where Arrhenius behavior was reported to break down already at ~500 K s^{-1},[14] as shown in Figure 5.3a by the black stars. It is also observable that NPs (CH_4) have a higher activation energy for crystallization than NPs (H_2) within the Arrhenius behavior range. The Kissinger plot at lower Φ has been zoomed in and linearly fitted (Figure 5.3b), with an activation energy for crystallization determined as 2.22 and 2.43 eV at^{-1} for NPs (H_2) and NPs (CH_4), respectively. These values coincide well with the reported values for GST films, in a range between 2 and 3 eV by conventional DSC or electrical resistance measurements.[10,33–36] The increase of activation energy induced by CH_4 incorporation is similar to the enhanced activation energy by carbon doping of GST films.[37]

Nevertheless, further increase in Φ (beyond 10 000 K s^{-1}) prompts the breakdown of the Arrhenius behavior, generating a curvature in the Kissinger plot. As a result, the activation energy for crystallization diminishes with the increment of temperature and vanishes at higher temperatures. In order to appropriately interpret these data, Johnson-Mehl-Avrami-Kolmogorov (JMAK) theory has been adopted to fit the Kissinger plot, analogous to our previous work on GeSb alloy.[23] The growth rate of crystallization is vital to utilize the JMAK theory, which can be written as:[19]

$$U(T) = \frac{4r_{atom}k_BT}{3\pi\lambda^2 R_{hyd}\eta(T)^{\xi}}[1-\exp(-\frac{\Delta G(T)}{k_BT})] \tag{5.2}$$

with $U(T)$ the growth rate, r_{atom} the atomic radius (~1.5 Å), λ the diffusional jump distance (~2.99 Å), R_{hyd} the hydrodynamic radius ($R_{hyd} = r_{atom}$), k_B the Boltzmann constant, $\eta(T)$ the temperature dependent viscosity, ξ the decoupling parameter of Stokes-Einstein equation ($\xi \leq 1$) and $\Delta G(T)$ the change of Gibbs free energy, which can be described, according to Thomson and Spaepen, as:[38]

$$\Delta G(T) = \frac{\Delta H_m(T_m - T)}{T_m}\left(\frac{2T}{T_m + T}\right) \tag{5.3}$$

where ΔH_m is the latent heat of melting, approximately 0.152 eV at^{-1},[39] and T_m is set to 890 K.[16] Note that fractional Stokes-Einstein equation ($U \propto \eta^{-\xi}$ with $\xi \leq 1$) is intrinsically included in Equation (5.2), as the breakdown of Stokes-Einstein relation has been observed in a large number of supercooled glass forming liquids and in particular PCMs and it is attributed to dynamical heterogeneities.[14,40] For the GST NPs we set ξ=0.65, a value similar to GST films.[14]

An appropriate viscosity model is required to determine the growth rate in Equation (2). Although the model proposed by *Mauro et al.*[41] (MYEGA model hereinafter) provides, as we proved,[23] a much better description of the viscosity of Ge-Sb phase-change materials as compared to the one from *Cohen & Grest*,[42] it yields inferior fits to the present data for GST NPs owning to its inability to afford Arrhenius behavior in a large temperature range. If the The MYEGA model (with a single fragility value) is adopted, it provides very high values of fragility for the NPs (H_2), *m*=203, which is higher than the theoretical value for kinetic fragility for glass forming liquids (m=176).[43] Furthermore, this model leads to very high crystallization temperatures at low heating rates, resulting in a large mismatch to the data obtained by in-situ heating in TEM, as shown in Figure 5.7 of the Appendix A. Furthermore, for NPs (CH_4), it only fits well at low heating rates range. In contrast, the generalized MYEGA model can avoid all the above problems. Note that the quality of the fits using either the MYEGA model or the *Cohen & Grest* model remains poor even using more sophisticated models for nucleation instead of the simple constant nuclei density (site saturation) adopted initially. Therefore we tested a generalized MYEGA model, since it enabled a successful description of the complex viscosity in metallic glass forming liquids:[27]

$$\log_{10}\eta(T) = \log_{10}\eta(\infty) + \frac{1}{T\left[W_1\exp(-\frac{C_1}{T}) + W_2\exp(-\frac{C_2}{T})\right]} \tag{5.4}$$

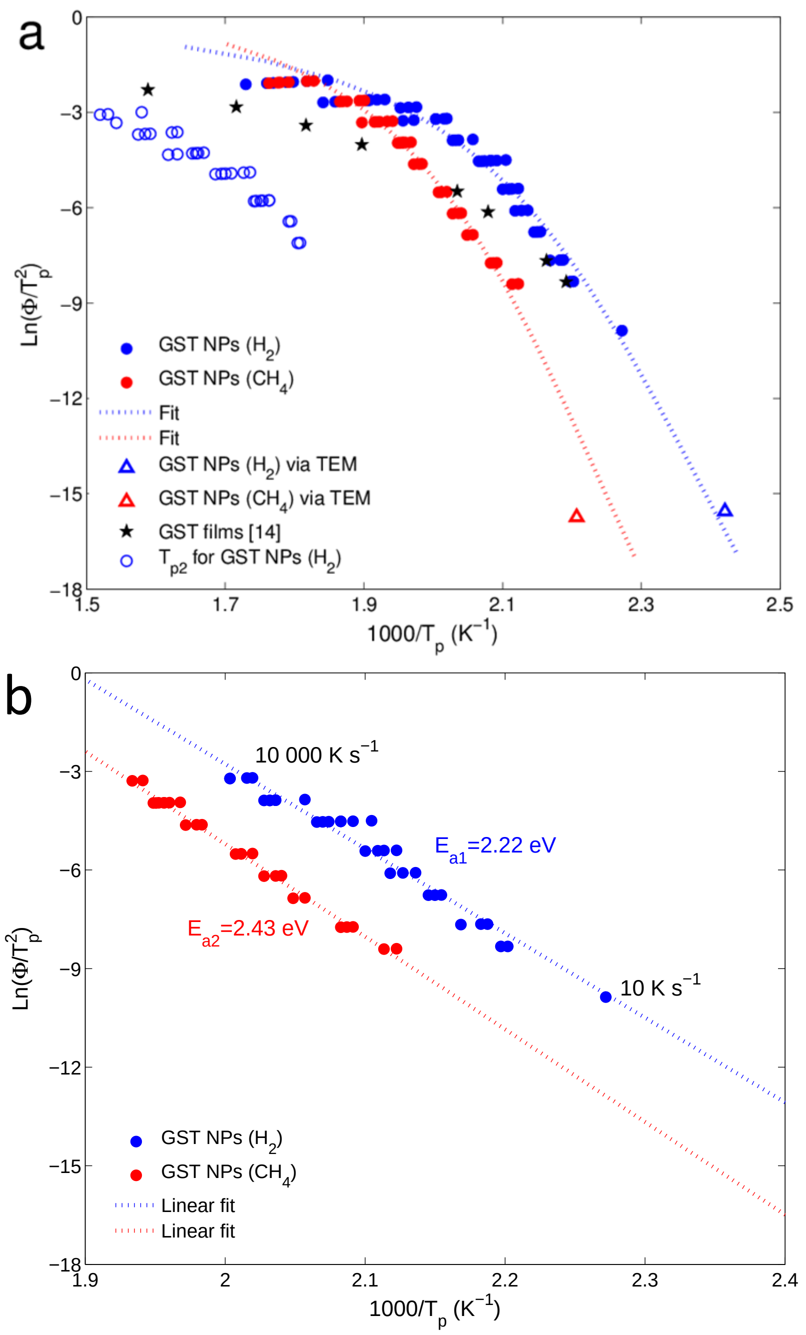

Figure 5.3 Kissinger plot with optimized model fits to the data. (a) Kissinger plot for NPs (H_2) and NPs (CH_4). Blue solid circles and blue open circles denote the amorphous to rock-salt transition temperatures (T_{p1}) and rock-salt to rhombohedral transition temperatures (T_{p2}) of NPs (H_2). The red solid circles represent T_{p1} of NPs (CH_4). Dotted lines show the corresponding fits to these data. The black stars show earlier reported T_{p1} of GST films by ultrafast DSC.[14] The blue and red triangles correspond to the T_{p1} of NPs (H_2) and NPs (CH_4), respectively, as obtained using in-situ heating in the TEM.[26] (b) Linear fit to the Kissinger plot at lower Φ (up to 10 000 K s^{-1}), leading to crystallization activation energy 2.22 and 2.43 eV at^{-1} for NPs (H_2) and NPs (CH_4), respectively.

with $\eta(\infty)$ viscosity at infinite temperature (here it is taken as 10^{-3} Pa s), T the temperature and W_1, C_1, W_2, C_2 the fitting parameters. This model illustrates that two intrinsic terms of viscosity subsist in the liquid, and these two terms can transfer to each other upon cooling or heating. The blue and red dotted curves in Figure 5.3a denote the modeled Kissinger plots utilizing the generalized MYEGA model (Equation (5.4)), showing excellent fits to the corresponding experimental data, with fitting quality evaluated by adjusted R^2 (0.973 and 0.984, respectively). The derived fitting parameters are: W_1=6921.8, C_1=7490.2, W_2=6.63$\times 10^{-4}$, C_2=517.2 for NPs (H_2) and W_1=8259.3, C_1=8091.9, W_2=5.27$\times 10^{-4}$, C_2=510.2 for NPs (CH_4). Note that the data become more scattered when Φ becomes high, particularly for Φ above 10 000 K s^{-1}. Therefore, only three data points at the most right side for Φ beyond 10 000 K s^{-1} are weighted to be the most representative data, as they exemplify the best thermal contact between the chip sensor and the NPs flake.

Moreover, the evolution of T_{p2} with Φ is also depicted in Figure 5.3a. A non-Arrhenius behavior is evidently revealed in this figure, inferring a temperature dependent activation energy for this structural transition. Without a proper growth rate model for this transition, it is currently not possible to model the Kissinger curve via JMAK theory.

5.3.4 Viscosity and fragility of $Ge_2Sb_2Te_5$ nanoparticles

Viscosity is of fundamental and practical relevance for glass forming liquids as it is directly associated with the glass transition and relaxation process, indicating the mobility of the atoms and therefore it is coupled to the growth rate of crystallization. As the unknown parameters in Equation (5.4) have been determined through fitting, the viscosity of the as-deposited amorphous NPs as a function of temperature can be derived straightforwardly; see the red and blue solid curves in the Angell plot of Figure 5.4, where the temperature dependent viscosity of GST films reported previously by *Orava et al.* is also depicted in comparison (black dotted curve in Figure 5.4).[14] Unlike the MYEGA model, Equation (5.4) does not directly provide the value of glass transition temperature (T_g) and fragility. Here we set T_g as the temperature at which the viscosity equals 10^{12} Pa s, then T_g are determined as 373 K and 403 K for NPs (H_2) and NPs (CH_4), respectively. This value for the NPs (H_2) is close to the reported values for the GST films (373~383 K).[14,44] As indicated in a previous work,[26] the crystallization temperature for NPs (H_2) is slightly lower than that of GST films (~10 K), therefore the akin T_g is plausible as the glass transition usually takes place ~10 K lower than T_{p1} at a Φ of 40 K min^{-1} for GST films.[29] The increase of T_g caused by the CH$_4$ incorporation is ~30 K, which agrees excellently with the rise of T_{p1}, as shown here by the ultrafast DSC measurements and by the *in-situ* TEM characterization of our earlier work.[26] The fragility, defined as $m = \left.\frac{d(\log_{10}\eta(T))}{d(T_g/T)}\right|_{T=T_g}$, is determined from the Angell plot for these NPs as well. The fragility of NPs (H$_2$) is 57, consistent with the value from a previous work (m=47 for non-doped GST films).[45] Methane addition slightly increases the fragility to a value of 62. These values for fragility are considerably lower compared to the value obtained earlier for GST films (m=90).[14]

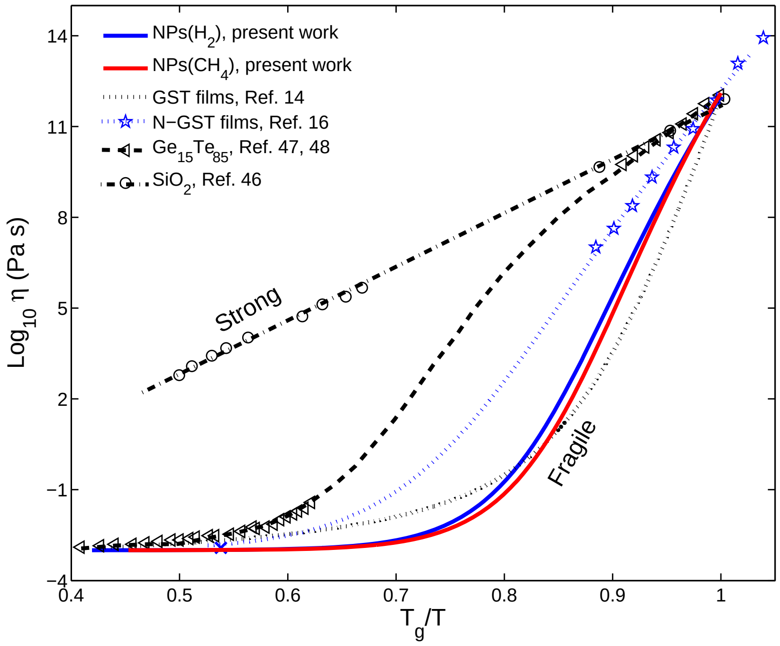

Figure 5.4 Angell plot for viscosity. The blue and red solid curves represent the modeled viscosity for NPs (H$_2$) and NPs (CH$_4$), respectively. The black open circles are the viscosity data for SiO$_2$ in order to show a strong (undercooled) liquid.[46] The black open triangles and the corresponding fitting curve are the experimental data[47,48] and fitting curve utilizing Equation (5.4) for Ge$_{15}$Te$_{85}$. The blue stars are the viscosity data for nitrogen doped GST films,[16] with corresponding fitting curves adopting Equation (5.4). Black dotted curve shows the viscosity for GST films explored by ultrafast DSC.[14]

5.3.5 Fragile-to-strong crossover

In the Angell plot, an Arrhenius behavior resulting in a fragility approaching ~15, such as holds for SiO$_2$,[46] is categorized as a strong (supercooled) liquid (cf. Figure 5.4). Larger values of fragility lead to non-Arrhenius behavior, classified as fragile, such as has been presented for the GST films.[14] However, in some (undercooled) liquids a single fragility model is not able to describe the temperature dependence of viscosity. Then, the coexistence of Arrhenius behavior at low temperature and non-Arrhenius behavior at high temperature has been successfully explained by a fragile-to-strong (FS) crossover,[27] which is a ubiquitous feature in glass formers. First discovered in water,[49] this phenomenon has thereafter been observed in glass forming liquids,[27] chalcogenides[50,51] and Ag-In-Sb-Te PCMs.[20] For instance, Figure 5.4 portrays the experimental viscosity data for $Ge_{15}Te_{85}$ (black open triangles) at temperatures near T_g[48] and melting temperature (T_m),[47] fitted with the corresponding dash curve utilizing Equation (4), where a distinct FS crossover is illustrated. The FS crossover in $Ge_{15}Te_{85}$ is confirmed by another work employing the Adam-Gibbs equation to fit the viscosity.[51] For GST NPs, the FS crossover is likewise discerned, demonstrated by the red and blue solid curves in Figure 5.4. With the strong segment near T_g , the viscosity drops exponentially with the increment of temperature with an intermediate fragility (strong), whereas a further increase in temperature yields a non-exponential decline of viscosity (fragile). The FS crossover in GST NPs is weaker than that of $Ge_{15}Te_{85}$, where the two segments of viscosity are clearly distinguished. Still, as we explain in the next paragraph, there are strong arguments that the FS crossover actually occurs in GST NPs and that it is not a misinterpretation of a (more ordinary) glass transition.

A similar temperature dependence of the growth rate as in the present work was also observed for AgInSbTe PCMs, where the Arrhenius dependence of viscosity was found at lower temperatures, while the MYEGA model (non-Arrhenius dependence) was obtained at higher temperatures.[19,21] At that time it was proposed that the Arrhenius behavior correlates to the glassy state whereas the non-Arrhenius behavior is associated with the supercooled liquid state. In this scenario, this divergence in temperature dependence of viscosity appears at the junction between glass and supercooled liquid. If our observed (FS transition) behavior is explained as a glass transition, that would lead to a T_g of ~438 K for GST NPs (H_2). Taking this value for T_g, we then obtain a viscosity at T_g of 10^3 Pa s. It is obvious that this viscosity is in conflict with the definition of glass transition temperature (where the viscosity is 10^{12} Pa s). Moreover, we also observed crystallization at a temperature about 20 K lower than this supposed T_g of ~438 K,[26] which is also inconsistent with the notation that crystallization is only possible above T_g. Clearly, with the fragile-to-strong crossover model, these conflicts are avoided. Therefore, the FS crossover is a more plausible explanation of our observations than the (supercooled liquid to) glass transition.

The present results therefore show the presence of the FS crossover, which already was signified by the large Arrhenius region shown in Figure 5.3b. It occurs for both samples approximately at 0.85 T_g/T, a T_g-scaled temperature lower than that of $Ge_{15}Te_{85}$ and AgInSbTe.[20] The CH_4 addition has negligible influence on this crossover. For GST films reported by *Orava et al.*, however, the FS crossover was not observed and a viscosity model with a single fragility value (Cohen&Grest model) was adopted to fit the Kissinger plot obtained through ultrafast DSC,[14] denoted as the black dotted curve in Figure 5.4. The high fragility of GST films results in a sharp reduction of viscosity at temperatures just above T_g. Yet, the lower fragility for GST NPs, caused by the FS crossover, yields a less acute decline in viscosity. Consequently, the GST NPs exhibit a higher viscosity at lower temperature in comparison to the GST films, as distinguished at ~0.9-1 T_g/T in Figure 5.4. These results thus suggest that NPs are advantageous in phase-change memory as higher viscosity correlates to lower atomic diffusivity therefore longer data retention time.

In a previous work,[16] the growth rate of nitrogen doped GST (N-GST) in memory cells was directly measured in a large temperature regime (from ~420 to ~530 K), where the overall growth rate of the N-GST deviates in temperature dependence: Arrhenius behavior at low temperature and non-Arrhenius behavior at high temperature. The experimental data for growth rate were transposed to viscosity using Equation (5.2), with decoupling parameter ξ=0.72 and other parameters (viz. T_m, r_{atom}, λ and R_{hyd} in Equation (5.2)) from this article. ξ is adjusted to make $\eta(T_g)=10^{12}$ Pa s, and this value of ξ is close to that for GST films reported previously.[14] The transposed viscosity is presented as blue stars in Figure 5.4. The MYEGA model for viscosity with one fragility cannot fit these data when specifying $\eta(T_m)$ as 1.2×10^{-3} Pa s.[52] In contrast, the generalized MYEGA model (Equation (5.4)) yields a good fit to the viscosity of N-GST, providing a strong indication that the FS crossover also occurs in these N-doped GST films employed in memory cells. In another work,[17] a similar temperature dependence in the growth rate of GST is observed, and two terms of temperature dependence were utilized to fit the Kissinger plot for GST confined in a memory cell. Yet, the FS crossover was not proposed to explain the observed behavior, but in the light of the present work it has thus been generally observed for GST in memory cells.

It has been suggested that FS crossover exists only in growth-dominated PCMs, but not in nucleation-dominated PCMs.[53] Melt-quenched GST PCMs confined in a cell are considered (by their nanoscale volume) as growth-dominated PCMs.[17] While GST films are considered as nucleation-dominated PCMs, GST NPs, on the other hand also possess growth-dominated crystallization ascribed to the extremely small volume for crystallization caused by down-scaling. For instance, in our previous work we found by high resolution TEM only single crystalline NPs.[26] Nevertheless, small crystal domains are generally expected for surface-induced heterogeneous nucleation dominated crystallization of GST PCMs.[54] However, the NPs in the present work are apparently that small that they still form single crystals. Therefore, it might be possible that presence of the FS crossover in GST NPs compared to its absence in GST films can be attributed to the down-scaling induced change in crystallization mechanism from nucleation dominant to growth dominant.

5.3.6 Overall growth rate of $Ge_2Sb_2Te_5$ nanoparticles

The overall growth rate of the crystallization for the GST NPs is of technological relevance, e.g. for PC memories, as it is associated with data retention at the lower temperatures and the switching speed at higher temperatures. The blue and red solid curves in Figure 5.5 show the overall growth rate, as derived using Equation 5.2, ranging from T_g to T_m for both NPs (H_2) and NPs (CH_4), respectively. In comparison, the growth rate of GST films obtained by *Orava et al.* is also depicted as black dash curve in Figure 5.5.[14] The maximum growth rate (U_m) for these 2 types of NPs is very similar, 1.7 and 1.6 m s^{-1}, with U_m taking place at approximately 0.7 T/T_m. These values for NPs are reasonably close to U_m of GST films, as can be observed in Figure 5.5 by comparing the blue and red solid curves for the GST NPs with the black dash curve holding for GST films. In a previous work, the growth rate of Ge-Sb alloy reaches maximum value at ~0.9 T/T_m,[23] which is plausible, because the U_m of growth-dominated PCMs is considered to occur at a higher T/T_m compared to nucleation-dominated PCMs.[20]

Although the NPs (CH_4) possess a lower growth rate at lower temperature range (below 520 K), it coincides with the one for NPs (H_2) when the temperature is beyond 590 K. The lower growth rate for NPs (CH_4) at low temperature is similar to the retardation induced by carbon doping in GST films,[37] as carbon (a byproduct decomposed from methane in plasmas) is expected to be incorporated into the NPs. When the temperature becomes higher, the FS crossover appears and then the fragile regime of viscosity is accessed. As a consequence, the viscosity strongly drops to equivalent values generating final convergence of the growth rates. This trend is also indicated by the viscosity in Figure 5.4, where the difference is less apparent, because Figure 5.4 is normalized with respect to T_g. This makes the NPs (CH_4) preferable for PC memory application as lower growth rates at low temperatures associated with a higher activation energy indicates a longer data retention time, meanwhile the still comparable growth rates at higher temperature enable sufficient rapid switching (to the crystalline SET state); see Figure 5.9.

The growth rate undergoes an Arrhenius-like behavior at temperatures just above T_g, and non-Arrhenius behavior emerges with a further increase of temperature, demonstrating a temperature dependent activation energy (E_g, derived from the gradient of this curve) for crystal growth during crystallization. With similar slopes to the independent data near T_g, the E_g is determined as ~2.8 and ~3.2 eV at^{-1} for the NPs(H_2) and NPs (CH_4). For $Ge_2Sb_2Te_5$ films it is well-established that the activation energy for crystallization and for growth near T_g is in the range 2.2 – 3.0 eV at^{-1}.[10–13,36,55] In comparison, the growth rate of GST films derived in Ref. 14 presents a considerably higher activation energy, ~5.0 eV at^{-1} near T_g, which appears unrealistic. Although a high fragility of the GST thin film can lead to a high activation energy, this fragility was obtained fully through modelling and fitting and not based on any directly measured data, inferring that the high fragility for the thin film could be erroneous.

However, it is still evident that the growth rates for the NPs (H_2) observed in the present work exhibit a large gap (~2 orders of magnitude) with the directly measured data obtained for GST films (open black data points in Figure 5.5).[11–13] This discrepancy can have several origins, e.g.: 1) The NPs (H_2) crystallize at lower temperature than films, leading to a faster growth rate at the same temperature. The NPs (CH_4) represent an evidently lower growth rate at the same temperature compared to NPs (H_2) due to the increase of T_p. Similarly, the nitrogen doped GST films (confined in memory cells) even show smaller growth rate than GST films,[16] as demonstrated by the blue stars in Figure 5.5; 2) The constant nuclei density hypothesis that was adopted in JMAK modeling is oversimplified and may result in an erroneous fitting of the data in the Kissinger plot and therefore may cause a considerable shift to higher growth rates at the lower temperatures. However, several clearly more advanced models for nucleation were also tested and these models did not significantly reduce the gap between the growth rates derived for the NPs (H_2) (blue solid line in Figure 5.5) and the directly measured data obtained for GST films (black open data points in Figure5); for more details see Figure 5.8 of the Appendix A.

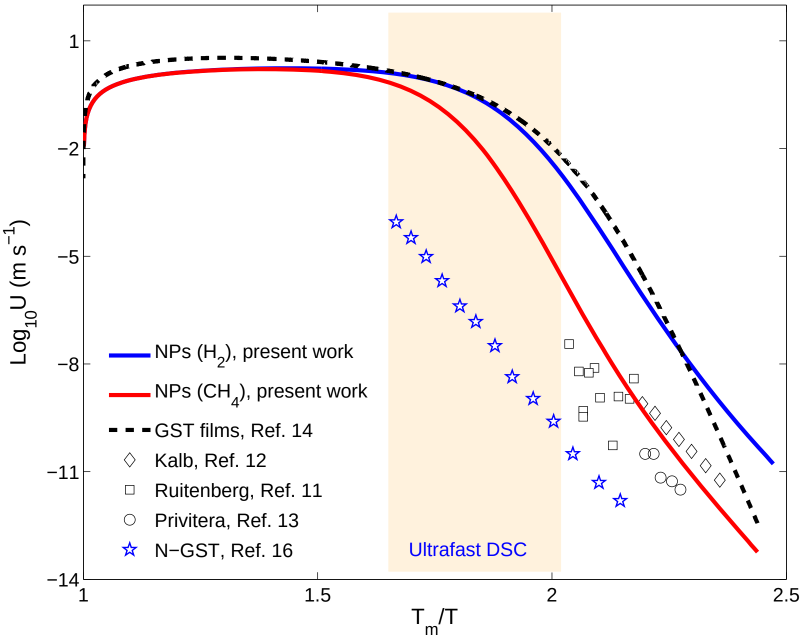

Figure 5.5 The growth rates of GST NPs between T_g and T_m. Blue and red curves represent the data for GST (H_2) and GST (CH_4), respectively. The black dash curve is the growth rate for GST films,[14] while the black data points are from direct measurements via transmission electron microscope,[11,13] and atomic force microscopy.[12] The directly measured growth rate for nitrogen doped GST films is also shown in this figure;[16] see the blue stars in this figure. The light yellow shaded area denotes the actual measurement regime accessed by ultrafast DSC.

5.4 Conclusions

Ultrafast differential scanning calorimetry has been employed to investigate the crystallization kinetics of $Ge_2Sb_2Te_5$ phase-change nanoparticles (NPs) synthesized by gas-phase condensation. The NPs show a relatively narrow size distribution around an average diameter of ~16 nm. Varying the heating rate during the DSC measurements with three orders of magnitude, it is observed that: (1) the crystallization rate complies with Arrhenius behavior within an (unexpectedly) large temperature range directly above T_g (for T_g/T values from 0.85-1), and (2) a non-Arrhenius fragile behavior occurs at higher temperatures (for T_g/T values lower than 0.85). This unique feature can be explained well (only) by utilizing a fragile-to-strong crossover model for the viscosity, from which the overall viscosity and growth rate of the NPs have been derived. This crossover is clearly observed here for the $Ge_2Sb_2Te_5$ NPs, while it was not observed earlier for GST films. This enables NPs to have both longer data retention times at low temperatures and high switching speed at high temperatures, entailing the NPs to be an advantageous contender in phase-change materials based devices. Moreover, it is demonstrated that CH_4 incorporation during the NPs production reduces the crystal growth rate by about two orders of magnitude at lower temperatures, and thus improves the data retention, whereas the maximum growth rate remains unchanged. This positive *"doping"* effect makes $Ge_2Sb_2Te_5$ NPs even more suitable candidates for phase-change memory applications.

Appendix A

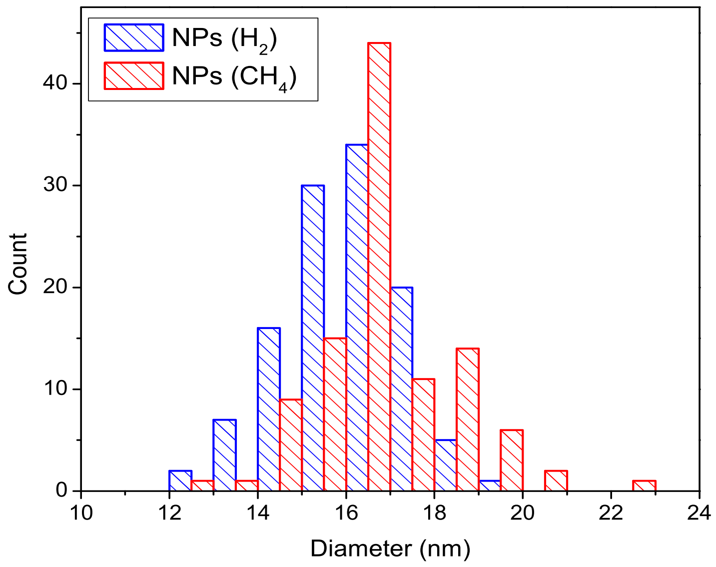

Figure 5.6 The size distribution of the $Ge_2Sb_2Te_5$ (GST) nanoparticles (NPs) synthesized with H_2 (black) and CH_4 (red) as derived from TEM images. The average diameters of these two samples are 16.0±1.3 and 16.8±1.7 nm, respectively. The NPs size distribution is relatively mono-disperse.

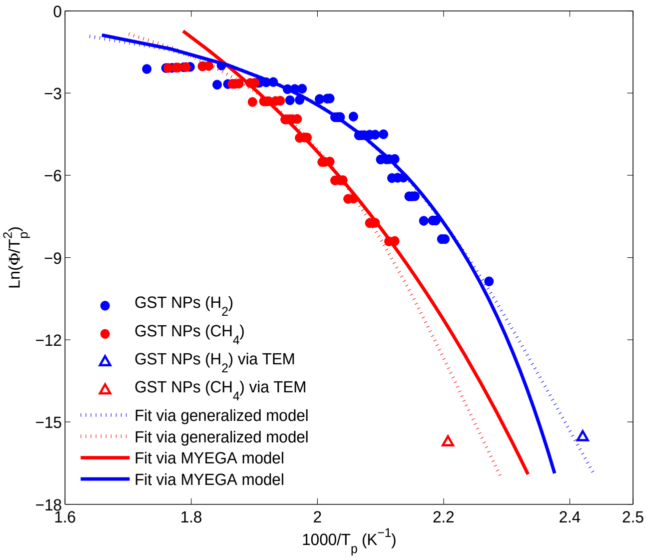

Figure 5.7 Fit of Kissinger plot utilizing the MYEGA model. Red and blue solid curves denote the inferior fits to the data via MYEGA model for viscosity for NPs (H_2) and NPs (CH_4), respectively. In contrast, the generalized MYEGA model shows much better fits for the whole temperature range.

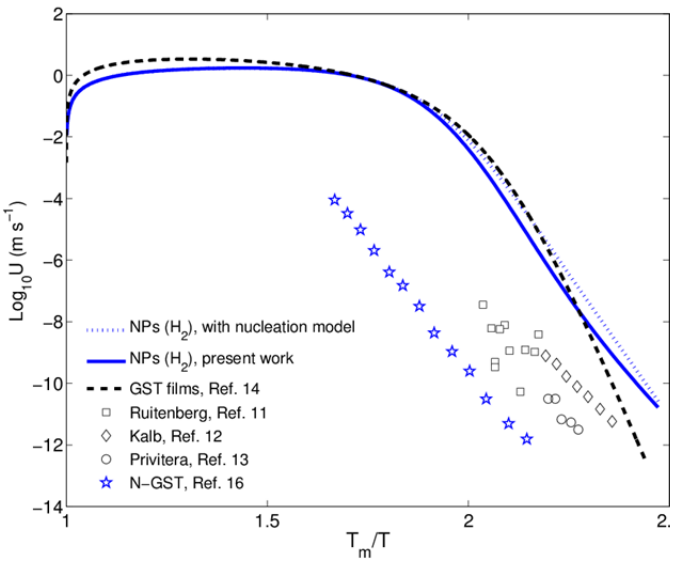

Figure 5.8 Overall growth rate of GST NPs (H_2) as a function of temperature using two models for nucleation. In the present work as in the previous work on GST films a very simple model for nucleation is adopted: constant nuclei density (independent of time and temperature). In order to test whether the results are sensitive to changing the nucleation model also a more intricate model has been tested including time- and temperature-dependent nucleation. The result shown by the blue dotted curve yields a similar growth rate at lower temperature side to the one with constant nucleation density (blue solid curve). Therefore, the present results show that the gap between the measured [11–13,16] and the modelled data is not caused by the model that is adopted for the nucleation.

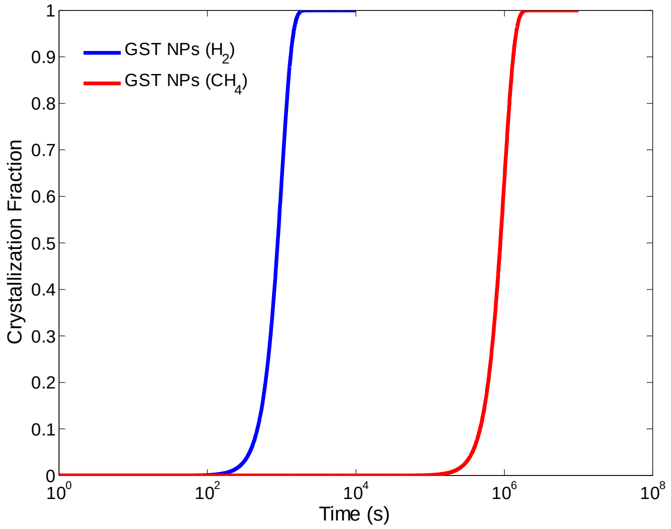

Figure 5.9 Modeled isothermal crystallization curve as a function of time at 110 °C. It can be nicely observed that the incubation time for crystallization becomes several orders of magnitude longer in case of GST NPs (CH_4) than in case of GST NPs (H_2).

Appendix B

Thermal lag

The theory to estimate thermal lag has been detailed in the Appendix of chapter 3. Taking the values for heat transfer coefficient (5 to 20 kW m^{-2} K^{-1}), sample thickness (200 to 500 nm) and thermal conductivity (0.19 W m^{-1} K^{-1} at 20 ^{o}C)[56] for $Ge_2Sb_2Te_5$ thin films, the Boit number is then derived in the range 0.005 to 0.05 according to Equation 3.8, indicating that the assumption of a uniform temperature distribution within the sample is reasonable.

Taking the heat capacity of $Ge_2Sb_2Te_5$ thin films as 1.4×10^6 J m^{-3} K^{-1},[39] the thermal lag caused by the heat transfer between the chip sensor and the sample is determined in the range 0.5 to 6 K at the maximum heating rate 40 000 K s^{-1} according to Equation 3.9. This thermal lag will not affect the breakdown of the Arrhenius behavior, since the breakdown starts at 10 000 K s^{-1}.

References

(1) Wuttig, M. *Nat. Mater.* **2005**, *4* (4), 265–266.

(2) Wuttig, M.; Yamada, N. *Nat. Mater.* **2007**, *6* (11), 824–832.

(3) Raoux, S.; Welnic, W.; Ielmini, D. *Chem. Rev.* **2010**, *110* (1), 240–267.

(4) Hosseini, P.; Wright, C. D.; Bhaskaran, H. *Nature* **2014**, *511* (7508), 206–211.

(5) Waldecker, L.; Miller, T. A.; Rudé, M.; Bertoni, R.; Osmond, J.; Pruneri, V.; Simpson, R. E.; Ernstorfer, R.; Wall, S. *Nat. Mater.* **2015**, *14* (10), 991–995.

(6) Burr, G. W.; Shelby, R. M.; Sidler, S.; Nolfo, C. di; Jang, J.; Boybat, I.; Shenoy, R. S.; Narayanan, P.; Virwani, K.; Giacometti, E. U.; Kurdi, B. N.; Hwang, H. *IEEE Trans. Electron Devices* **2015**, *62* (11), 3498–3507.

(7) Tuma, T.; Pantazi, A.; Le Gallo, M.; Sebastian, A.; Eleftheriou, E. *Nat. Nanotechnol.* **2016**, *advance online publication*.

(8) Ríos, C.; Stegmaier, M.; Hosseini, P.; Wang, D.; Scherer, T.; Wright, C. D.; Bhaskaran, H.; Pernice, W. H. P. *Nat. Photonics* **2015**, *9* (11), 725–732.

(9) Rudé, M.; Simpson, R. E.; Quidant, R.; Pruneri, V.; Renger, J. *ACS Photonics* **2015**, *2* (6), 669–674.

(10) Friedrich, I.; Weidenhof, V.; Njoroge, W.; Franz, P.; Wuttig, M. *J. Appl. Phys.* **2000**, *87* (9), 4130–4134.

(11) Ruitenberg, G.; Petford-Long, A. K.; Doole, R. C. *J. Appl. Phys.* **2002**, *92* (6), 3116–3123.

(12) Kalb, J.; Spaepen, F.; Wuttig, M. *Appl. Phys. Lett.* **2004**, *84* (25), 5240–5242.

(13) Privitera, S.; Bongiorno, C.; Rimini, E.; Zonca, R. *Appl. Phys. Lett.* **2004**, *84* (22), 4448–4450.

(14) Orava, J.; Greer, A. L.; Gholipour, B.; Hewak, D. W.; Smith, C. E. *Nat. Mater.* **2012**, *11* (4), 279–283.

(15) Ciocchini, N.; Cassinerio, M.; Fugazza, D.; Ielmini, D. *IEEE Trans. Electron Devices* **2013**, *60* (11), 3767–3774.

(16) Sebastian, A.; Le Gallo, M.; Krebs, D. *Nat. Commun.* **2014**, *5*.

(17) Jeyasingh, R.; Fong, S. W.; Lee, J.; Li, Z.; Chang, K.-W.; Mantegazza, D.; Asheghi, M.; Goodson, K. E.; Wong, H.-S. P. *Nano Lett.* **2014**, *14* (6), 3419–3426.

(18) Santala, M. K.; Reed, B. W.; Raoux, S.; Topuria, T.; LaGrange, T.; Campbell, G. H. *Appl. Phys. Lett.* **2013**, *102* (17), 174105.

(19) Salinga, M.; Carria, E.; Kaldenbach, A.; Bornhöfft, M.; Benke, J.; Mayer, J.; Wuttig, M. *Nat. Commun.* **2013**, *4*.

(20) Orava, J.; Hewak, D. W.; Greer, A. L. *Adv. Funct. Mater.* **2015**, *25* (30), 4851–4858.

(21) Zalden, P.; von Hoegen, A.; Landreman, P.; Wuttig, M.; Lindenberg, A. M. *Chem. Mater.* **2015**, *27* (16), 5641–5646.

(22) Eising, G.; Van Damme, T.; Kooi, B. J. *Cryst. Growth Des.* **2014**, *14* (7), 3392–3397.

(23) Chen, B.; Momand, J.; Vermeulen, P. A.; Kooi, B. J. *Cryst. Growth Des.* **2016**, *16* (1), 242–248.

(24) Lee, S.-H.; Jung, Y.; Agarwal, R. *Nat. Nanotechnol.* **2007**, *2* (10), 626–630.

(25) Xiong, F.; Liao, A. D.; Estrada, D.; Pop, E. *Science* **2011**, *332* (6029), 568–570.

(26) Chen, B.; ten Brink, G. H.; Palasantzas, G.; Kooi, B. J. *Sci. Rep.* **2016**, 6, 39546.

(27) Zhang, C.; Hu, L.; Yue, Y.; Mauro, J. C. *J. Chem. Phys.* **2010**, *133* (1), 014508.

(28) Wei, X.; Shi, L.; Chong; Chong, T.; Zhao, R.; Lee, K. H. *Jpn. J. Appl. Phys.* **2007**, *46* (4S), 2211.

(29) Kalb, J. a.; Wuttig, M.; Spaepen, F. *J. Mater. Res.* **2007**, *22* (03), 748–754.

(30) Roorda, S.; Doorn, S.; Sinke, W. C.; Scholte, P. M. L. O.; van Loenen, E. *Phys. Rev. Lett.* **1989**, *62* (16), 1880–1883.

(31) Donovan, E. P.; Spaepen, F.; Turnbull, D.; Poate, J. M.; Jacobson, D. C. *J. Appl. Phys.* **1985**, *57* (6), 1795–1804.

(32) Kissinger, H. E. *Anal. Chem.* **1957**, *29* (11), 1702–1706.

(33) Yamada, N.; Ohno, E.; Nishiuchi, K.; Akahira, N.; Takao, M. *J. Appl. Phys.* **1991**, *69* (5), 2849–2856.

(34) Ohshima, N. *J. Appl. Phys.* **1996**, *79* (11), 8357–8363.

(35) Kim, Y.; Park, S. A.; Baeck, J. H.; Noh, M. K.; Jeong, K.; Cho, M.-H.; Park, H. M.; Lee, M. K.; Jeong, E. J.; Ko, D.-H.; Shin, H. J. *J. Vac. Sci. Technol. A* **2006**, *24* (4), 929–933.

(36) Tominaga, J.; Shima, T.; Fons, P.; Simpson, R.; Kuwahara, M.; Kolobov, A. *Jpn. J. Appl. Phys.* **2009**, *48* (3S1), 03A053.

(37) Zhou, X.; Wu, L.; Song, Z.; Rao, F.; Zhu, M.; Peng, C.; Yao, D.; Song, S.; Liu, B.; Feng, S. *Appl. Phys. Lett.* **2012**, *101* (14), 142104.

(38) Thompson, C. V.; Spaepen, F. *Acta Metall.* **1979**, *27* (12), 1855–1859.

(39) Kalb, J. A.; Wuttig, M. Publikationsserver der RWTH Aachen University 2006.

(40) Ediger, M. D. *Annu. Rev. Phys. Chem.* **2000**, *51* (1), 99–128.

(41) Mauro, J. C.; Yue, Y.; Ellison, A. J.; Gupta, P. K.; Allan, D. C. *Proc. Natl. Acad. Sci.* **2009**, *106* (47), 19780–19784.

(42) Cohen, M. H.; Grest, G. S. *Phys. Rev. B* **1979**, *20* (3), 1077–1098.

(43) Wang, L.-M.; Mauro, J. C. *J. Chem. Phys.* **2011**, *134* (4), 044522.

(44) Morales-Sánchez, E.; Prokhorov, E. F.; Mendoza-Galván, A.; González-Hernández, J. *J. Appl. Phys.* **2002**, *91* (2), 697–702.

(45) Cho, J.-Y.; Kim, D.; Park, Y.-J.; Yang, T.-Y.; Lee, Y.-Y.; Joo, Y.-C. *Acta Mater.* **2015**, *94*, 143–151.

(46) Angell, C. A. *Science* **1995**, *267* (5206), 1924–1935.

(47) Neumann, H.; Herwig, F.; Hoyer, W. *J. Non-Cryst. Solids* **1996**, *205–207*, *Part 1*, 438–442.

(48) Rocca, J.; Erazú, M.; Fontana, M.; Arcondo, B. *J. Non-Cryst. Solids* **2009**, *355* (37–42), 2068–2073.

(49) Ito, K.; Moynihan, C. T.; Angell, C. A. *Nature* **1999**, *398* (6727), 492–495.

(50) Stølen, S.; Grande, T.; Johnsen, H.-B. *Phys. Chem. Chem. Phys.* **2002**, *4* (14), 3396–3399.

(51) Wei, S.; Lucas, P.; Angell, C. A. *J. Appl. Phys.* **2015**, *118* (3), 034903.

(52) Akola, J.; Jones, R. O. *Phys. Rev. B* **2007**, *76* (23), 235201.

(53) Orava, J.; Weber, H.; Kaban, I.; Greer, A. L. *J. Chem. Phys.* **2016**, *144* (19), 194503.

(54) Lee, S.-H.; Jung, Y.; Agarwal, R. *Nano Lett.* **2008**, *8* (10), 3303–3309.

(55) Redaelli, A.; Pirovano, A.; Tortorelli, I.; Ielmini, D.; Lacaita, A. L. *IEEE Electron Device Lett.* **2008**, *29* (1), 41–43.

(56) Lyeo, H.-K.; Cahill, D. G.; Lee, B.-S.; Abelson, J. R.; Kwon, M.-H.; Kim, K.-B.; Bishop, S. G.; Cheong, B. *Appl. Phys. Lett.* **2006**, *89* (15), 151904.

Chapter 6

Dynamics of GeSbTe nanoparticles on graphene

Abstract

Phase change materials are currently widely used in data storage and are considered as promising candidate for phase change memory. The properties of phase-change nanoparticles have been investigated yet the understanding of their dynamics is lacking. In this chapter we deposited GeSbTe nanoparticles directly on graphene support and studied the landing dynamics of these nanoparticles on graphene. The nanoparticles prefer to land on suspended graphene support three times higher compared to graphene on carbon support. Also the oxidation dynamics of the GeSbTe nanoparticles was investigated. It is found that the Ge atoms migrate to the periphery of the nanoparticles after exposure to air for two weeks.

Based on *Dynamics of GeSbTe phase-change nanoparticles on graphene,*
B. Chen, L. V. Do, G. ten Brink, G. Palasantzas, P. Rudolf, B. J. Kooi, to be submitted.

6.1 Introduction

Phase-change materials (PCMs) have attracted strong interest due to their high potential for applications in optical storage, electrical memory, photonic displays, etc..[1–3] They can be reversibly switched between their amorphous and crystalline phases within nanosecond time scale and nanometer length scale, while the significant optical and electrical contrasts between these two phases enable encoding and storing information by programing the PCMs between these two phases. The ever-increasing demand for information storage encourages the pursuing for storage media with stronger performances. One of the most promising paths is the down-scaling of the bit dimensions. Recently many investigations of three-dimensionally scaled down PCMs (nanoparticles) have been presented, where GeTe and $Ge_2Sb_2Te_5$ nanoparticles have been successfully grown by chemical synthesis and physical deposition.[4–7] The weak size dependence in crystallization temperature ensures the long-time stability of the amorphous state and the wide operation window, as elucidated in our previous paper.[6] Also demonstrated is that the GST NPs, especially the GST NPs prepared with CH_4 additional gas during deposition, exhibiting better data retention compared to the thin films and comparable crystallization speed in the switching regime, are a promising candidate for future phase change memory.[7]

Graphene has experienced intense investigations due to its unique mechanical, thermal and electron transport properties.[8–10] For instance, it has been demonstrated that the energy efficiency of the material in phase change memory was enhanced by inserting graphene between the active GST and the bottom electrode heater.[11] In this device, graphene played a role as a thermal barrier and limited the atomic migration of PCM that also leads to the endurance of the memory. In addition, there are numbers of investigations reporting that placing thin films or nanoparticles on graphene not only influenced the thin films or nanoparticles but also the electronic properties of graphene.[12–18] Some nanoparticles could form 2D structures and have strong interactions with graphene,[19,20] which could lead to the opening of the band gap of graphene and thereby greatly extends its potential in semiconductor applications.

On the other hand, the functionalization of graphene has attracted intensive studies.[21] Decorating graphene with NPs has applications in many fields, such as catalysis, sensors, supercapacitors, energy storage and the anode of Li ion battery.[22–25]

Despite the advantages it offers, sound understanding of the interaction between graphene and the GST NPs as well as the dynamics of NPs adsorption and oxidation are necessary before its applications. Although there have been comprehensive investigations on the metal oxide-graphene nanocomposite, the GST nanoparticles grown by inert gas condensation is “clean”, i.e. without surrounding ligands that usually play an important role in surface activity. Due to this difference, the dynamics of NPs deposition and subsequent oxidation remain ambiguous. In this chapter we report we deposited GST NPs on graphene and studied the interaction between the phase-change NPs and the graphene support. The dynamics of NPs attachment on the graphene and oxidation was unraveled by studying the morphology of the NPs.

6.2 Experimental methods

6.2.1 Graphene preparation

Graphene was grown on oxygen rich copper foils by chemical vapour deposition. Briefly, the copper foil (Alfa Aesar, 99.8%, #46365) with a thickness of 25 µm was cleaned by soaking in acetic acid for 8 hours, rinsed by water, before it was put into a quartz tube for growing the graphene. In order to eliminate the residual copper oxide on the copper surface, the quartz tube was filled with 0.1 mbar hydrogen (Messer, purity 5.0) , and it was heated up to 1035 ^{o}C. To grow graphene, 0.2 mbar mixture of argon and methane (5%) was added into the quartz tube at 1035 ^{o}C for 2 hours. Thereafter, the copper foil was cooled down to room temperature with all the gases remained.

After a high quality of monolayer graphene was confirmed by Raman measurement with He-Ne laser at 633 nm, graphene was transferred to a quantifoil R2/1 holey carbon (Electron Microscopy Sciences, Q225-AR1) TEM grids for the STEM characterization. Firstly, the TEM grids was placed on top of graphene on copper. Two drops of isopropanol (IPA) were deposited on the sample to enhance the binding between graphene and the carbon membrane of the quantifoil TEM grids after the IPA evaporated. The sample, consequently, had been annealed at 100 ^{o}C for 10 minutes to finally strengthen the contact between graphene and the TEM grids before the copper was etched away in $(NH_4)_2S_2O_8$ 0.1g/ml for 24 hours. The TEM grids covered with graphene were eventually rinsed three times in demi-water to eliminate any remaining trace of the etchant.

6.2.2 GST NPs deposition

The $Ge_2Sb_2Te_5$ phase-change nanoparticles with excellent size, crystallinity and composition control were grown by inert gas phase condensation based on magnetron sputtering, as described in chapter 2. The main chamber (to collect the NPs) is evacuated to a pressure of 10^{-8} mbar. Amorphous GST NPs were directly synthesized by sputtering the GST target (purity of 99.99%), employing a low current (0.15 A) to avoid the formation of crystalline NPs. The Ar gas flow (purity 99.9999%) used for the two types of samples analyzed in the present work is 35 sccm. Medium amount of CH_4 was used as additional gas to initiate the nucleation process.[6] Low discharge current (0.105 A) was adopted to ensure the amorphous state of the NPs. The NPs were directly deposited on Au quantifoil grids covered with transferred graphene at room temperature. The coverage was altered by changing the time and yield of the deposition process.

6.2.3 Characterization

The morphology of the as-deposited NPs were characterized in JEOL 2010 at 200 kV within 1 hour after sample deposition. The coverage is defined as the ratio of the NPs covered area over total area. The as-deposited amorphous NPs were crystallized by annealing them at a temperature of 180 ^{o}C for 10 minutes inside the JEOL 2010. The energy dispersive spectroscopy elemental mapping and high resolution TEM images were performed in JEOL ARM 200F and FEI Themis Z. High acceleration voltage (200 kV) was utilized to record overview bright-field TEM images of the GST NPs, but low acceleration voltages (40 and 60 kV) were used to record HAADF-STEM images when graphene is involved since high voltage (above 80 kV) can easily induce knock-on damage to the single layer graphene due to the collision of the beam electrons with the nucleus of the graphene target atom.[26,27]

6.3 Results and discussion

The quality of the graphene support layer was characterized by selected area electron diffraction (SAED) patterns (with an aperture diameter corresponding to 2.5 μm on the sample surface), as demonstrated in Figure 6.7 of the Appendix. The line profile of the diffractogram in Figure 6.7a indicates that the selected graphene support is a single layer,[28] while the broad halo at 3.3 1/nm infers the amorphous nature of the as-deposited GeSbTe nanoparticle (NPs). During the graphene transfer, it is possible for graphene to be teared and folded, which leads to the formation of bi-layer and multi-layer graphene locally as indicated in Figure 6.7b. Here we intentionally chose the single-layer graphene to image the GST NPs and the substrate.

The morphology of the NPs was characterized by bright field TEM images, as shown in Figure 6.1. The average diameter of the NPs is determined as 9.5±1.1 nm. The substrate consists of two distinct parts on the TEM grids: (1) (suspended) graphene on holes or (2) graphene on carbon support films (hereafter named graphene and carbon/graphene, respectively). Surprisingly the NPs attachment dynamics on the two different supports diverges remarkably, generating distinctly different morphologies of the NPs. As can be observed clearly in Figure 6.1a, the coverage of the NPs on the graphene (left side) is much higher than that on the carbon/graphene area (right side), although the NPs are directly attached to the graphene on both sides. Figure 6.1b-c show the overview image of the NPs on these two different areas that allow the quantification of the NPs coverage. It is found that the coverage on the graphene support layer area is roughly three times higher than the one on the carbon/graphene support film for the same sample. In order to verify the reproducibility of this difference, several samples with different coverages were prepared and characterized. As shown in Figure 6.1d, this difference in coverage is consistent for all of these samples with wide coverage range, from about 4 to 48 % on the graphene support layer. Moreover, one can nicely observe in Figure 6.1a that the coverage directly jumps to a high value at the vicinity of the carbon edge instead of a gradual change over some distance.

If the difference in coverage has some electrostatic or mechanical, i.e. long-range, origin, then a gradient in coverage near the carbon edge would be expected. For instance, when the difference stems from the mechanical flexibility of the graphene on the hole that dissipates the kinetic energy of the GST NPs (usually ~ 0.1 eV per atom [29]), a gradient in coverage close to the carbon edge should be observed since a gradient in flexibility also exists when the graphene is approaching the carbon edge. Although the energy per atom in the NP that is impinging on the graphene coated TEM grid is still close to the thermal energy ($3kT$ per atom with k the Boltzmann constant and T the absolute temperature), still the speed with which the clusters approach the grid is on the order of hundred meters per second. This will impact the sticking of the NPs on the various types of surfaces. The non-gradient variation in coverage for the various surface types then drives us to consider a thermodynamic origin: the surface free energy. Due to the nature of high surface free energy for graphene,[30] more NPs are adsorbed on the surface in order to reduce the surface energy, leading to a much higher coverage of the GST NPs in comparison to the carbon/graphene surface where the surface energy is already lowered by the supported carbon film. The other role of surface energy is adsorbing airborne hydrocarbon contamination on the surface in order to reduce the surface energy due to the long time exposure to air (~2 weeks). The adsorption of hydrocarbon to reduce surface energy of graphite and graphene has been observed by water contact angle measurements.[31,32]

The GST NPs were also simultaneously deposited on a continuous carbon support film and their morphology was characterized as well. It is worth noting that the coverage on a holey carbon TEM grid where the NPs were directly deposited on is comparable to the carbon/graphene support. This phenomenon indicates that the surface free energy is dominated by this amorphous carbon support film at the carbon/graphene area. The surface free energy of fresh graphene grown on a copper substrate was determined as 53.0 mJ/m^2 for Owens-Wendt approach,[32] slightly higher than the value of amorphous carbon films (49.3 mJ/m^2) utilizing the same approach.[33] After adsorption of airborne hydrocarbon contamination after 24 h of air exposure, the surface free energy of graphene decreased to 37.5 mJ/m^2. Note that all the experimental data were derived on a Cu/Graphene surface, the surface energy of suspended graphene is lacking due to the huge challenge to measure it.

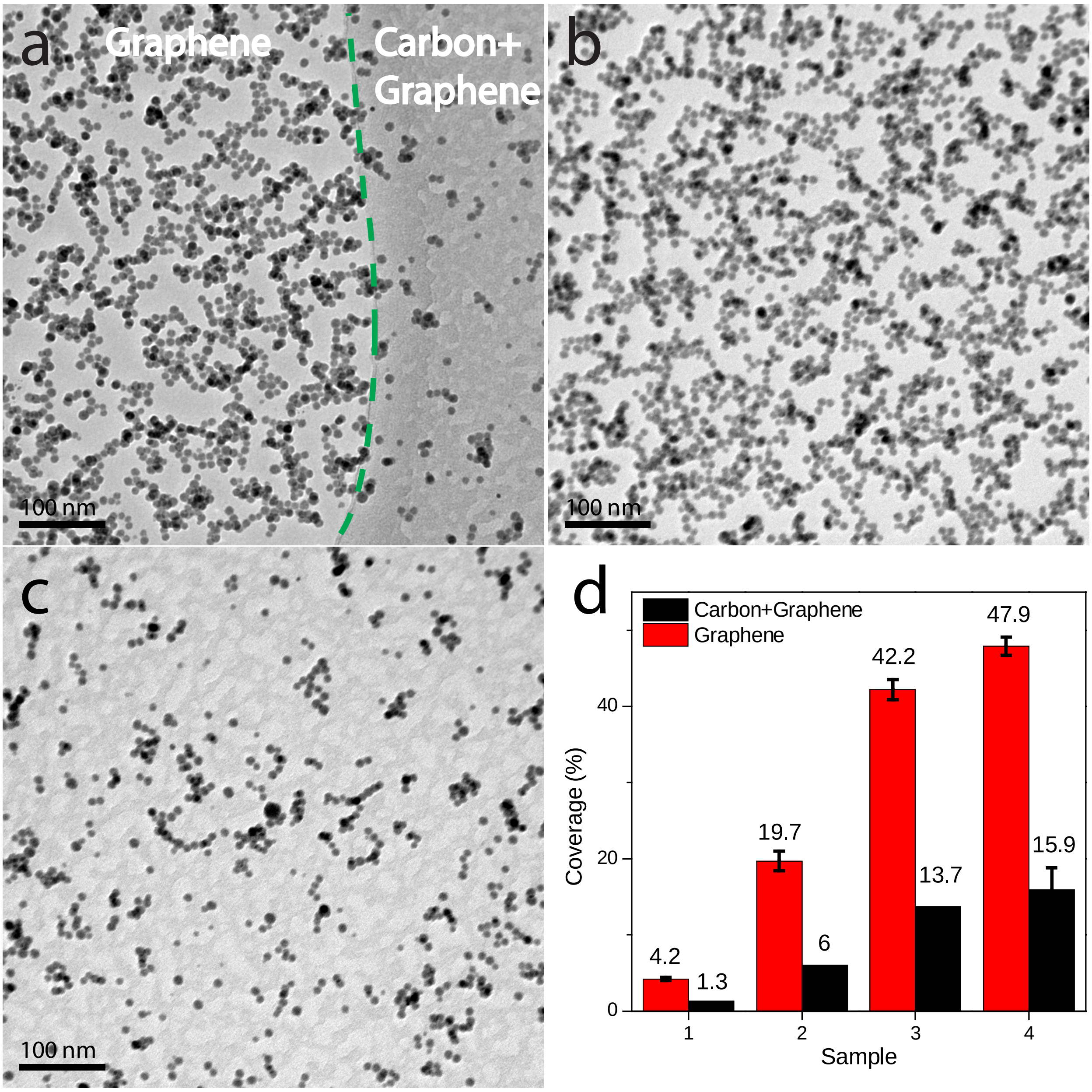

Figure 6.1 Morphology of $Ge_2Sb_2Te_5$ nanoparticles on graphene and carbon/graphene support. The NPs at the edge of carbon support film (indicated by the green dash curve) shows an abrupt increase of coverage (a). (b) and (c) display the morphology of GST NPs deposited on the graphene and carbon/graphene support films, respectively. This difference in coverage between suspended graphene and graphene on amorphous carbon is consistent with all the samples produced, as shown in (d).

The above results suggest a promising application of graphene: harvesting nanoparticles. The high surface energy of graphene also makes it possible to align the adsorbates onto it. Engineering graphene with nanoparticles has several emerging applications. Decorating graphene with metal oxide nanoparticles, such as MnO_2,[34] CuO [35] and Fe_3O_4,[36] is of interest as anodes in Li-ion batteries. So here airborne hydrocarbon adsorbates also provide the capability of decorating the graphene and gluing NPs on the surface. Moreover, this hydrocarbon adsorbates are removable by heating graphene to ~550 °C,[31] enabling the reversible switch of the surface state of graphene.

It has been demonstrated in our previous work that the overall composition of the GST NPs are in good agreement with the nominal stoichiometry of $Ge_2Sb_2Te_5$ (Ge:Sb:Te=22:22:56),[6] yet the elemental distribution within the NPs could not be determined due to instrumental limitations at that time. As shown in Figure 6.2, high spatial resolution energy dispersive spectroscopy (EDS) elemental mapping of as-deposited amorphous NPs on graphene has been performed, with the corresponding morphology of the NPs demonstrated by the high angle annular dark field - scanning transmission electron microscopy (HAADF-STEM) image, portraying the distribution of Ge, Sb and Te. The homogeneous distribution of the Ge, Sb and Te can be clearly observed in this figure. Moreover, no obvious oxidation (forming an outer shell) of (one of) these three elements can be detected in this mapping as confirmed by line profile of the combined mapping, inferring that the as-deposited GST NPs were not observably (< 1 nm) oxidized after exposure to air for 1 day.

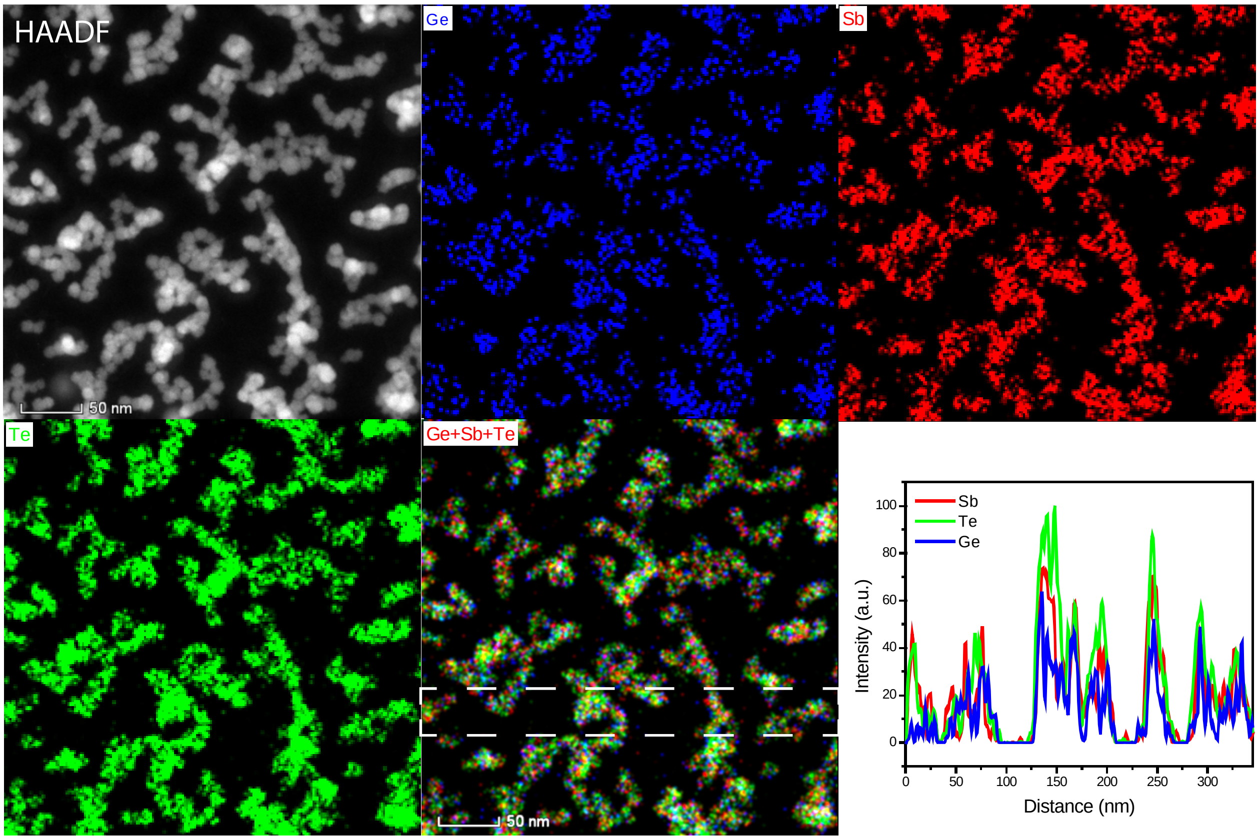

Figure 6.2 Energy dispersive spectroscopy (EDS) elemental mapping of amorphous GST NPs on graphene. The NPs were exposed to air for 1 day before performing this measurement.

To investigate the oxidation dynamics of the NPs, we exposed the GST NPs to air for 2 weeks after crystalizing them by annealing in TEM at a temperature of 180 ^{o}C for 10 minutes.[6] Figure 6.3 shows the HAADF and bright field images of NPs on graphene support film at different acceleration voltages (40 and 60 kV). Along the line of our previous results,[6] the GST crystals exhibit a combination of rock-salt and trigonal structures, where the lattice parameter of the rock-salt structure is ~1.8 % extended (with $d_{(022)}$=0.216 nm) in comparison to the lattice constant of GST films. While most of the NPs are in rock-salt phase, the trigonal phase was observed as well.[37] The van der Waals gaps are visible for some of the crystalized NPs.

Due to the high surface energy of graphene/nanoparticle composite and exposure to air, the airborne hydrocarbon contamination is further absorbed on the surface, depicted as the “cloud” in HAADF-STEM images (Figure 6.3a and c), while it is obscured in the bright field images (Figure 6.3b and d). Hence cautions have to be taken on interpreting the bright field images about hydrocarbon contaminations. The NPs are surrounded by the airborne hydrocarbon contamination. On one hand, the NPs prefer to land on the pre-existed hydrocarbon adsorbates. On the other hand, owing to the high surface to volume ratio of the nanoparticles (with diameter less than 10 nm), more airborne hydrocarbon is adsorbed by the NPs to reduce their surface energy, forming the encircling cloud-like structure. Yet it is impossible to distinguish that whether the hydrocarbons were adsorbed before or after NPs deposition.

At the edge of the NPs, large amount of atoms seem to distribute randomly instead of being bonded to the crystal. Then the hydrocarbon contamination then plays a role as a highway for the migration of atoms, leading to the enrichment of atoms at the edge of the hydrocarbon, as indicated by the white arrows in Figure 6.3a and c. Figure 6.3 also demonstrates an acceleration voltage dependent mobility of these atoms. It is evident that more randomly distributed atoms assemble at the boundary of the hydrocarbon and the periphery of the NPs (green arrows in Figure 6.3a and c) imaged at 60 kV in comparison to that recorded at 40 kV, indicating that the mobility of the heavy atoms correlates to the electron beam irradiation. The real time video obtained by recording high resolution bright field images at each second shows the pop-up of heavy atoms induced by the electron beam at an acceleration voltage of 60 kV. It is highly possible that the Ge atoms migrate towards the outside of the NPs and forms a GeO_x shell due to its highest sensitivity to oxygen among the Ge, Sb, Te elements.

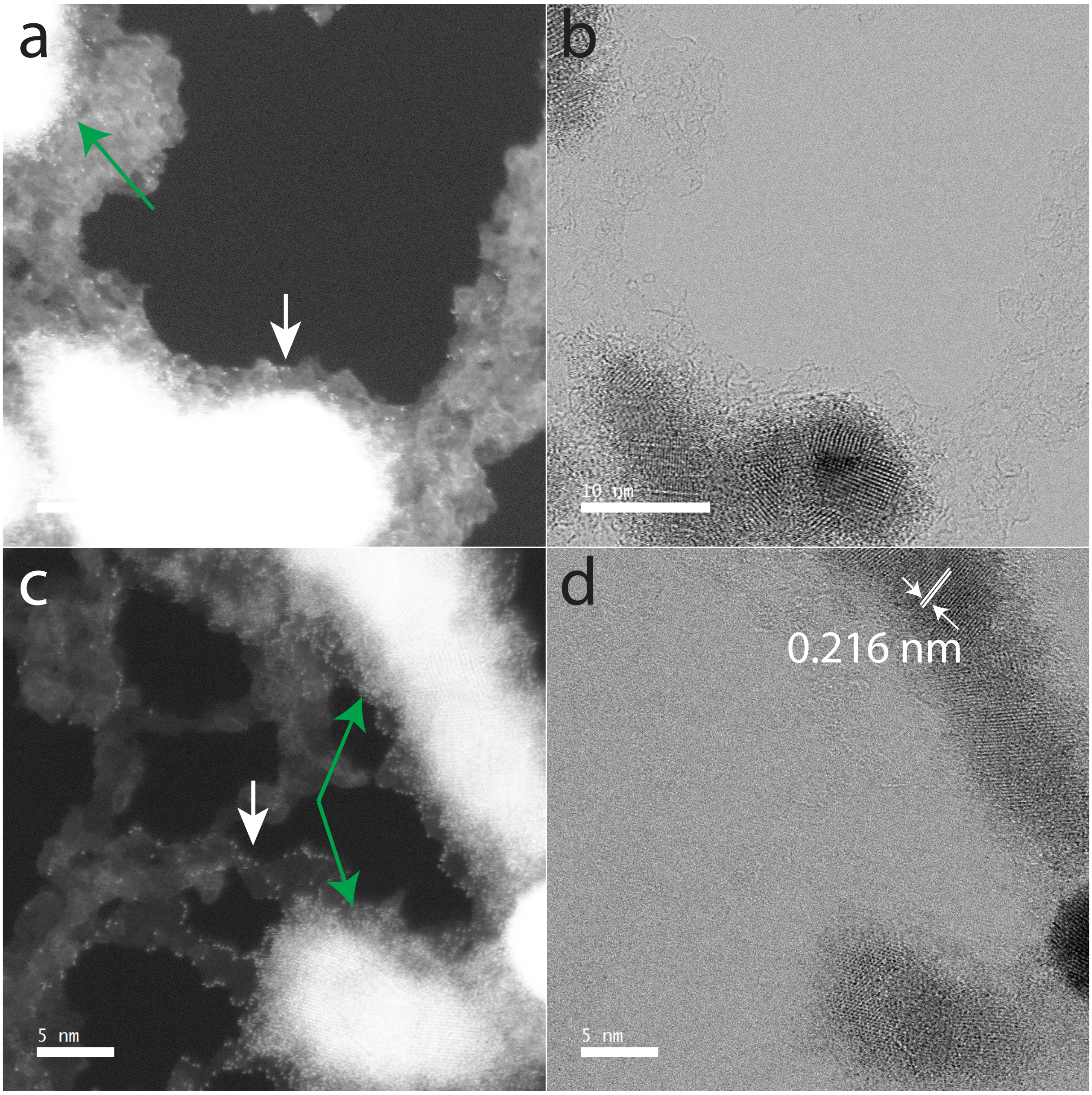

Figure 6.3 High resolution TEM images of crystallized NPs on graphene support film. (a) and (c) are the high angle angular dark field images recorded using 40 and 60 kV electron beams, respectively, while (c) and (d) are the corresponding bright field images.

In order to verify the species of the atoms that move towards the outside of the NPs and the edge of the hydrocarbon, EDS elemental mapping has been conducted for the NPs, as shown in Figure 6.4. The Sb and Te atoms mostly remain within the NPs, while small amount of Te atoms move onto the hydrocarbon cloud. However, Ge atoms move towards the periphery of the NPs and form distinct oxide shells surrounding the NPs, which is further confirmed by the similar distribution of Ge and O atoms in Figure 6.4. The line profile of the elemental maps for these four elements markedly portrays the identical distribution for Ge and O at the shell of the NPs. Figure 6.8 of the Appendix depicts more evidently diffusion of Ge and Te atoms compared to Sb atoms on the hydrocarbon contamination. These results show the high sensitivity of the GST NPs (especially Ge) to the air exposure, inferring the necessity of a capping layer to protect the NPs. Also revealed by the above results is that Ge and Te atoms have a higher mobility on the hydrocarbon contamination than Sb.

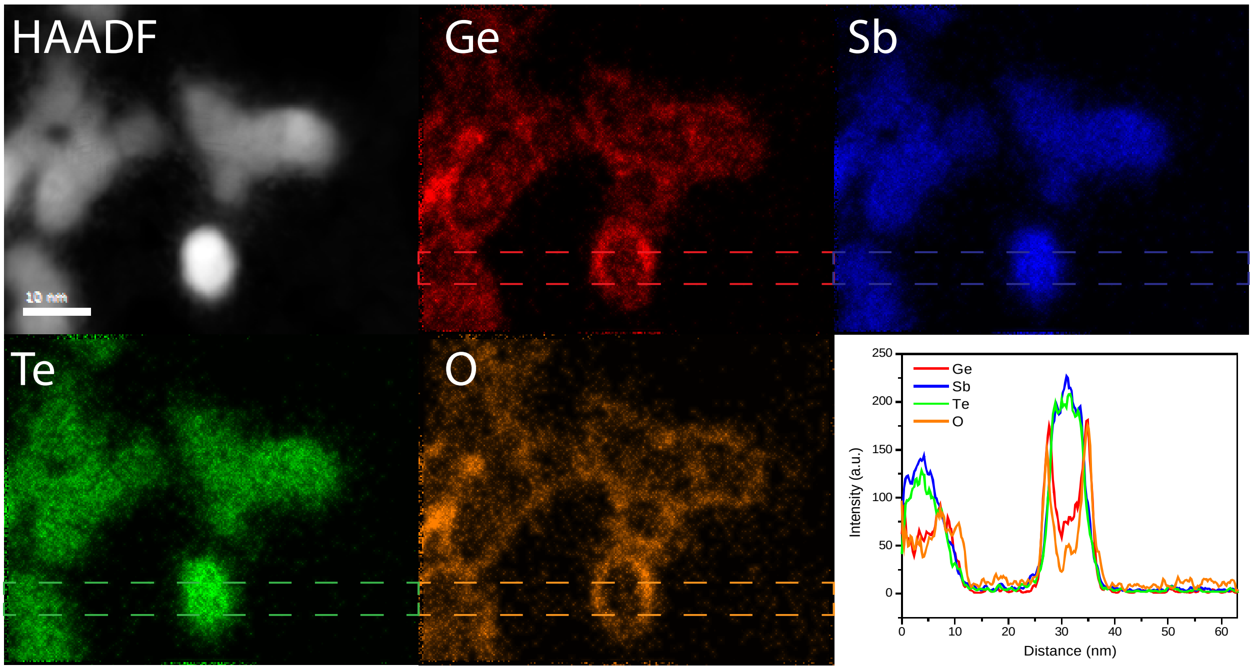

Figure 6.4 Energy dispersive spectroscopy (EDS) elemental mapping and the corresponding line profiles of NPs exposed in air for two weeks.

In contrast, the NPs deposited on the carbon/graphene support film show a rather different morphology and oxidation dynamics after crystallization in comparison to the NPs on the graphene support, as elucidated in Figure 6.5. Although hydrocarbon adsorbate can be hardly observed in both HAADF-STEM and bright field images, the adsorption still occurred. Some hydrocarbon contamination is observable in some HAADF-STEM images. There are two possible reasons for the less visible airborne hydrocarbon contamination in this area: 1) the surface energy of the graphene has been lowered by the carbon support film, so less hydrocarbons are absorbed; 2) the thick carbon support film (~12 nm) strongly reduces the signal and thus visibility of the hydrocarbon contamination. Considering the phenomenon that GST NPs are attached to hydrocarbon contaminations, it is highly possible that the graphene adsorbs more hydrocarbon in comparison to carbon/graphene due to higher surface energy, leading to higher coverage since the NPs can land on the hydrocarbon softly.

Similar to the GST NPs on the graphene support layer, the EDS elemental mapping shows uniform distribution of Ge, Sb and Te atoms with GeO_x shells formed surrounding the NPs. Although the Ge atoms at the shell can be detected, more Ge atoms remain within the NPs compared to the NPs on graphene, as proved by line profile of these elemental maps. Also the less obvious oxidation shell indicates that the NPs on the carbon/graphene support are less heavily oxidized compared to the NPs on graphene. Because of the similar size of the NPs profiled in Figure 6.4 and 6.5, a possible size effect on the oxidation can be excluded. Another information that can be derived from the line profile is that O atoms are present on the whole surface. The wide distribution of O atoms stems from the hydrocarbon and water adsorbed on the substrate.

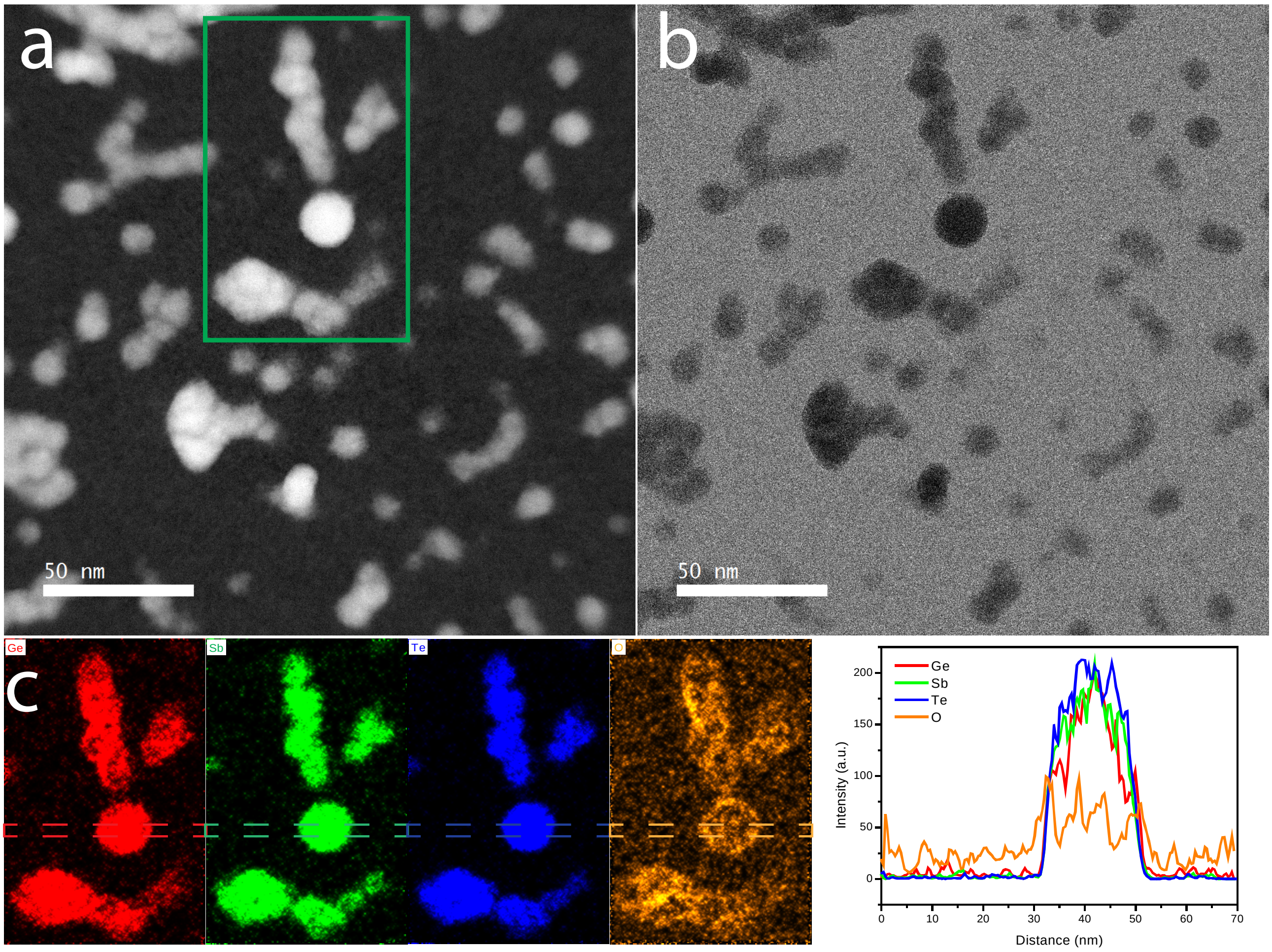

Figure 6.5 HAADF (a) and bright field (b) images of the GST NPs on the carbon/graphene supporting film at acceleration voltage of 40 kV. EDS elemental mapping of this area is shown in (c), indicating that some limited oxidation occurred of the NPs on the carbon/graphene, but oxidation is definitely not as strong as for NPs on graphene with clearly developed GeO_x shell (cf. Figure 6.4).

Since acceleration voltage above 80 kV can easily induce knock-on defects to graphene,[26] low acceleration voltage was used to image graphene in this work. The atomic structure was imaged with HAADF-STEM at 40 and 60 kV with a resolution where individual atoms in the graphene are still resolved, as depicted in Figure 6.6. The STEM image shows the C-C separation of 1.41 Å, in excellent line with the crystallography structure of graphene (where C-C separation is 1.42 Å).[38] Defects could not be observed in large areas under the electron irradiation. Surprisingly, the electron beam induced etching, which is believed to happen for low acceleration voltage (20 to 100 kV),[26] was not observed in this work. No holes could be observed in the HAADF-STEM images, even near the hydrocarbon contamination sites, where the hole nucleates.[26] The signal-to-noise ratio can be improved by integrating multi frames. Figure 6.9 of the Appendix shows the proccessed image after 21 frames intergration, portraying a sharper contrast.

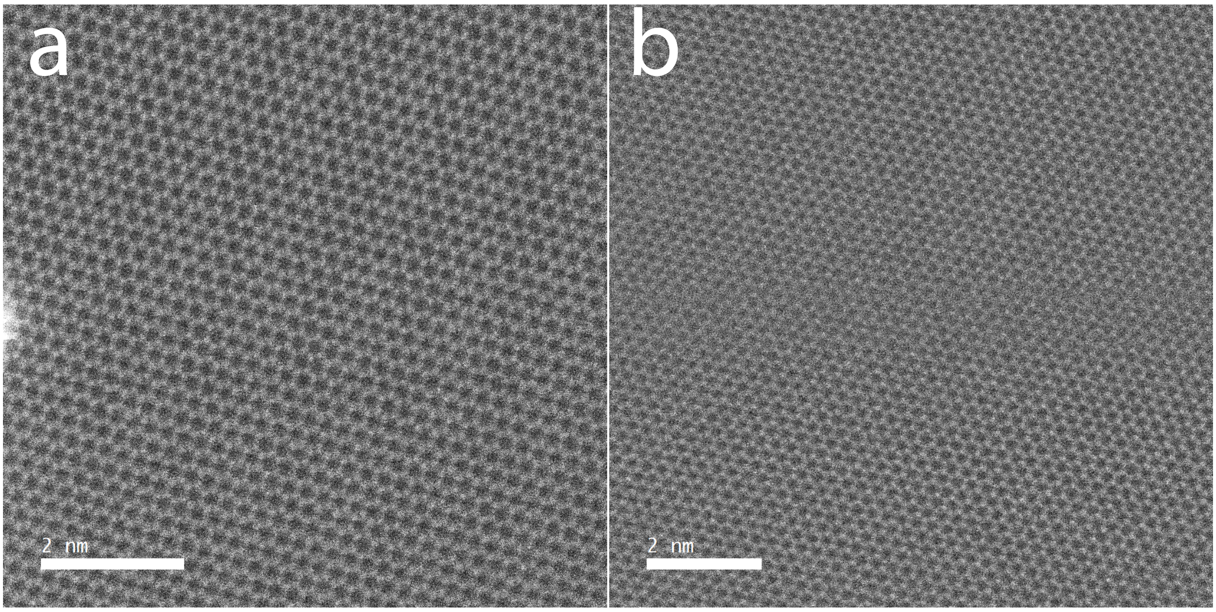

Figure 6.6 Single frame HAADF-STEM images of graphene at 40 and 60 kV.

6.4 Conclusions

Phase-change $Ge_2Sb_2Te_5$ nanoparticles have been deposited on CVD grown graphene support layers transferred on Au quantifoil. The coverage of nanoparticles on the suspended graphene is about three times higher than that on the carbon/graphene support. We attributed this distinct difference to the variation in surface energy, indicating that graphene can be used to (more effectively) harvest nanoparticles. Our observations of dynamics on the graphene support is strongly influenced by hydrocarbon contamination, which is effectively observed by HAADF-STEM images but not by bright field images. With uniform distributions for the Ge, Sb and Te atoms for the nascent $Ge_2Sb_2Te_5$ nanoparticles, these particles are sensitive to air exposure, especially Ge atoms which tend to form after prolonged times clear GeO_x shells. The NPs deposited on graphene were oxidized more heavily than the NPs on carbon/graphene support. High quality atomic structure of graphene has been evidently resolved at accelerating voltages as low as 40 kV.

Appendix

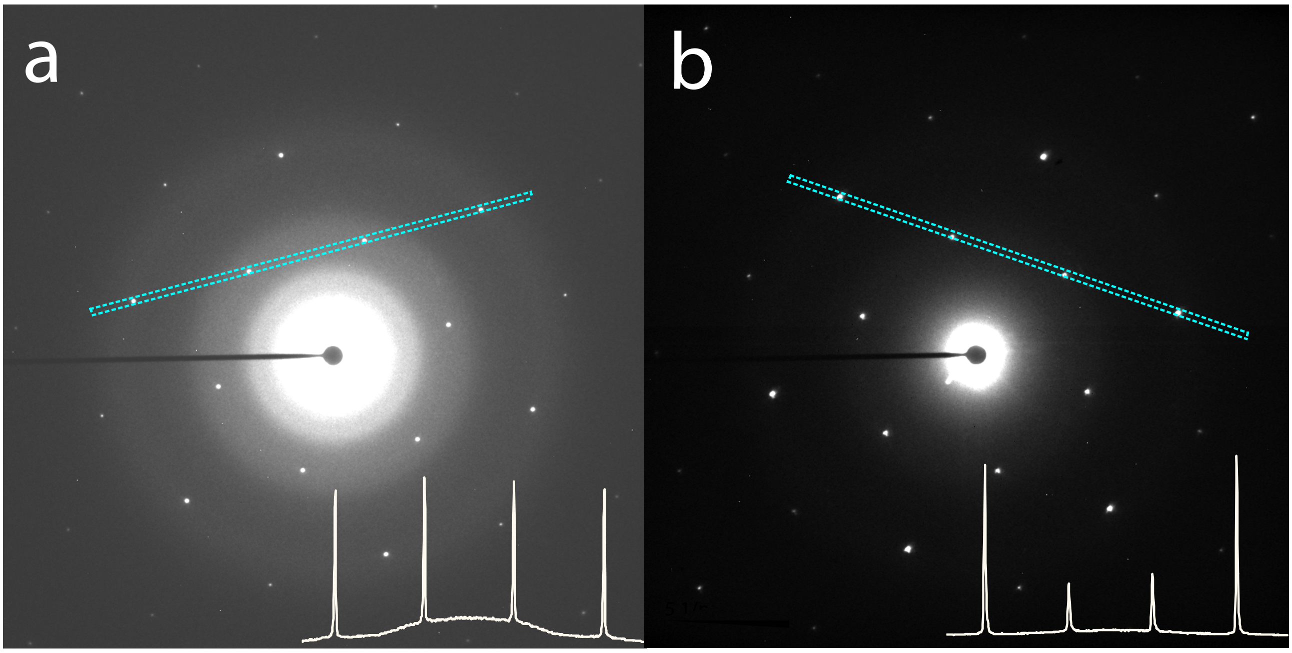

Figure 6.7 Selected area electron diffraction pattern of graphene with (a) and without GST NPs (b). The line profile inserted in (a) indicates that the graphene in this area is single layer.[28] The broad bright halo demonstrates the amorphous nature of the as-deposited GST NPs. The line profile in (b) shows the bilayer graphene.

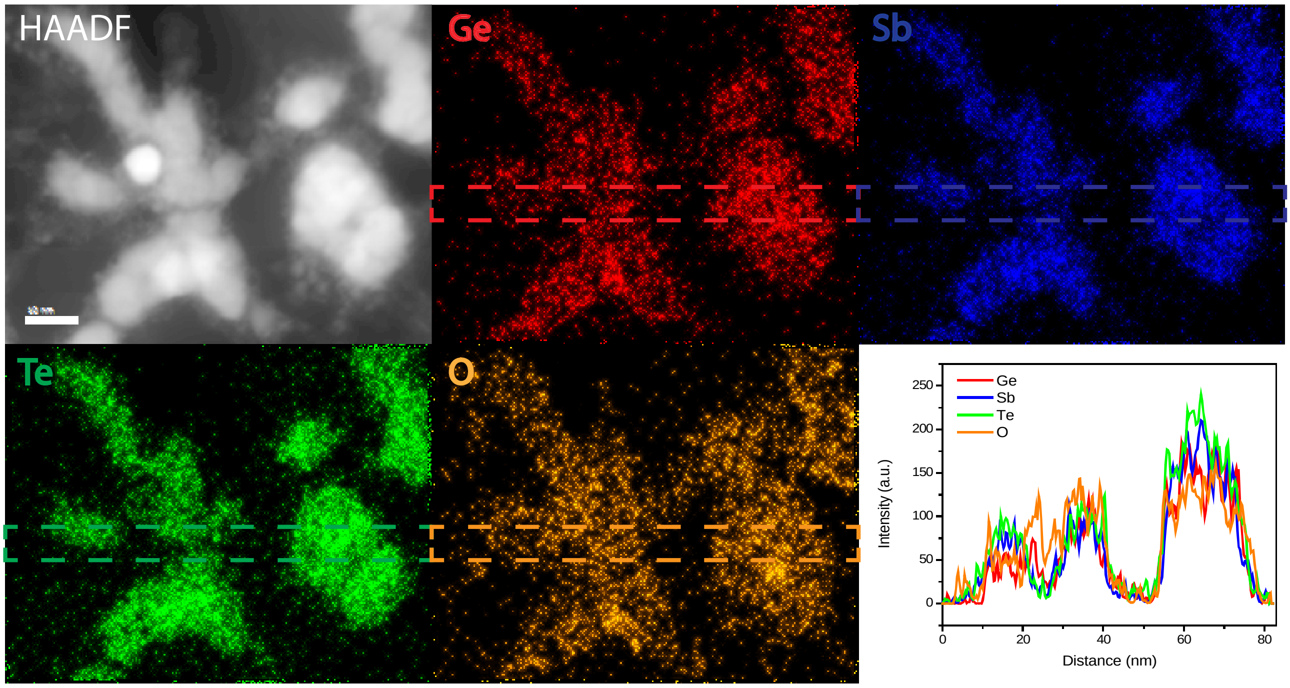

Figure 6.8 The high angle annular dark field image and energy dispersive spectroscopy elemental mapping of GST NPs on graphene. The NPs were exposed to air for two weeks after crystallization in TEM. Results were obtained with an accelerating voltage of 40 kV.

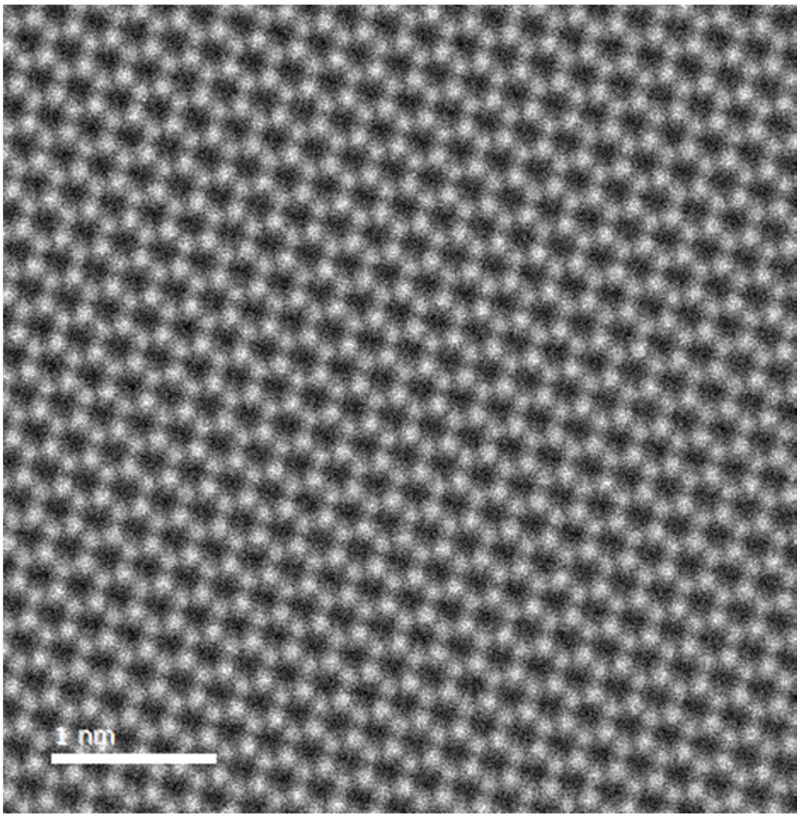

Figure 6.9 40 kV HAADF-STEM image of graphene, where 21 frames were integrated. Line profiles taken show a C-C separation of 1.41 Å that matches well with the crystallography structure of graphene.

References

(1) Wuttig, M.; Yamada, N. *Nat. Mater.* **2007**, *6* (11), 824–832.

(2) Burr, G. W.; Breitwisch, M. J.; Franceschini, M.; Garetto, D.; Gopalakrishnan, K.; Jackson, B.; Kurdi, B.; Lam, C.; Lastras, L. A.; Padilla, A.; Rajendran, B.; Raoux, S.; Shenoy, R. S. *J. Vac. Sci. Technol. B* **2010**, *28* (2), 223–262.

(3) Hosseini, P.; Wright, C. D.; Bhaskaran, H. *Nature* **2014**, *511* (7508), 206–211.

(4) Caldwell, M. A.; Raoux, S.; Wang, R. Y.; Wong, H.-S. P.; Milliron, D. J. *J. Mater. Chem.* **2010**, *20* (7), 1285–1291.

(5) Arachchige, I. U.; Soriano, R.; Malliakas, C. D.; Ivanov, S. A.; Kanatzidis, M. G. *Adv. Funct. Mater.* **2011**, *21* (14), 2737–2743.

(6) Chen, B.; ten Brink, G. H.; Palasantzas, G.; Kooi, B. J. *Sci. Rep.* **2016**, *6*.

(7) Chen, B.; ten Brink, G. H.; Palasantzas, G.; Kooi, B. J. *J. Phys. Chem. C* **2017**, *121* (15), 8569–8578.

(8) Lee, C.; Wei, X.; Kysar, J. W.; Hone, J. *Science* **2008**, *321* (5887), 385–388.

(9) Balandin, A. A.; Ghosh, S.; Bao, W.; Calizo, I.; Teweldebrhan, D.; Miao, F.; Lau, C. N. *Nano Lett.* **2008**, *8* (3), 902–907.

(10) Chen, J.-H.; Jang, C.; Xiao, S.; Ishigami, M.; Fuhrer, M. S. *Nat. Nanotechnol.* **2008**, *3* (4), 206–209.

(11) Ahn, C.; Fong, S. W.; Kim, Y.; Lee, S.; Sood, A.; Neumann, C. M.; Asheghi, M.; Goodson, K. E.; Pop, E.; Wong, H.-S. P. *Nano Lett.* **2015**, *15* (10), 6809–6814.

(12) Wu, Z.-S.; Ren, W.; Wen, L.; Gao, L.; Zhao, J.; Chen, Z.; Zhou, G.; Li, F.; Cheng, H.-M. *ACS Nano* **2010**, *4* (6), 3187–3194.

(13) Guo, S.; Sun, S. *J. Am. Chem. Soc.* **2012**, *134* (5), 2492–2495.

(14) Wang, B.; Park, J.; Wang, C.; Ahn, H.; Wang, G. *Electrochimica Acta* **2010**, *55* (22), 6812–6817.

(15) Zhou, X.; Yin, Y.-X.; Wan, L.-J.; Guo, Y.-G. *Adv. Energy Mater.* **2012**, *2* (9), 1086–1090.

(16) Xue, D.-J.; Xin, S.; Yan, Y.; Jiang, K.-C.; Yin, Y.-X.; Guo, Y.-G.; Wan, L.-J. *J. Am. Chem. Soc.* **2012**, *134* (5), 2512–2515.

(17) Zhou, Y.-G.; Chen, J.-J.; Wang, F.; Sheng, Z.-H.; Xia, X.-H. *Chem. Commun.* **2010**, *46* (32), 5951–5953.

(18) Zhou, X.; Yin, Y.-X.; Wan, L.-J.; Guo, Y.-G. *Chem. Commun.* **2012**, *48* (16), 2198–2200.

(19) Qiu, C.; Zhou, H.; Cao, B.; Sun, L.; Yu, T. *Carbon* **2013**, *59*, 487–494.

(20) Huang, C.; Lin, H.-Y.; Huang, C.-H.; Shiue, R.-J.; Wang, W.-H.; Liu, C.-Y.; Chui, H.-C. *Nanoscale Res. Lett.* **2012**, *7* (1), 618.

(21) V, G.; M, O.; Ab, B.; V, C.; N, K.; Kc, K.; P, H.; R, Z.; Ks, K. *Chem. Rev.* **2012**, *112* (11), 6156–6214.

(22) Chen, X.; Wu, G.; Chen, J.; Chen, X.; Xie, Z.; Wang, X. *J. Am. Chem. Soc.* **2011**, *133* (11), 3693–3695.

(23) Kamat, P. V. *J. Phys. Chem. Lett.* **2010**, *1* (2), 520–527.

(24) Chen, W.; Li, S.; Chen, C.; Yan, L. *Adv. Mater.* **2011**, *23* (47), 5679–5683.

(25) Raccichini, R.; Varzi, A.; Passerini, S.; Scrosati, B. *Nat. Mater.* **2015**, *14* (3), 271–279.

(26) Meyer, J. C.; Eder, F.; Kurasch, S.; Skakalova, V.; Kotakoski, J.; Park, H. J.; Roth, S.; Chuvilin, A.; Eyhusen, S.; Benner, G.; Krasheninnikov, A. V.; Kaiser, U. *Phys. Rev. Lett.* **2012**, *108* (19), 196102.

(27) Meyer, J. C.; Kisielowski, C.; Erni, R.; Rossell, M. D.; Crommie, M. F.; Zettl, A. *Nano Lett.* **2008**, *8* (11), 3582–3586.

(28) Meyer, J. C.; Geim, A. K.; Katsnelson, M. I.; Novoselov, K. S.; Obergfell, D.; Roth, S.; Girit, C.; Zettl, A. *Solid State Commun.* **2007**, *143* (1–2), 101–109.

(29) Haberland, H.; Insepov, Z.; Moseler, M. *Phys. Rev. B* **1995**, *51* (16), 11061–11067.

(30) Braga, S. F.; Coluci, V. R.; Legoas, S. B.; Giro, R.; Galvão, D. S.; Baughman, R. H. *Nano Lett.* **2004**, *4* (5), 881–884.
(31) Li, Z.; Wang, Y.; Kozbial, A.; Shenoy, G.; Zhou, F.; McGinley, R.; Ireland, P.; Morganstein, B.; Kunkel, A.; Surwade, S. P.; Li, L.; Liu, H. *Nat. Mater.* **2013**, *12* (10), 925–931.
(32) Kozbial, A.; Li, Z.; Conaway, C.; McGinley, R.; Dhingra, S.; Vahdat, V.; Zhou, F.; D'Urso, B.; Liu, H.; Li, L. *Langmuir* **2014**, *30* (28), 8598–8606.
(33) Zhao, Q.; Liu, Y.; Abel, E. W. *J. Colloid Interface Sci.* **2004**, *280* (1), 174–183.
(34) Yan, J.; Fan, Z.; Wei, T.; Qian, W.; Zhang, M.; Wei, F. *Carbon* **2010**, *48* (13), 3825–3833.
(35) Wang, B.; Wu, X.-L.; Shu, C.-Y.; Guo, Y.-G.; Wang, C.-R. *J. Mater. Chem.* **2010**, *20* (47), 10661–10664.
(36) Zhang, M.; Lei, D.; Yin, X.; Chen, L.; Li, Q.; Wang, Y.; Wang, T. *J. Mater. Chem.* **2010**, *20* (26), 5538–5543.
(37) Lotnyk, A.; Bernütz, S.; Sun, X.; Ross, U.; Ehrhardt, M.; Rauschenbach, B. *Acta Mater.* **2016**, *105*, 1–8.
(38) Castro Neto, A. H.; Guinea, F.; Peres, N. M. R.; Novoselov, K. S.; Geim, A. K. *Rev. Mod. Phys.* **2009**, *81* (1), 109–162.

Chapter 7

Crystallization kinetics of GeTe nanoparticles

Abstract

Chalcogenide based phase change materials (PCMs) are of great interest as promising candidates for novel electrical nonvolatile memories and have been applied successfully in rewritable optical disks. Nano-structured PCMs are considered as the next generation building blocks for their low power consumption, high storage density and fast switching speed. Yet their crystallization kinetics at high temperature, the rate-limiting property upon switching, faces great challenges due to the short time and length scales involved. Here we present a facile method to synthesize highly controlled, ligand-free GeTe nanoparticles, an important PCM, with average diameter under 10 nm. Subsequent crystallization by slow and ultrafast rates allow unravelling of the crystallization kinetics, demonstrating the break-down of Arrhenius behavior of crystallization and a fragile-to-strong transition in the viscosity as well as the overall crystal growth rate for the as-deposited GeTe NPs. The obtained results pave the way for further development of phase-change memory based on GeTe at sub-lithographic sizes.

Based on *Resolving the crystallization kinetics of GeTe phase-change nanoparticles,*
B. Chen, D. de Wal, G. ten Brink, G. Palasantzas, B. J. Kooi, submitted.

7.1 Introduction

Based on the rapid and reversible switching between the amorphous and crystalline phases that offers strong optical and electrical contrast between these two phases, phase-change materials (PCMs) have attracted attention in various fields, such as optical data storage and novel electrical nonvolatile memories.[1,2] Very recently they were successfully utilized in emerging applications, like solid state displays, on-chip photonic circuitry and neuromorphic computing.[3–5] The switching of the PCMs relies upon proper heating and cooling of the materials. Heating the amorphous PCMs with pulses (either electric or laser) at tens of ns triggers the crystallization, and melting followed with quenching them by ultrashort pulses induces the amorphization of the PCMs. Understanding the crystallization kinetics of PCMs thus lies at the heart of their switching. However, owing to the short time scale (tens of ns) and length scale (~tens of nm) involved, it has been highly challenging for a long time to investigate the crystallization kinetics by traditional measurements that allow only low heating rates (e.g. below 3 K s^{-1}). However, with the development of ultrafast differential scanning calorimetry (DSC), a powerful tool, that enables heating the specimen up to 40000 K s^{-1}, has become (commercially) available in recent years. Subsequently, the crystallization kinetics of (amorphous) $Ge_2Sb_2Te_5$ and AgInSbTe, GeSb thin films and GeSbTe nanoparticles (NPs) have been investigated by ultrafast DSC.[6–9] As a result, the crystallization behaviors at high heating rates were unraveled as well as the temperature dependency of viscosity and crystal growth rate. Apart from the ultrafast DSC, other techniques were developed to understand the crystallization kinetics of PCMs, such as laser-based time-resolved reflectivity measurements, isothermal technique monitoring the thickness change of amorphous PCMs and microthermal stage-based resistance measurements.[10–12] Crystal growth rates over wide temperature ranges were unraveled for melt-quenched AgInSbTe and doped-$Ge_2Sb_2Te_5$ PCMs.

GeTe, as a promising candidate for phase-change memory,[13] has received considerable attention in particular regarding the understanding of its crystallization kinetics. Dynamic transmission electron microscope (DTEM) was adopted to study the crystal growth rate near the melting temperature.[14] Very recently the crystallization kinetics of GeTe thin films was explored by crystalizing the specimen using ultrafast DSC with a large range of heating rates and subsequent modeling of the obtained results.[15]

Another intriguing property of PCMs is their excellent scalability that is fundamental for future memory devices. Scaling PCMs provides huge advantages,[16–18] such as high information storage density, fast switching speed and low power consumption per bit. Therefore many studies have been devoted to exploring the scaling of PCMs. Three dimensional down-scaling of GeTe PCMs into nanoparticles with diameters below 20 nm using chemical synthesis was successfully realized recently.[19,20] In this case, size dependent polar ordering in crystalline GeTe NPs has been observed.[21] In addition, a strong size dependence of the crystallization temperature has been observed for amorphous GeTe NPs, especially for NP diameters below 10 nm. For instance, the crystallization temperature reached 400 ^{o}C for GeTe NPs having a diameter of 1.8 nm,[19] which is more than 220 ^{o}C higher in comparison with the crystallization temperature for the bulk GeTe, suggesting ultrahigh stability of the amorphous phase for these NPs. Despite the successful synthesis of the amorphous and crystalline GeTe nanoparticles (NPs), determining the crystallization kinetics of GeTe NPs is highly challenging owing to the short time scale involved in the crystallization at high temperature. On the other hand, inert gas condensation based on magnetron sputtering offers a one-step synthesis of ligand-free NPs in ultrahigh vacuum. The large yield of the deposition allows us to investigate the crystallization kinetics of the GeTe NPs by ultrafast DSC. In this work we present the synthesis of GeTe NPs with excellent size, crystallinity and composition control by inert gas condensation. Utilizing ultrafast heating (up to 20000 K s^{-1}) in conjunction with DSC and subsequent numerical modeling allowed us to assess the crystallization kinetics of as-deposited amorphous GeTe NPs in the (extrapolated) temperature range between the glass transition and melting temperatures.

7.2 Experimental methods

7.2.1 Sample preparation

The GeTe phase-change nanoparticles (NPs) were synthesized by magnetron sputtering inert gas condensation using a home-modified nanoparticle deposition system (Nanogen 50). The sample chamber was evacuated to 10^{-8} mbar before NPs deposition. Amorphous GeTe NPs were directly synthesized by sputtering the GeTe target (purity of 99.99%), employing a low current (0.15 A) to avoid the formation of crystalline NPs. The Ar gas flow (purity 99.9999%) used to sputter the target is 35 sccm. A small amount of methane was used to promote the formation of the nascent GeTe clusters in the plasma.[22] Analogous to chapter 5, the NPs were deposited directly on a pre-cleaned glass substrate and transmission electron microscope (TEM) holey carbon grids taped outside the periphery of the NPs beam for subsequent characterization of crystallization.

7.2.2 Morphology and slow crystallization

Analogous to chapter 4, the morphology, composition and slow crystallization of the as-deposited GeTe NPs were characterized by TEM (JEOL 2010) at 200 kV after deposition. The slow crystallization process for the GeTe NPs was monitored by *in-situ* heating in TEM. The detailed methodology is described in chapter 2 and 4. The temperature interval used here is 3 ^{o}C after the appearance of observable diffraction spots on the SAED patterns. The heating rate above 200 ^{o}C is estimated as 0.03 K s^{-1}. At each temperature step (3 °C), a time interval of 60 seconds was taken for the sake of stabilization of the TEM membrane to avoid the influence of drifting caused by thermal expansion. The diameter of the selected area aperture for the SAED patterns is 2.5 μm. The NP density is assessed as ~ 6000 μm^{-2}, however the total number of NPs selected in the SAED patterns cannot be estimated accurately because of the irregularly distributed holes in the carbon support film.

7.2.3 Fast crystallization and modelling

Similar to chapter 5, the phase transitions of the samples were subsequently measured by ultrafast differential scanning calorimetry (DSC, Mettler-Toledo Flash DSC 1), with the sensor chips (USF-1) each containing the actual sensor and reference area. The details of measurements can be found in chapter 5. The approximate size of the individual flakes measured is roughly 20×20 μm^2. The heating rates (Φ) adopted in this work varied from 100 to 20000 K s^{-1}. The thermal lag has no significant influence on the kinetics, as discussed in the Appendix of this chapter. Analogous to chapters 3 and 5, numerical modeling was performed to understand the crystallization kinetics of the GeTe NPs, with the details of the method shown in the Appendix of chapter 3. In the numerical modeling, the generalized MYEGA model was used to describe the temperature dependency of viscosity of the as-deposited amorphous GeTe NPs.[23] The nucleation process was simplified by a constant nuclei density (site saturation) and the crystallization process is thus largely governed by the temperature dependence of the growth, as used in chapters 3 and 5. In the fitting process, a data point derived from the *in-situ* heating in TEM was also adopted, with the Φ assessed as 0.03 K s^{-1}.

7.3 Results and discussion

7.3.1 Low heating rate crystallization

The composition, morphology and the crystallinity of the as-deposited GeTe nanoparticles (NPs) were characterized by transmission electron microscopy (TEM). The composition of the GeTe NPs was scrutinized by energy dispersive X-ray spectrometry (EDS), showing the atomic ratio of Ge:Te=45:55 (±1); see Figure 7.5 of the Appendix. The slight deficiency (~ 2-3 at%) of Ge element is consistent with the results obtained earlier for the GeSbTe and GeTe NPs synthesized by inert gas condensation. The most probable explanation is that the effective sputtering rate of Ge is slightly lower in comparison to Sb and Te. Figure 7.1a shows the morphology of the as-deposited GeTe NPs, indicating that no coalescence of the NPs but only aggregation takes place during deposition.

The average diameter of the NPs was then determined as 9.4±1.6 nm, as demonstrated in Figure 7.6 of the Appendix, indicating a relatively narrow size distribution of the GeTe NPs. The selected area electron diffraction (SAED) patterns, as shown in Figure 7.1b, demonstrate the amorphous nature of the as-deposited GeTe NPs due to the lack of sharp diffraction rings associated with crystal planes.

Analogous to our previous study on GeSbTe NPs (chapter 4), the crystallization of the GeTe NPs at low heating rate was characterized by *in-situ* heating in TEM.[22] The GeTe NPs were annealed within the TEM, with the corresponding SAED patterns recorded at each temperature step. Figure 7.1c illustrates the SAED patterns at 270 °C, with diffraction rings distinctly detectable. Figure 7.1d demonstrates the azimuthal integral of the SAED patterns, showing that the crystalline peak appears at a temperature of ~230 °C and saturates at ~260 °C. It is noticeable that the GeTe NPs coalesce during crystallization. This can be distinguished by comparing bright field images of the same area before and after the in-situ heating, as shown in Figure 7.7 of the Appendix. The interplanar spacing derived from the SAED patterns are: d_{202}=0.297 nm and $d_{024/220}$=0.210 nm, showing excellent agreement with the value for GeTe NPs obtained earlier.[21] The peaks for {024} and {220} planes cannot be resolved for such small NPs. Another work has found that the two peaks merged into one in synchrotron X-ray diffraction for GeTe NPs smaller than 17 nm.[21] Through recording and normalizing the evolution of the diffraction intensity for {024}/{220} peak as a function of temperature, the crystallinity as a function of temperature can be obtained, as shown in Figure 7.1e. After fitting the data with the Boltzmann function, the crystallization temperature, defined as the temperature where the maximum 1st order derivative occurs, is then derived as 238.3±0.3 °C that is 60 °C higher than that of the bulk GeTe (~175 °C).[24] The fitting was excellent, as assessed by the adjusted R^2=0.997. Figure 7.1f compares the size dependency of crystallization temperature for GeTe and GeSbTe NPs.[19,20,22] Opposite trends for the size dependency can be detected for these two kinds of NPs, where the crystallization temperature drastically rises for GeTe while a slight decrease is found for GeSbTe NPs when the size of the NPs decrease. Despite the different methods to grow NPs, the data derived for the GeTe NPs in this work agree excellently with the size dependency determined for previous NPs prepared by chemical synthesis. Note that the crystallization temperature of GeTe NPs in this work is slightly higher compared to the previous GeTe NPs due to the small amount of methane incorporation to facilitate the formation of nascent NPs during NPs deposition. We have observed in previous work that the methane addition can enhance the stability of the amorphous phase of GeSbTe NPs therefore a similar effect is expected for GeTe NPs.[22]

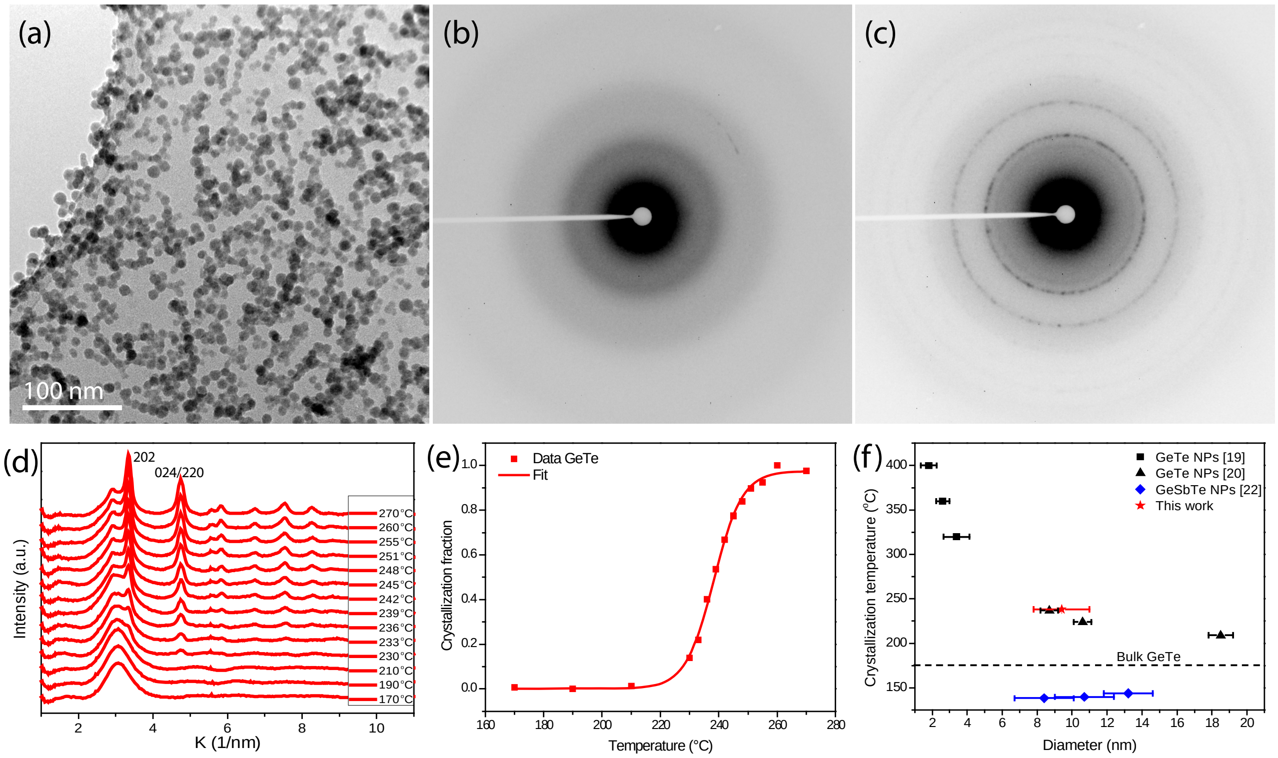

Figure 7.1 The morphology, crystallinity and slow crystallization of GeTe NPs. (a) Bright field TEM image showing the morphology of the as-deposited GeTe NPs. Selected area electron diffraction (SAED) patterns of the GeTe NPs recorded at room temperature (b) and 270 ^{o}C (c) show the amorphous to crystalline transition. (d) Azimuthal integral of the SAED patterns recorded at different temperatures. The crystallization fraction as a function of temperature is shown in (e), and the size-dependent crystallization temperatures of GeTe and GeSbTe NPs are shown in (f).

7.3.2 Ultrafast crystallization

The fast crystallization was accomplished by heating single GeTe flakes, that are scraped off from the glass substrate, at various heating rates ranging from 100 to 20000 K s^{-1} by ultrafast differential scanning calorimetry (DSC). The obtained DSC traces are shown in Figure 7.2a, where the exothermic crystallization peaks are distinctly observed, as shown by the arrows in Figure 7.2a. The crystallization peak temperature (T_p) shifts from ~280 ^{o}C at 100 K s^{-1} to 365 ^{o}C at 20000 K s^{-1}. Note that for the GeTe NPs, the crystallization peak was not observed above 20000 K s^{-1} due to the limit of the maximum temperature that the ultrafast DSC can reach (450 ^{o}C). The shift of T_p is expected according to Kissinger:[25]

$$\frac{Q}{R} = -\frac{d\ln(\Phi/T_p^2)}{d(1/T_p)} \tag{7.1}$$

with Q the activation energy for crystallization, R the gas constant, and Φ the heating rate. Then the data obtained by DSC are depicted in a Kissinger plot, as shown in Figure 7.2b. As shown in the Kissinger plot, the crystallization follows Arrhenius behavior (i.e. a linear dependence in the Kissinger plot) for heating rates Φ below 2500 K s^{-1} and it breaks down for Φ above 2500 K s^{-1}. The linear fit in the Kissinger plot below 2500 K s^{-1} provides the activation energy for crystallization, E_a=4.09±0.29 eV. The activation energy is higher compared to the one of the GeSbTe NPs (~2.2 eV).[9] Above 2500 K s^{-1}, the Arrhenius behavior in the Kissinger plot breaks down, generating a strong curvature in the Kissinger plot. Hence, the activation energy of crystallization becomes temperature dependent where it decreases with the increase of temperature.

To understand the break down in the Arrhenius behavior as well as the overall crystallization kinetics, the Johnson-Mehl-Avrami-Kolmogrov (JMAK) theory was adopted to numerically model the crystallization peak temperature at various Φ . In the JMAK modeling, the crystal growth rate is the key factor that dominates the crystallization process. Analogous to our previous work,[8,9] the crystal growth rate between the glass transition and melting temperature is described as:

$$U(T)=\frac{4r_{atom}k_BT}{3\pi\lambda^2 R_{hyd}\eta(T)^{\xi}}[1-\exp(-\frac{\Delta G(T)}{k_BT})] \tag{7.2}$$

with $U(T)$ the growth rate, r_{atom} the atomic radius (~1.5 Å), λ the diffusional jump distance (here ~2.99 Å),[26] R_{hyd} the hydrodynamic radius ($R_{hyd}=r_{atom}$), k_B the Boltzmann constant, $\eta(T)$ the temperature dependent viscosity, ξ the decoupling parameter of Stokes-Einstein equation ($\xi=0.65$ as used for the GeSbTe NPs [9]) and $\Delta G(T)$ the change of Gibbs free energy, which can be described, according to Thomson and Spaepen, as:[27]

$$\Delta G(T)=\frac{\Delta H_m(T_m-T)}{T_m}(\frac{2T}{T_m+T}) \tag{7.3}$$

where ΔH_m is the latent heat of melting, approximately 0.186 eV at^{-1}, and T_m is set to 1000 K.[26] In Equation 7.2, the viscosity description is of vital importance in the modeling. As demonstrated by our previous work,[9] the generalized MYEGA model [23] that was originally proposed to describe the viscosity of metallic glass forming liquids outperformed the single fragility MYEGA model to describe the viscosity of as-deposited GeSbTe NPs, because of the relatively clear presence of Arrhenius behavior up to a certain heating rate and only a breakdown of this behavior above this heating rate. Since this is also observed in the present work for a heating rate of 2500 K s^{-1}, it is obvious to adopt the generalized MYEGA model here as well:

$$\log_{10}\eta(T) = \log_{10}\eta(\infty) + \frac{1}{T\left[W_1\exp(-\frac{C_1}{T}) + W_2\exp(-\frac{C_2}{T})\right]} \tag{7.4}$$

with $\eta(\infty)$ viscosity at infinite temperature (here it is taken as 10^{-3} Pa s), T the temperature and W_1, C_1, W_2, C_2 the fitting parameters. After the optimization, the modeled T_p at various Φ were depicted as red dotted curve in the Kissinger plot, showing an excellent fitting with the adjusted R^2=0.990. The fitting parameters in Equation 7.4 were determined as: W_1=6184.98, C_1=9061.17, W_2=4.42 × 10^{-4}, C_2=609.17. One can evidently observe that the generalized MYEGA model can nicely fit both the linear (Arrhenius behavior) and the curved (non-Arrhenius behavior) parts in the Kissinger plot.

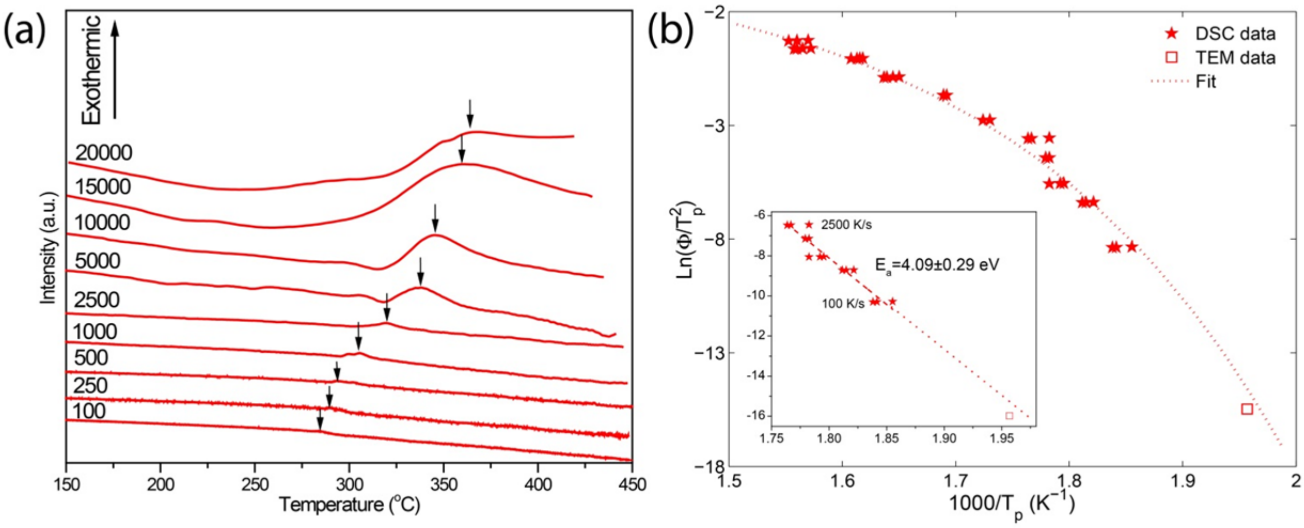

Figure 7.2 DSC traces for heating rates ranging from 100 to 20000 K s^{-1} (a) and the corresponding Kissinger plot (b). The unit for the heating rate in (a) is K s^{-1}. The inset of (b) demonstrates the zoomed-in Kissinger plot below 2500 K s^{-1}, with the linear fit indicating the activation energy of crystallization. The extrapolation of the linear fit is close to the TEM data point.

7.3.3 Viscosity and fragility

After fitting the data in the Kissinger plot, the viscosity of the as-deposited GeTe NPs is then obtained from Equation 7.4. Figure 7.3 depicts the temperature dependency of the viscosity of the as-deposited amorphous GeTe NPs. Note that in the generalized MYEGA model, the glass transition temperature (T_g) is not directly provided. The T_g is set as the temperature where the viscosity is 10^{12} Pa s, which results in T_g=467 K for the GeTe NPs. This value for T_g is higher than the one for GeTe film because of the higher crystallization temperature of the NPs.[26] The fragility, defined as:

$$m = \left. \frac{d(\log_{10} \eta(T))}{d(T_g / T)} \right|_{T=T_g} \tag{7.5}$$

was then derived as 78 for the amorphous GeTe NPs from Figure 7.3. The value for the fragility is lower than that determined for the GeTe thin films (m=132) owing to the different viscosity models adopted during numerical modeling.[15] However the fragility of GeTe NPs is higher in comparison with GeSbTe NPs, which is reasonable since GeTe NPs show a higher activation energy for crystallization than GeSbTe NPs (4.09 vs 2.43 eV). For comparison, the viscosity for GeSbTe NPs is also depicted in the Figure 7.3. The viscosity exhibits a strong (Arrhenius) behavior approaching T_g and becomes fragile (non-Arrhenius) at temperatures above ~$1.2T_g$. The extrapolated viscosity fits very well with the value at melting temperature ($\eta = 10^{-3.05}$ Pa s) determined by molecular dynamics simulation.[26]

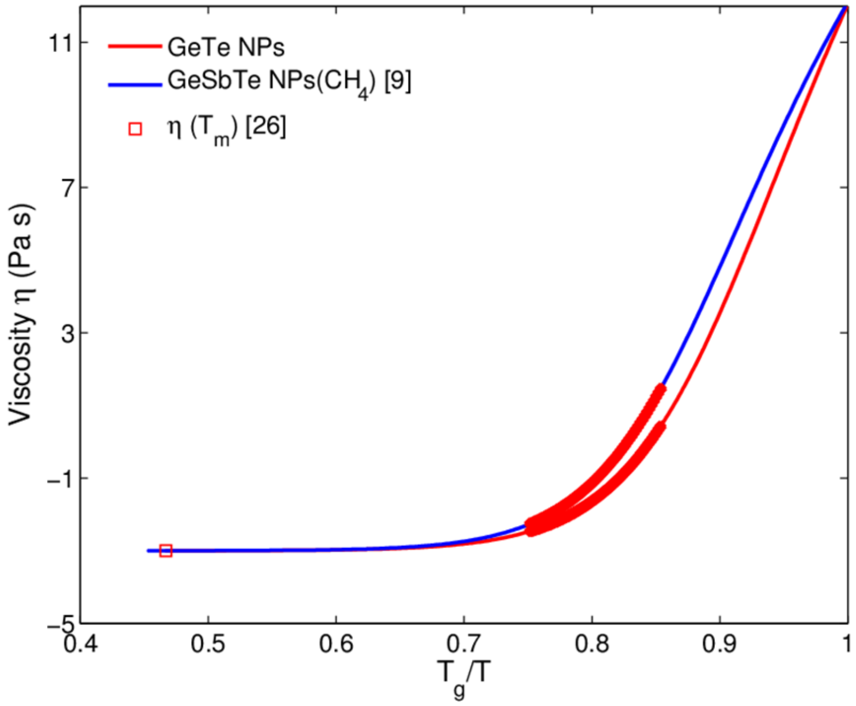

Figure 7.3 Temperature dependent viscosity of the GeTe NPs. The high activation energy for the crystallization supports the high fragility. The viscosity at melting temperature, $10^{-3.05}$ Pa s,[26] is also depicted as red open square for comparison. The thick red marked region indicates the temperature regime accessed by ultrafast DSC.

7.3.4 Crystal growth rate

The overall crystal growth rate is one of the most relevant properties of PCMs as it indicates the stability of amorphous phase at relatively low temperatures and the crystallization speed at high temperatures and is thus of key technological importance for applications such as phase-change memory. As illustrated by the solid red curve in Figure 7.4, the crystal growth rate between glass transition and melting temperatures is determined by Equation 7.2 for the as-deposited amorphous GeTe NPs. In contrast, crystal growth rates at low temperatures for GeTe thin films are shown in Figure 7.4.[28–30] The maximum growth rate (U_m) of GeTe NPs is 1.9 m s^{-1}, occurring at ~720 K (~0.72 T_m), slightly higher than GeSbTe NPs (~0.70 T_m) and lower in comparison to GeTe film (~0.79 T_m).[9,15] The U_m of GeTe NPs is comparable to that of the GeTe thin films (U_m=3.5 m s^{-1}).[15] However, the GeTe NPs show 2-3 orders of magnitude lower crystal growth rate at temperature approaching T_g in comparison with the GeTe thin film and the GeSbTe NPs, indicating a higher stability of the amorphous phase of the GeTe NPs. Due to the comparable U_m between the GeTe and GeSbTe PCMs, the GeTe NPs are the most favorable for memory applications among the PCMs shown in Figure 7.4. However the concern is the melting temperature of the GeTe NPs, which is not accessible by ultrafast DSC. Due to the large increase in the crystallization temperature of the GeTe NPs and well-known decreasing trend in melting temperature during down scaling, the

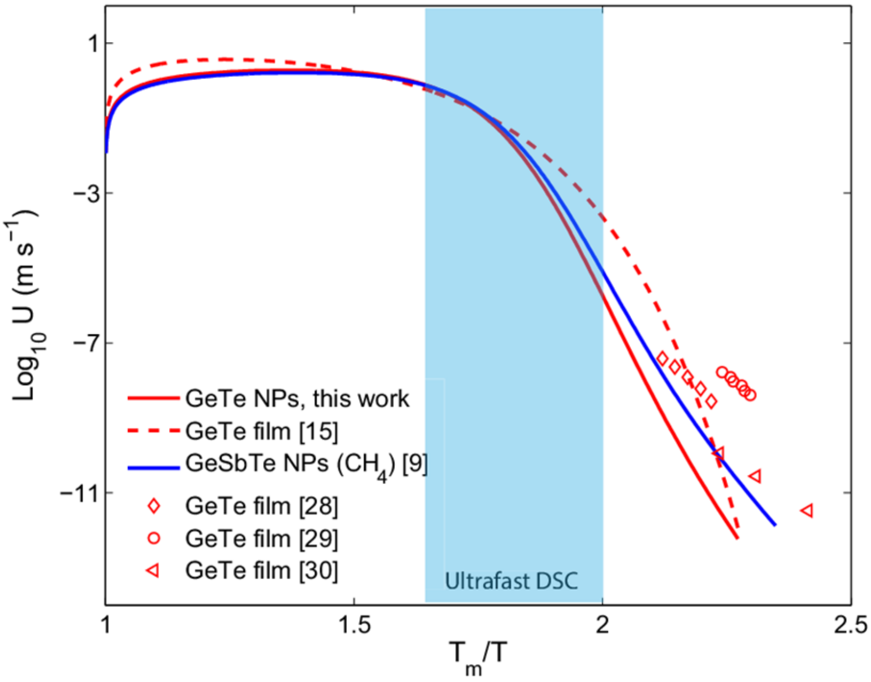

Figure 7.4 Temperature dependency of crystal growth rate of GeTe NPs. The growth rates for GeTe thin films and GeSbTe NPs are depicted for comparison.

operation window for crystallizing GeTe NPs can become very small, limiting the applicability of GeTe NPs. For instance the melting temperature of GeTe thin film with a thickness of 2 nm is about 600 ^{o}C, 120 ^{o}C lower than the bulk value.[24] So further measurements on the size dependence of the melting temperature are required before GeTe NPs can be considered for applications.

7.4 Conclusions

Amorphous GeTe nanoparticles with size, crystallinity and composition control has been successfully synthesized by inert gas condensation. In-situ heating in a transmission electron microscope reveals that the crystallization temperature of the GeTe NPs at relatively low heating rate is 60 ^{o}C higher than the one for the bulk GeTe. Ultrafast heating by differential scanning calorimetry is then utilized to unravel the crystallization kinetics of the crystallization at higher temperatures. The breakdown of Arrhenius behavior in crystallization is distinctly observed at heating rate above 2500 K s^{-1}. Numerical modeling with proper description for viscosity reveals the temperature dependency of the viscosity and crystal growth rate of the GeTe NPs. The high maximum crystal growth rate at high temperature in combination with the low crystal growth rate when the glass transition temperature is approached implies a promising application perspective of GeTe NPs in memories, but the strongly reducing temperature window between the crystallization temperature and the melting temperature when the NP size reduces can be an obstacle.

Appendix

Thermal lag

The theory to estimate thermal lag has been detailed in Appendix of chapter 3. Taking the values for heat transfer coefficient (5 to 20 kW m^{-2} K^{-1}),[31] sample thickness (200 to 500 nm) and thermal conductivity (0.23 W m^{-1} K^{-1} at 20 ^{o}C)[32] for GeTe thin films, the Boit number is then derived in the range 0.004 to 0.04 according to Equation 3.8, indicating that the assumption of a uniform temperature distribution within the sample is reasonable.

Taking the heat capacity per unit volume of GeTe thin films as 7.4×10^{5} J m^{-3} K^{-1},[15] the thermal lag caused by the heat transfer between the chip sensor and the sample is determined in the range 0.2 to 1.2 K at the maximum heating rate 20000 K s^{-1} according to Equation 3.9. This thermal lag will not affect the breakdown of the Arrhenius behavior, since the breakdown starts at 2500 K s^{-1}.

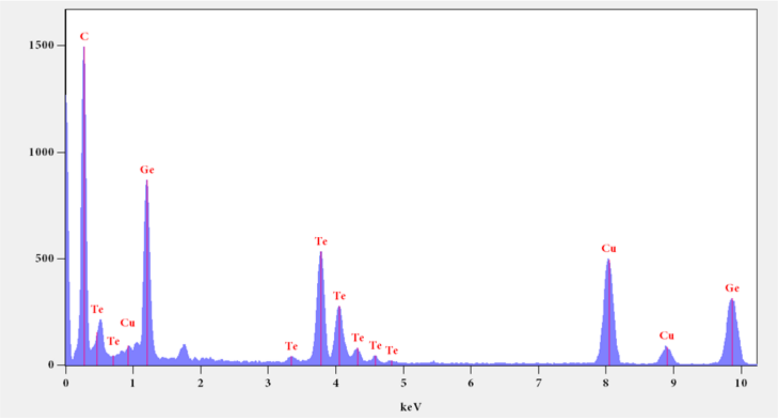

Figure 7.5 The composition of the GeTe NPs, giving a ratio Ge:Te=45:55 (±1) at%. The carbon and copper are from the membrane (holey carbon grids).

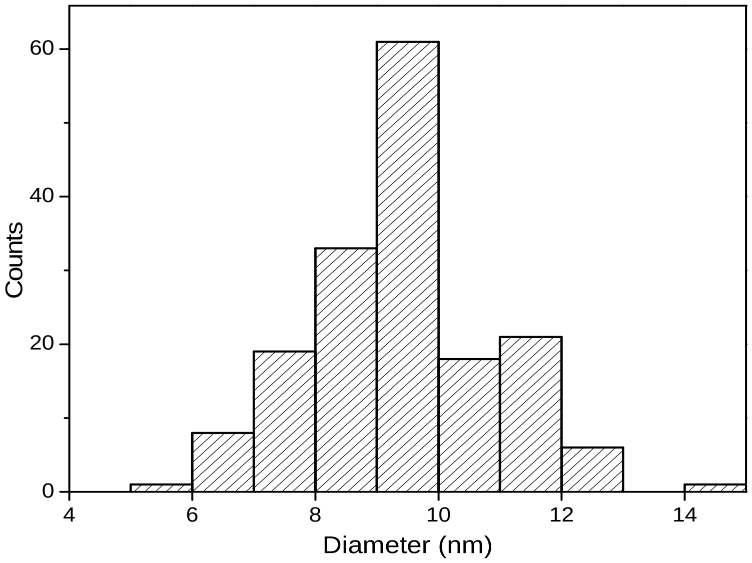

Figure 7.6 The size distribution of the as-deposited GeTe NPs, showing an average diameter of 9.4±1.6 nm.

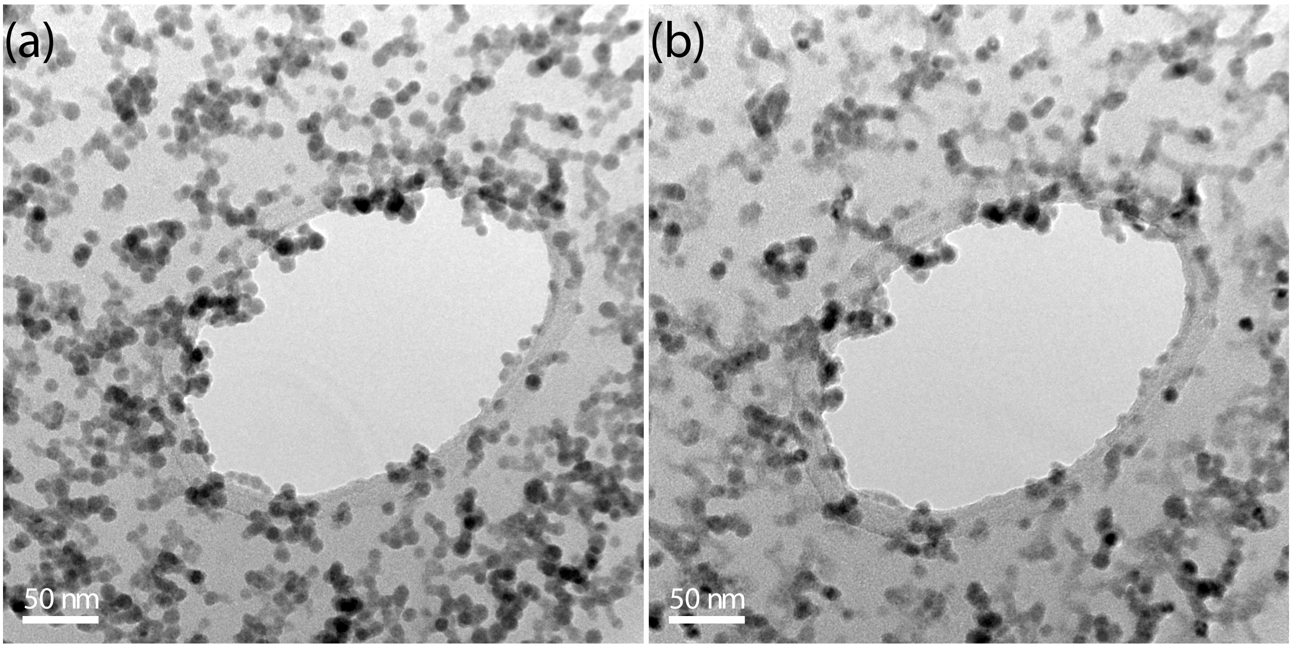

Figure 7.7 Bright field images of GeTe NPs before (a) and after (b) annealing. Coalescence of NPs can be clearly observed after annealing.

References

(1) Wuttig, M.; Yamada, N. *Nat. Mater.* **2007**, *6* (11), 824–832.

(2) Raoux, S.; Welnic, W.; Ielmini, D. *Chem. Rev.* **2010**, *110* (1), 240–267.

(3) Hosseini, P.; Wright, C. D.; Bhaskaran, H. *Nature* **2014**, *511* (7508), 206–211.

(4) Ríos, C.; Stegmaier, M.; Hosseini, P.; Wang, D.; Scherer, T.; Wright, C. D.; Bhaskaran, H.; Pernice, W. H. P. *Nat. Photonics* **2015**, *9* (11), 725–732.

(5) Tuma, T.; Pantazi, A.; Le Gallo, M.; Sebastian, A.; Eleftheriou, E. *Nat. Nanotechnol.* **2016**, *11* (8), 693–699.

(6) Orava, J.; Greer, A. L.; Gholipour, B.; Hewak, D. W.; Smith, C. E. *Nat. Mater.* **2012**, *11* (4), 279–283.

(7) Orava, J.; Hewak, D. W.; Greer, A. L. *Adv. Funct. Mater.* **2015**, n/a-n/a.

(8) Chen, B.; Momand, J.; Vermeulen, P. A.; Kooi, B. J. *Cryst. Growth Des.* **2016**, *16* (1), 242–248.

(9) Chen, B.; ten Brink, G. H.; Palasantzas, G.; Kooi, B. J. *J. Phys. Chem. C* **2017**, *121* (15), 8569–8578.

(10) Salinga, M.; Carria, E.; Kaldenbach, A.; Bornhöfft, M.; Benke, J.; Mayer, J.; Wuttig, M. *Nat. Commun.* **2013**, *4*.

(11) Sebastian, A.; Le Gallo, M.; Krebs, D. *Nat. Commun.* **2014**, *5*.

(12) Jeyasingh, R.; Fong, S. W.; Lee, J.; Li, Z.; Chang, K.-W.; Mantegazza, D.; Asheghi, M.; Goodson, K. E.; Wong, H.-S. P. *Nano Lett.* **2014**.

(13) Perniola, L.; Sousa, V.; Fantini, A.; Arbaoui, E.; Bastard, A.; Armand, M.; Fargeix, A.; Jahan, C.; Nodin, J. F.; Persico, A.; Blachier, D.; Toffoli, A.; Loubriat, S.; Gourvest, E.; Beneventi, G. B.; Feldis, H.; Maitrejean, S.; Lhostis, S.; Roule, A.; Cueto, O.; Reimbold, G.; Poupinet, L.; Billon, T.; Salvo, B. D.; Bensahel, D.; Mazoyer, P.; Annunziata, R.; Zuliani, P.; Boulanger, F. *IEEE Electron Device Lett.* **2010**, *31* (5), 488–490.

(14) Santala, M. K.; Reed, B. W.; Raoux, S.; Topuria, T.; LaGrange, T.; Campbell, G. H. *Appl. Phys. Lett.* **2013**, *102* (17), 174105.

(15) Chen, Y.; Wang, G.; Song, L.; Shen, X.; Wang, J.; Huo, J.; Wang, R.; Xu, T.; Dai, S.; Nie, Q. *Cryst. Growth Des.* **2017**, *17* (7), 3687–3693.

(16) Hirasawa, M.; Orii, T.; Seto, T. *Appl. Phys. Lett.* **2006**, *88* (9), 093119.

(17) Xiong, F.; Liao, A. D.; Estrada, D.; Pop, E. *Science* **2011**, *332* (6029), 568–570.

(18) Lee, S.-H.; Jung, Y.; Agarwal, R. *Nat. Nanotechnol.* **2007**, *2* (10), 626–630.

(19) Caldwell, M. A.; Raoux, S.; Wang, R. Y.; Wong, H.-S. P.; Milliron, D. J. *J. Mater. Chem.* **2010**, *20* (7), 1285–1291.

(20) Arachchige, I. U.; Soriano, R.; Malliakas, C. D.; Ivanov, S. A.; Kanatzidis, M. G. *Adv. Funct. Mater.* **2011**, *21* (14), 2737–2743.

(21) Polking, M. J.; Urban, J. J.; Milliron, D. J.; Zheng, H.; Chan, E.; Caldwell, M. A.; Raoux, S.; Kisielowski, C. F.; Ager, J. W.; Ramesh, R.; Alivisatos, A. P. *Nano Lett.* **2011**, *11* (3), 1147–1152.

(22) Chen, B.; ten Brink, G. H.; Palasantzas, G.; Kooi, B. J. *Sci. Rep.* **2016**, *6*.

(23) Zhang, C.; Hu, L.; Yue, Y.; Mauro, J. C. *J. Chem. Phys.* **2010**, *133* (1), 014508.

(24) Raoux, S.; Shelby, R. M.; Jordan-Sweet, J.; Munoz, B.; Salinga, M.; Chen, Y.-C.; Shih, Y.-H.; Lai, E.-K.; Lee, M.-H. *Microelectron. Eng.* **2008**, *85* (12), 2330–2333.

(25) Kissinger, H. E. *Anal. Chem.* **1957**, *29* (11), 1702–1706.

(26) Sosso, G. C.; Miceli, G.; Caravati, S.; Giberti, F.; Behler, J.; Bernasconi, M. *J. Phys. Chem. Lett.* **2013**, *4* (24), 4241–4246.

(27) Thompson, C. V.; Spaepen, F. *Acta Metall.* **1979**, *27* (12), 1855–1859.

(28) Martin Salinga; Johannes Kalb; Michael Klein; Tobias Sontheimer; Frans Spaepen; Matthias Wuttig. *EPCOS* **2007**.

(29) Mio, A. M.; Carria, E.; D'Arrigo, G.; Gibilisco, S.; Miritello, M.; Grimaldi, M. G.; Rimini, E. *J. Non-Cryst. Solids* **2011**, *357* (10), 2197–2201.

(30) Bastard, A.; Bastien, J. C.; Hyot, B.; Lhostis, S.; Mompiou, F.; Bonafos, C.; Servanton, G.; Borowiak, C.; Lorut, F.; Bicais-Lepinay, N.; Toffoli, A.; Sandhya, C.; Fantini, A.; Perniola, L.; Gourvest, E.; Maitrejean, S.; Roule, A.; Sousa, V.; Bensahel, D.; André, B. *Appl. Phys. Lett.* **2011**, *99* (24), 243103.

(31) Şahin, H. M.; Kocatepe, K.; Kayıkcı, R.; Akar, N. *Energy Convers. Manag.* **2006**, *47* (1), 19–34.

(32) Fallica, R.; Varesi, E.; Fumagalli, L.; Spadoni, S.; Longo, M.; Wiemer, C. *Phys. Status Solidi RRL – Rapid Res. Lett.* **2013**, *7* (12), 1107–1111.

Summary

Phase-change materials (PCMs) have been successfully used in optical storage and are among the most promising candidates for next generation memory technology. The application is based on the rapid and reversible switching between the amorphous and crystalline phases of the materials that provides high optical/electrical contrast between these two phases. Although a lot of attentions have been dedicated to the exploration of the phase transition in PCMs for more than two decades, the crystallization kinetics of the transition at relatively high temperatures remained for a long time highly challenging due to the short time and length scales involved. However, the crystallization kinetics at high temperature is essential for applications as the switching mostly takes place within the temperature interval 400-500 °C.

In this thesis we investigated the crystallization kinetics of PCMs. In chapter 3 we applied ultrafast heating to Ge_7Sb_{93} thin films with various heating rates by ultrafast differential scanning calorimetry (DSC). A breakdown of Arrhenius behavior was observed for crystallization at high heating rates. With numerical modeling using Johnson-Mehl-Avrami-Kolmogorov theory in combination with two different models for crystal growth rate we studied the crystallization kinetics in the temperature range in-between the glass transition and the melting temperatures. By comparing the modeled crystal growth rates with the experimentally obtained direct growth data for Ge_7Sb_{93} films, we derived a proper model to describe the viscosity and growth rate for PCMs, paving the way for later research on the kinetics of phase-change nanoparticles.

The search for a next generation, potentially universal, memory drives the exploration of non-volatile memory with larger storage capability and faster switching speed. Down-scaling PCMs provides a promising solutions to reach these goals. Inert gas condensation based on magnetron sputtering offers us a facile way to deposit ligand-free nanoparticles at room temperature. Using this method, we synthesized $Ge_2Sb_2Te_5$ nanoparticles, one of the most widely used PCMs, in diameters below 20 nm with excellent composition, crystallinity and size control (Chapter 4). Subsequent characterization by transmission electron microscopy revealed the size dependence of crystallization of these nanoparticles, where the crystallization temperature slightly decreases with the reduction of size. A small amount of methane, added during deposition, efficiently increases the crystallization temperature of the nanoparticles, resulting in an enhanced stability of the amorphous phase of the nanoparticles. To understand the crystallization kinetics of these nanoparticles at high temperature, ultrafast crystallization was employed (Chapter 5). The crystallization follows

Arrhenius behavior for a quite long heating rate range, while it breaks down at heating rates above ~10 000 K/s. We interpreted this phenomenon by adopting a viscosity model with a strong-to-fragile transition within the supercooled liquid, a phenomenon ubiquitously existing in metallic glasses. Adopting the model established for the Ge_7Sb_{93} thin films, we unraveled the viscosity as well as the crystal growth rate in-between the glass transition and the melting temperatures for the as-deposited amorphous $Ge_2Sb_2Te_5$ nanoparticles. The methane incorporation did not influence the maximum crystal growth rate in the nanoparticles, but improves the low temperature retention and therefore provides an effective way to improve the overall performance of the PCM. This improvement by methane was observed for the GeTe nanoparticles as well (Chapter 7).

This thesis demonstrates extensive investigations on the crystallization of phase-change nanoparticles. $Ge_2Sb_2Te_5$ nanoparticles incorporated with methane present promising properties for applications in memory. However, to use these nanoparticles in memories, knowledge of the conductivities of the amorphous and crystalline nanoparticles is essential. However, the small size of the nanoparticles makes the connection of the nanoparticles to electrodes highly challenging. One of the options is conductive atomic force microscope which can readily probe the nanoparticles with sizes around ten nanometers and is able to measure the current through the nanoparticle at certain applied voltages. This approach opens a door to study the explore the scalability of the threshold voltage as well as power consumption of crystallization which is key to phase-change memory.

The interaction of the phase-change nanoparticles with the underlying substrate is also relevant for the potential usage of the nanoparticle-based systems. So we investigated the sticking dynamics of the $Ge_2Sb_2Te_5$ nanoparticles on graphene (Chapter 6). The areal density of nanoparticles landed on suspended graphene is ~3 times higher than the one on graphene supported by a thin amorphous carbon film, which we attribute to the difference in surface energy of both types of graphene. Exposure to air for 8 weeks leads to significant oxidation of the Ge atoms while Sb and Te did not show obvious oxidation, where oxidation was more severe for the nanoparticles on the suspended graphene than on the supported graphene.

An intriguing example of the applications of the phase-change nanoparticles is the ability to modify the surface wettability. Amorphous phase-change nanoparticles deposited on highly oriented pyrolytic graphite increased the hydrophobicity of the surface. By annealing the system (to a moderate temperature of 120 °C), the hydrophobic surface switched to hydrophilic. This interesting phenomenon indicates a novel approach to control the surface wettability by phase-change nanoparticles.

Samenvatting

Phase-Change Materialen (PCMs) zijn succesvol geïmplementeerd in optische dataopslag, en behoren tot de meest veelbelovende kandidaten voor een volgende generatie geheugen-technologie. Deze toepassing is gebaseerd op snel en reversibel wisselen tussen de amorfe en kristallijne fasen van een materiaal, dat een groot optisch of elektrisch contrast heeft tussen deze beide fasen. Hoewel de afgelopen twee decennia veel inspanningen gewijd zijn aan het onderzoek naar de fasetransitie op relatief hoge temperaturen, bleef het ontrafelen van de kristallisatie-kinetiek tot voor kort een grote uitdaging vanwege de korte tijd- en lengteschalen waarop deze processen plaatsvinden. Toch is kennis van deze kinetiek essentieel, omdat het schakelen van de geheugentoestanden merendeels plaatsvindt in het temperatuurregime tussen de 400 en 500 ^{o}C. In deze thesis hebben we de kristallisatie-kinetiek van PCMs onderzocht. In hoofdstuk 3 beschrijven we onderzoek waarbij met behulp van ultrasnelle *differential scanning calorimetry* (DSC) dunne Ge_7Sb_{93} films ultrasnel verhit zijn. We vonden een afwijking van Arrhenius-gedrag voor kristallisatie bij snelle verhitting. Door middel van numeriek modelleren met behulp van de Johnson-Mehl-Avrami-Kolmogorov theorie, in combinatie met twee verschillende modellen voor de kristalgroeisnelheid, hebben we de kristallisatiekinetiek in het temperatuurbereik van glastransitie tot smelttemperatuur bestudeerd. Door de gemodelleerde kristalgroei te vergelijken met direct verkregen experimentele kristalgroeidata van Ge_7Sb_{93}, hebben we een model afgeleid om de viscositeit en groeisnelheid van PCMs te beschrijven. Dit heeft de weg vrijgemaakt voor verder onderzoek naar de kinetiek van *phase-change* nanodeeltjes.

De zoektocht naar een volgende generatie, potentieel meer universeel, geheugen is een stimulans voor het onderzoek naar niet-volatiel geheugen met grotere opslagcapaciteit en snellere schakelsnelheid. Het verkleinen van PCMs kan hierbij een beloftevolle oplossing bieden. Inerte gas condensatie gebaseerd op magnetron-sputteren is een geschikte methode om ligand-vrije nanodeeltjes bij kamertemperatuur te deponeren. Met deze methode hebben we $Ge_2Sb_2Te_5$-nanodeeltjes, een van de meest gebruikte PCMs, gesynthetiseerd met diameters beneden 20 nm, met excellente compositie, kristalliniteit, en grootte-controle. Tijdens daarop volgende karakterisatie in een transmissie-elektronen microscoop bleek dat de kristallisatietemperatuur van de nanodeeltjes licht afnam naarmate de deeltjes kleiner werden. Kleine hoeveelheden methaan, toegevoegd tijdens het depositieproces, bleek effectief in het verhogen van de kristallisatietemperatuur van de nanodeeltjes, wat resulteerde in een toegenomen stabiliteit van de amorfe fase van de nanodeeltjes. Om de kristallisatiekinetiek van de nanodeeltjes op hoge temperatuur te begrijpen, is ultrasnelle

DSC gebruikt. De kristallisatie bleek Arrhenius-gedrag te vertonen over een grote range van verhittingssnelheden, maar bleek hiervan af te wijken voor snelheden boven 10 000 K/s. We hebben dit fenomeen geintepreteerd door middel van een viscositeitsmodel met een *fragile-to-strong* transitie in de supergekoelde vloeistof, een fenomeen alomtegenwoordig in metallische glazen. Met het eerder vastgestelde model voor de dunne Ge_7Sb_{93} films, hebben we vervolgens de viscositeit en de kristalgroeisnelheid bepaald tussen de glastransitie en de smelttemperatuur voor de als-gedeponeerd amorfe $Ge_2Sb_2Te_5$ nanodeeltjes. De methaan-opname had geen invloed op de maximale groeisnelheid van de nanodeeltjes bij hoge temperatuur, maar bleek dus wel de stabiliteit van de amorfe fase bij lage temperatuur te verbeteren en is daarom een effectieve manier om de algehele prestaties van de nanodeeltjes te verbeteren. Deze verbetering door methaan hebben wij ook bij GeTe-nanodeeltjes waargenomen.

Deze thesis toont dus uitgebreid onderzoek aan de kristallisatie van *phase-change*-nanodeeltjes. $Ge_2Sb_2Te_5$ nanodeeltjes met toegevoegd methaan laten veelbelovende eigenschappen voor toepassingen in geheugen zien. Om deze nanodeeltjes in geheugen te gebruiken is kennis van de elektrische geleiding van de amorfe en kristallijne nanodeeltjes essentieel. De kleine omvang van de nanodeeltjes maakt het een grote uitdaging om de nanodeeltjes te verbinden met elektroden. Een van de opties is het gebruik van een *conductive atomic force microscope*, die nanodeeltjes met een grootte rond 10 nm kan detecteren, en de electrische stroom door een nanodeeltje kan meten voor een gegeven aangebracht voltage. Deze aanpak opent de deur voor het bestuderen van de schaalbaarheid van het drempel-voltage en energieverbruik van kristallisatie, wat essentieel is voor *phase-change*-geheugen.

De interactie van nanoparticles met het onderliggende substraat is ook relevant voor het potentiele gebruik van nanodeeltjes gebaseerde systemen. We hebben de stictie-dynamica van $Ge_2Sb_2Te_5$ nanodeeltjes op grafeen onderzocht. De dichtheid van nanodeeltjes die landden op vrijhangend grafeen was ~3 keer hoger dan de dichtheid op grafeen ondersteund door een dunne amorfe carbonfilm, wat we toeschrijven aan het verschil in oppervlakte-energie van beide typen oppervlakken. Blootstelling aan lucht gedurende 8 weken leidt tot sterk preferente oxidatie van de Ge atomen terwijl Sb en Te niet duidelijk oxideerden, waarbij de oxidatie van de deeltjes op vrijhanged grafeen weer sterker is dan op ondersteund grafeen. Een bijzonder voorbeeld van de toepassing van PCM nanodeeltjes is het modificeren van de oppervlakte-wetting. De PCM-nanodeeltjes werden gedeponeerd op sterk georienteerd pyrolitisch grafiet, en verhoogden hierdoor de hydrofobiciteit van het oppervlak. Door het systeem te gloeien (bij een relatief lage temperatuur van 120 °C), veranderde het hydrofobe oppervlak naar hydrofiel. Dit interessante fenomeen geeft een nieuwe aanpak om de oppervlaktewetting te modificeren en wellicht te kunnen schakelen met behulp van *phase-change* nanodeeltjes.

List of publications

(1) B. Chen, D. de Wal, G. ten Brink, G. Palasantzas, B. J. Kooi, Resolving the crystallization kinetics of GeTe phase-change nanoparticles, submitted.

(2) B. Chen, L. V. Do, G. ten Brink, G. Palasantzas, P. Rudolf, B. J. Kooi, Dynamics of GeSbTe phase-change nanoparticles on graphene, submitted.

(3) B. Chen, L. Xing, G. ten Brink, G. Palasantzas, B. J. Kooi, Size-dependent crystallization of GeSb phase change nanoparticles, in preparation.

(4) B. Chen, G. ten Brink, G. Palasantzas, B. J. Kooi, Crystallization Kinetics of GeSbTe Phase-Change Nanoparticles Resolved by Ultrafast Calorimetry, *J. Phys. Chem. C* **2017**, 121, 8569.

(5) B. Chen, G. ten Brink, G. Palasantzas, B. J. Kooi, Size dependent and tunable crystallization of GeSbTe phase-change nanoparticles, *Sci. Rep.* **2016**, 6, 39546

(6) B. Chen, J. Momand, P.A. Vermeulen, B. J. Kooi, Crystallization Kinetics of Supercooled Liquid Ge–Sb Based on Ultrafast Calorimetry, *Cryst. Growth Des.* **2015**, 16, 242.

(7) L. Xing, G. ten Brink, B. Chen, F. P. Schmidt, G. Haberfehlner, F. Hofer, B. J. Kooi, G. Palasantzas, Synthesis and Morphology of Iron–iron Oxide Core–shell Nanoparticles Produced by High Pressure Gas Condensation. *Nanotechnology* **2016**, *27*, 215703.

(8) G. ten Brink, P. J. van het Hof, B. Chen, M. Sedighi, B. J. Kooi, G. Palasantzas, Control Surface Wettability with Nanoparticles from Phase-Change Materials. *Appl. Phys. Lett.* **2016**, *109*, 234102.

Acknowledgement

I could not finish my PhD degree here without the help and support from people around me. Here I would like to take the chance to express my sincere thanks to all of you!

First I would like to deliver my thanks to my marvelous supervisor Prof. dr. ir. Bart J. Kooi, for giving me the opportunity to work in the group of Nanostructure Materials and Interfaces. I can still remember that you showed me our lab on my first day of working. All my skills in TEM are from you; Your patience on teaching me the details of TEM is amazing. I appreciate a lot the freedom you give to me on the research, while you always supported me my decisions. I could always walk into your office when I encountered troubles in research and ask for suggestions from you. The discussion with you can always inspired me and make me confident on research. You are a great supervisor who thinks of his students and I feel lucky working with you. My great thanks to you Bart!

I would also like to thank my second promotor Prof. dr. George Palasantzas. I learnt a lot from you about our nanocluster deposition system. I am always surprised about your fast response of emails, even on vacations. My sincere thanks also go to Gert H. ten Brink. You taught me how the nanoclusters source works and how to treat it gently. The discussion with you on the nanocluster source helped me a lot to improve the output of the nanocluster source.

I am grateful to the assessment committee members, Prof. dr. H. Bhaskaran, Prof. dr. M. A. Loi, Prof. dr. K. U. Loos for their careful reading and helpful suggestions to improve this thesis.

My special thanks to my office mates, Lijuan Xing, Jamo Momand, Paul A. Vermeulen, Weiteng Guo and Xukai Zhang for scientific and daily discussions, jokes and games. Lijuan, we have been friends for more than 10 years. It is amazing working here with you. Thank you for all the discussions with you and your help on work and daily life. My best wishes to you & Peiliang Zhao. Jamo and Paul, I am grateful to all help from you on the experiments, instruments and the valuable suggestions on my research. Besides, I enjoyed the time learning Dutch from you. There are lots of fun squashing and wall climbing with you, Paul. Weiteng, I am glad collaborating with you and becoming your friend. You made our office joyful. I had full of memorable time playing badminton with you. Xukai, your amazing perseverance surprised me; I learnt a lot from you on sports. I present my deepest gratitude to all of you and wish you success in science and happy life.

I would like to acknowledge my present and ex colleagues, Vitaly Svetovoy, Gopy Krishnan, Anna Mc Ewan, Mehdi Sedighi, Gert Eising, Zahra Babamahdi, Heng Zhang, Xiaotian Zhu, Dennis de Wal, Sytze de Graaf, Jefta Mulder and Peter Jan van het Hof for the great fun at tea time and group activities we anticipated together. I appreciate a lot the free and cozy atmosphere in our group, making my life here more relaxed and enjoyable. My earnest thanks to all the group members in Nanostructured Materials and Interfaces!

Research involves collaborative work as well. I am grateful to all the collaborators, Lam Van Do, Prof. Petra Rudolf, Barbara Casarin and Marco Malvestuto for your efficient work. Thank JEOL and FEI for obtaining the STEM results for the nanoparticles on graphene.

My big thanks to Paul and Bart for their effort put on the Dutch summary of my thesis.

Many thanks to my Paranymphs, Weiteng and Pu Yang for your efforts and time on helping me in the preparation of PhD ceremony.

I would like to thank China Scholarship Council for the financial support to my PhD research. Also I would like to thank my friend Yuxia and Zehong for their help to obtain CSC grant.

Apart from science, there are many friends with whom lots of joyful and pleasant memories were created in Groningen. Here I would like to address my greatest and deepest thanks to all of you. Pu, a perfect friend who has being sharing, giving useful advices and helping. Peiliang, Jun Li, Ling Liu, Shishi Wu, Yizhi Jiang, Jinfeng Shao, Ximin Wang, Yufan Guo, Hao Tian, Huatang Cao, Yingfen Wei, Lei Liang & Juan Shan, Rongjing Zhang, Xuewen Zhang& Min Wu, Jiquan Wu, Bin Jiang, Yi Zhang, Qian Li, Miao Wang, Yu Sun, Jing Liu, Jin Xu, Jie Yang & Honghua Fang, Xiaoming Zhang & Ping Xu, Huifang Yin, Zhengtao Li, Zheng Cheng, and Peng Wang. I would like to thank the Groningen badminton group members as well for all nice games and teaching me badminton techniques; playing badminton enriched my leisure time.

Beibei Wu, I would like to thank you for all the support and encouragement you gave to me when I faced problems. Your curiosity to the world made me a curious person again.

I would like to present my deepest appreciation to Prof. dr. Fushun Liu for supervising my mater project. You taught me to be an independent researcher. Many thanks to Shun Guo and Qingqun Meng who taught me what makes a good researcher. Guangyue Liao, thank you for encouraging me to pursue my PhD abroad. Thanks also go to Beihang University and the University of Groningen which support my grant application to CSC and making the whole process smooth.

最后，希望把我最真挚的感谢给我的家人。爸妈一直以来对我的无私的支持和帮助，才让我走到现在，无论我做什么决定你们总是在背后默默地支持我，让我可以放心的前行，追寻自己的梦想。外公外婆，抱歉过去几年不能经常去看你们。

Groningen
Oct. 2017
陈彬

Curriculum vitae

Bin Chen was born on 16th April 1987 in Sichuan of China. After obtaining the B. Sc of materials science at Shandong University in 2010, he continued doing a master project at Beihang University. Focusing in the field of shape memory alloy under the supervision of Prof. Fushun Liu, he obtained M. Sc of materials science in March 2013. Funded by China scholarship council, he then went to the Netherlands to pursue his PhD at the University of Groningen since October 2013. His research was focused on the crystallization behavior of chalcogenide based phase-change nanoparticles under the supervision of Prof. dr. Bart J. Kooi and Prof. dr. George Palasantzas.